

TABLE OF CONTENTS

	Page
INTRODUCTION	1
CHAPTER 1 CONTEXT AND LITERATURE REVIEW	3
1.1 Environmental issues	3
1.2 Thesis Objectives	4
1.3 Morphing Wing Concept in the Aviation Domain	4
1.3.1 Morphing Wing: Challenges and Benefits.....	4
1.3.2 Origin of Morphing in Aerospace.....	6
1.3.3 The CRIAQ Morphing Wing Technology Project.....	7
1.4 State of the Art: Numerical Prediction and Experimental Detection of the Laminar to Turbulent Boundary Layer Transition	11
1.4.1 Boundary Layer Theory.....	11
1.4.2 Numerical Prediction of the Boundary Layer Transition: N-factor Method.....	14
1.4.3 Experimental Determination of the Boundary Layer Transition Region..	16
1.5 Aeroelastic Behavior and Vibration Measurements of a Wing	22
1.5.1 Aeroelastic Behavior.....	22
1.5.2 Strain Gages	23
1.5.3 Accelerometers	23
CHAPTER 2 PRESSURE DATA ACQUISITION SYSTEM AND POST PROCESSING METHODOLOGY	25
2.1 Context.....	25
2.2 Description of the Wing Model	26
2.3 Real Time Acquisition System for Pressure Measurements: Kulite Transducers Setup and their Installation on the Wing	27
2.4 Numerical Aerodynamic Optimization and Prediction of the Performances of the Wing Airfoil	32
2.5 Description of the Wind Tunnel Post Processing Procedure	34
2.5.1 Pressure Coefficient Distribution.....	34
2.5.2 Laminar to Turbulent Boundary Layer Detection	36
CHAPTER 3 VIBRATION DATA ACQUISITION SYSTEM AND REAL TIME PROCESSING	47
3.1 Context.....	47
3.2 Data Acquisition System.....	47
3.2.1 Hardware Development	47
3.2.2 Software Development.....	52
CHAPTER 4 WIND TUNNEL TESTS AND RESULTS	61
4.1 Wind Tunnel Test Procedure	61

4.1.1	NRC Wind Tunnel Description	61
4.1.2	Wind Tunnel Test Preparation and Progress	63
4.2	Overview of Aerodynamics Results	66
4.3	Vibration Experimental Results	85
CONCLUSION		93
RECOMMENDATIONS		97
ANNEX I	SPECIFICATIONS OF THE PRESSURE SENSORS	99
ANNEX II	ACCELEROMETERS SPECIFICATIONS	101
ANNEX III	SPECIFICATION OF THE ACQUISITION MODULE FOR ACCELEROMETERS	103
BIBLIOGRAPHY		105

LIST OF TABLES

	Page
Table 1.1	Classification of the wing morphing concept6
Table 2.1	Chord percentage at which Kulite sensors are positioned31
Table 2.2	Tested cases optimized for laminar flow improvement.....33
Table 4.1	NRC Wind Tunnel Technical Specifications.....63
Table 4.2	Experimental wing lift and drag coefficients for un-morphed and morphed wing configurations for case #40 to case #4583
Table 4.3	Maximum Amplitudes of the Recorded Accelerations.....86

LIST OF FIGURES

	Page
Figure 1.1 The mechanical principle of morphing	8
Figure 1.2 Morphing skin location on a typical wing aircraft.....	9
Figure 1.3 Cross section and bottom view of the MDO-505 wing model	10
Figure 1.4 Wing airfoil section optimization	11
Figure 1.5 Boundary layer of a flow over a plane plate	12
Figure 1.6 Pressure distribution of a NACA 4415 profile for a Mach number of 0.19, a Reynolds number of 2e6 and an angle of attack of 0 degrees (Popov et al., 2008)	19
Figure 1.7 Pressure coefficient distribution in the vicinity of the transition point interpolated using the Spline and PCHIP methods. Taken from Popov et al., (2008).....	20
Figure 1.8 Second derivative of the pressure coefficient distribution interpolated using the Spline and PCHIP methods. Taken from Popov et al., (2008).....	21
Figure 2.1 Internal structure of the wing model.....	26
Figure 2.2 Graphical (and photographic) representation of Kulite XCQ-062 transducer.....	27
Figure 2.3 Sketch of a Kulite sensors installation on the composite skin.....	28
Figure 2.4 Inside surface of the composite skin.....	29
Figure 2.5 Overview of the pressure data acquisition system and connections between the components.....	30
Figure 2.6 Representation of the wing dimensions and Kulite sensors distribution on the composite skin surface.....	31
Figure 2.7 Comparison of the numerical versus the experimental pressure coefficient distribution for flight case #15; original airfoil (left) and optimized airfoil (right).....	35

Figure 2.8	Noises representation of the thirty-two sensors' power spectrums	37
Figure 2.9	Block diagram of the pressure data Post processing software	38
Figure 2.10	Standard deviation of the pressure data acquired for flight case #68; original airfoil (left) and optimized airfoil (right).....	39
Figure 2.11	PSD representation of the original airfoil of case #68 (Mach number=0.2, $\alpha=0^\circ$, $\delta=4^\circ$)	41
Figure 2.12	PSD representation of the optimized airfoil of case #68 (Mach number=0.2, $\alpha=0^\circ$, $\delta=4^\circ$)	42
Figure 2.13	Infra-Red measurements for transition location on the wing upper surface for flight case #68, original airfoil (left) and optimized airfoil (right)	44
Figure 3.1	Accelerometers setup on the wing box, aileron box and balance	48
Figure 3.2	Functional block diagram of the ADXL-326 type accelerometer	49
Figure 3.3	Architecture of the vibration data acquisition system.....	51
Figure 3.4	Block diagram of the vibration real-time acquisition software	53
Figure 3.5	Screen shot of the software interface (1)	55
Figure 3.6	Screen shot of the software interface (2)	55
Figure 4.1	Simplified scheme of the wind tunnel at the NRC (closed return)	62
Figure 4.2	CRIAQ MDO 505 project wing model setup in the NRC wind tunnel section	64
Figure 4.3	NRC subsonic wind tunnel facilities plan.....	65
Figure 4.4	Standard deviation of pressure data acquired for flight case #40, for the original (a) and the optimized airfoil (b)	67
Figure 4.5	Standard deviation of pressure data acquired for flight case #41, for the original (a) and the optimized airfoil (b)	67
Figure 4.6	Standard deviation of pressure data acquired for flight case #42, for the original (a) and the optimized airfoil (b)	68
Figure 4.7	Standard deviation of pressure data acquired for flight case #43, for the original (a) and the optimized airfoil (b)	68

Figure 4.8	Standard deviation of pressure data acquired for flight case #44, for the original (a) and the optimized airfoil (b).....	69
Figure 4.9	Standard deviation of pressure data acquired for flight case #45, for the original (a) and the optimized airfoil (b).....	69
Figure 4.10	PSD representation for the original airfoil, case #40 (Mach=0.15, $\alpha=1^\circ$, $\delta=0^\circ$)	70
Figure 4.11	PSD representation for the original airfoil, case #41 (Mach=0.15, $\alpha=1.25^\circ$, $\delta=0^\circ$)	71
Figure 4.12	PSD representation for the original airfoil, case #42 (Mach=0.15, $\alpha=1.5^\circ$, $\delta=0^\circ$)	72
Figure 4.13	PSD representation for the original airfoil, case #43 (Mach=0.15, $\alpha=2^\circ$, $\delta=0^\circ$)	73
Figure 4.14	PSD representation for the original airfoil, case #44 (Mach=0.15, $\alpha=2.5^\circ$, $\delta=0^\circ$)	74
Figure 4.15	PSD representation for the original airfoil, case #45 (Mach=0.15, $\alpha=3^\circ$, $\delta=0^\circ$)	75
Figure 4.16	PSD representation for the optimized airfoil, case #40 (Mach=0.15, $\alpha=1^\circ$, $\delta=0^\circ$)	76
Figure 4.17	PSD representation for the optimized airfoil, case #41 (Mach=0.15, $\alpha=1.25^\circ$, $\delta=0^\circ$)	77
Figure 4.18	PSD representation for the optimized airfoil, case #42 (Mach=0.15, $\alpha=1.5^\circ$, $\delta=0^\circ$)	78
Figure 4.19	PSD representation for the optimized airfoil, case #43 (Mach=0.15, $\alpha=2^\circ$, $\delta=0^\circ$)	79
Figure 4.20	PSD representation for the optimized airfoil, case #44 (Mach=0.15, $\alpha=2.5^\circ$, $\delta=0^\circ$)	80
Figure 4.21	PSD representation for the optimized airfoil, case #45 (Mach=0.15, $\alpha=3^\circ$, $\delta=0^\circ$)	81
Figure 4.22	Average transition location calculated with 2D XFOIL software and experimentally determined with Kulite sensors, for case #40 to case #45.....	82

Figure 4.23	Comparison between Kulite sensor results and infrared measurements in terms of the transition location for the original airfoils- case #40 to case #45.....	84
Figure 4.24	Comparison between Kulite sensor results and infrared measurements in terms of flow transition location for the optimized airfoils - case #40 to case# 45	85
Figure 4.25	Time and frequency domain representations of recorded accelerations Mach number = 0.15, angle of attack= 0°	87
Figure 4.26	Time and frequency domain representations of recorded accelerations Mach number = 0.2, angle of attack= 0°	87
Figure 4.27	Time and frequency domain representations of recorded accelerations Mach number = 0.25, angle of attack= 0°	88
Figure 4.28	Time and frequency domain representations of recorded accelerations Mach number = 0.25, angle of attack = 1°	88
Figure 4.29	Time and frequency domain representations of recorded accelerations Mach number = 0.25, angle of attack= 2°	89
Figure 4.30	Time and frequency domain representations of recorded accelerations Mach number = 0.25, angle of attack = 3°	89

LIST OF ABBREVIATIONS

CF	Cross Flow
CFD	Computational Fluid Dynamics
CIRA	Italian Aerospace Research Center (Centro Italiano Ricerche Aerospaziali)
CP	Pressure coefficient
CRIAQ	Consortium for Research and Innovation in Aerospace in Quebec
EPM	Ecole polytechnique de Montréal
ÉTS	École de Technologie Supérieure
FEM	Finite Element Model
FFT	Fast Fourier Transform
IATA	International Air Transport Association
IAR	Institute for Aerospace Research
IR	Infra Red
LAMSI	Shape Memory Alloys and Intelligent Systems Laboratory
LARCASE	Research Laboratory in Active Controls, Avionics and Aeroservoelasticity
MEMS	Micro Electro-Mechanical System
MDO	Multi-Disciplinary Optimization
NACA	National Advisory Committee for Aeronautics
NI	National Instruments
NRC	National Research Council Canada
NSERC	National Sciences and Engineering Research Council of Canada
PSD	Power Spectrum Density

XX

SD	Standard Deviation
Ts	Tollmien Schlichting
USB	Universal Serial Bus
WWTs	Wind Tunnel Tests

LIST OF SYMBOLS

A_i	Amplitude of the sinusoid i
C_p	Pressure coefficient
f	Frequency
L	Characteristic Length
M	Mach number
Re	Reynolds number
U	Flow velocity
U_∞	Characteristic air speed
V	air speed
ξ	Boundary layer thickness
Φ_i	Phase of the sinusoid i
α	Angle of attack
δ	Deflection angle of the aileron
μ	Dynamic viscosity of air
Δp	Differential pressure

INTRODUCTION

Carbon dioxide emissions from the aeronautical sector are an important factor in global warming, a phenomenon that has been noticeably increasing in recent years. In addition to reducing the fuel consumption of airplanes, others environmental issues and concerns have had increasing influence on the development of new aircraft technologies. The improvement of airplane aerodynamic performance is one very promising approach for green aircraft development. The international multidisciplinary project CRIAQ MDO 505 was created to support research work on this aspect, involving Canadian team partners from École de technologie supérieure (ETS), École Polytechnique de Montréal, Canada's National Research Council (NRC), Bombardier Aerospace and Thales Canada, and Italian team partners from the University of Naples Federico II and CIRA. The project is led by Professor Ruxandra Botez, Head of the Research Laboratory in Active Controls, Avionics and Aeroservoelasticity (LARCASE) located at ETS, and my thesis supervisor.

The CRIAQ MDO 505 project evaluates the improvement of the aerodynamic performance of a wing prototype by means of the "morphing wing" approach. The laminarity improvement is gained by delaying the laminar to turbulent flow transition region towards the wing trailing edge. The wing prototype has a span of 1.5 meters and a root chord of 1.5 meters. Its composite upper skin surface is designed and manufactured to be flexible, so that the wing airfoil can change its original shape to an aerodynamically optimized shape designed for each flow case. An actuator system is installed inside the wing to achieve this morphing. This system is composed of four electrical actuators arranged two-by-two on their lines situated at 38% and 42% of the chord. The actuator system is automatically controlled by an in-house software which directs the changing of the airfoil shape depending on the wind tunnel pre-selected flow conditions.

The main objectives of this thesis are to direct and describe the vibration data acquisition during wind tunnel tests, post-process the pressure and acceleration experimental data and then interpret the obtained results.

The first chapter is a literature review arranged to familiarize the reader with the various morphing principles, vibration analysis technologies and wind tunnel testing technologies for airflow characterization. Chapter 2 is dedicated to the post-processing of the pressure data. The pressure data acquisition system is described, along with the analysis methods used to interpret pressure data representations from raw data. The experimental characterization of the wing airflow is also given, especially the determination of the laminar to turbulent boundary layer transition zone. The pressure results obtained using the post processing of the measured data are then compared with the results obtained via the infrared visualization and the results from numerical simulations. The third chapter is devoted to the description of the vibration acquisition system. All of the equipment is presented, as well as the in-house software designed to manage the real-time graphical representation and to monitor the vibrations amplitudes. The hardware/software integration is described in detail. The recorded acceleration data is submitted to a vibration analysis, with the aim of validating the numerical aeroelasticity studies conducted on the wing.

CHAPTER 1

CONTEXT AND LITERATURE REVIEW

1.1 Environmental issues

The last fifteen years (since 2000) have been marked by a huge expansion of both passenger and freight air traffic, as well as a reinforcement of aviation connectivity. Most of this expansion has been due to the continuing economic growth in emerging markets (IATA, 2015). In fact, the passenger load factor increased from 70% to 80% between 2000 and 2014. That expansion has contributed to an increase of the carbon foot print of the aviation industry, which has been identified as being responsible for 2% of the annual man-made carbon emissions annually (IATA, 2015), released during aircraft lights.

Consequently, one of the carbon emission reduction goals stated in 2009 was to reduce fuel consumption by an average of 1.5% annually, up to 2020. In 2012, aircraft flights caused 12 million tons of carbon emissions, representing an annual reduction of 1.7% in fuel consumption and surpassing the 2012 aviation industry target by 0.2 %.

In their report, IATA (2015) has estimated the influence of several actions (such as economic measures, the use of biofuels, flying smarter and the use of more efficient aircraft) on carbon dioxide emissions from 2005 to 2050. It appears that using more efficient aircraft plays an important role in the aviation industry's goal of cutting their net emissions in half by 2050, compared with those of 2005.

In addition to cost concerns, these environmental issues have stimulated the development of various innovative technologies to improve aircraft aerodynamic performance. The international multidisciplinary project CRIAQ MDO-505 was created to realize these goals, under the supervision of Professor Ruxandra Botez at the LARCASE of the ETS in Montreal. The project's objective was to design and validate a morphing wing system in a wind tunnel

using actuators and sensors to improve its aerodynamic performances (based on prior Computational Fluid Dynamics (CFD) and structure calculations).

1.2 Thesis Objectives

This Master's thesis has the double objective of managing the vibration data acquisition during wind tunnel tests and of post-processing and interpreting the pressure and acceleration experimental data.

The following theories are reviewed below to address the thesis objectives:

- The morphing wing concept;
- The numerical and experimental detection of boundary layer laminar to turbulent transition; and
- The aeroelastic behavior and vibration measurements of a wing.

1.3 Morphing Wing Concept in the Aviation Domain

1.3.1 Morphing Wing: Challenges and Benefits

The word "Morphing" comes from the verb "to morph", which refers to a continuous shape of a body, changed under its actuation system influence. In the aeronautical domain, "morphing" is defined as "a set of technologies that increase a vehicle's performance by manipulating certain characteristics to better match the vehicle's state to the environment and task at hand" (Weisshaar, 2006).

Traditional aircraft with fixed wing geometries offer have high aerodynamic performance over a fixed range, and for a limited set of flight conditions. They are designed for a specific mission, for which they are quite efficient. However, for a set of different flight conditions, they give poor aerodynamic performances and sub-optimal fuel consumption efficiency, and so are not advantageous for civilian aircraft (Barbarino *et al.*, 2011; Weisshaar, 2006). This

actually represents a weakness for aircraft, as flexibility and multirole capacities are two important aviation considerations.

Morphing aircraft, in particular those equipped with adaptive wings, have the ability to vary their geometry according to external changes in aerodynamic loads, resulting in improved aerodynamic performance at various flight conditions (Smith et Nelson, 1990) and thereby offering more efficient fuel consumption. Changing the wing geometry of an aircraft for each flight condition may require complex adaptive wing technologies, but the aerodynamic performance gained would not be negligible (Stanewsky, 2001).

The morphing of aircraft is not a new concept in the aviation industry. Technologies such as variable sweep, retractable landing gear, retractable flaps and slats, and variable incidence noses have already been investigated and analyzed as part of the morphing aircraft concept. However, most of the time, their use has not been wide-spread because of the associated penalties in terms of cost, complexity or weight, even if the penalties could sometimes be overcome by the benefits (Weisshaar, 2006).

Following the huge technological advances in smart and adaptive structures, other aspects of the morphing concept, such as changing the wing surface area to control the airfoil shape, are becoming popular research topics.

The state of art of Smart Structures and of the integration of various systems have been summarized (Chopra, 2002; Murugan et Friswell, 2013). Generally, a smart structure includes four technologies: "smart material actuators", "sensors", "control strategies" and "power conditioning electronics". The integration of smart structures in the aerospace domain is becoming common and is rapidly expanding. A "smart structure" should have the capability to respond to changing external environment conditions. In an aircraft, this capability translates into the ability to change shape in order to more efficiently withstand different load conditions.

The geometrical parameters of aircraft influenced by morphing solutions can be classified into three categories: out of plane transformation, planform alteration and airfoil adjustment (Barbarino *et al.*, 2011). Table 1.1 presents the variable parameters associated with these categories.

Table 1.1 Classification of the wing morphing concept
Adapted from Barbarino *et al.* (2011, P.4)

Planform	Sweep	Span	Chord
Out - of -plane	Twist	Dihedral/Gull	Spanwise bending
Airfoil	Camber	Thickness	

Morphing airfoil technology has become a dominant topic, surpassing the interest in the planform or out-of-plane methods. The design of a morphing airfoil technology means that the focus is on the wing skin (called "morphing skin") change, which must be soft enough to allow shape changes, while being stiff enough to withstand aerodynamic load, and to keep the desired airfoil shape (Thill *et al.*, 2008). The CRIAQ MDO 505 project is part of this recent wave of technological research projects focused on the morphing airfoil design.

1.3.2 Origin of Morphing in Aerospace

Although morphing technologies are relatively new as research areas in aerospace, the design of changing wing planforms is as 'old as motorized flight itself' (Thill *et al.*, 2008). This section will review some examples of morphing technologies' beginnings in the aerospace field.

In 1903, the aviation industry was officially marked by the beginning of controlled human flight. But even before that date, the first shape changing aircraft had already been experimented on, by Clement Ader in 1873, in France. He further proposed a wing morphing design and in the 1890's, he developed other ideas for aviation (Weisshaar, 2006).

Not long afterwards, other variable geometry technologies were experimented on in France. Along the same lines, G.T.R Hill designed a tailless monoplane aircraft called the Pterodactyl IV, which offered a variable sweep angle range of between 4 and 75 degrees that was enabled by a mechanical worm wheel arrangement driving hinged wings capable of changing the sweep angles in flight. The Pterodactyl was flight tested for the first time in 1931.

1.3.3 The CRIAQ Morphing Wing Technology Project

The multidisciplinary project CRIAQ 7.1 started in 2006 as a in collaboration among teams from:

- Aerospace companies: Bombardier Aerospace and Thales Canada;
- Universities: "École Polytechnique de Montréal" (EPM) and "École de technologie supérieure" (ETS-LAMSI et ETS-LARCASE); and
- The National Sciences and Engineering Research Council of Canada (NSERC).

Since its inception, the project has been led by Professor Ruxandra Botez, Head of the Research Laboratory in Active Controls, Avionics and Aeroservoelasticity (LARCASE), based at the ETS.

The feasibility of a morphing wing capable of reducing aircraft fuel consumption has been demonstrated. The prototype consisted of a rectangular bi-dimensional wing with a rigid inner surface that supports a flexible upper surface manufactured of composite materials. The wing was equipped with two lines of smart actuators and optical sensors to control the changing of the flexible skin's shape for various flow conditions (as shown in Figure 1.1). A 30% reduction in the wing drag was achieved by improving the laminar flow on the wing (Mamou *et al.*, 2010).

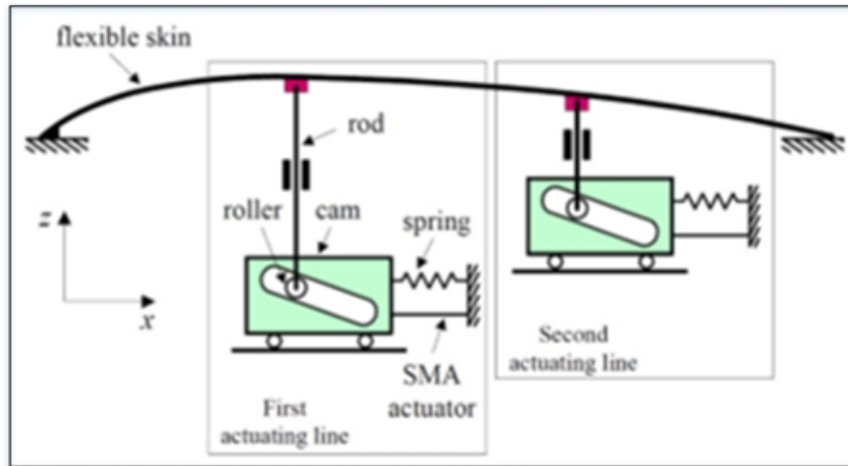


Figure 1.1 The mechanical principle of morphing
Taken from Popov *et al.* (2009)

The aerodynamic optimization of the airfoil shape was performed using both the aerodynamic modeling, and the structural Finite Element Model (FEM) of the adaptive morphing wing flexible skin (Sainmont, Paraschivoiu et Coutu, 2009). Three types of closed loop controllers have been designed and three different approaches were tested experimentally (Mamou *et al.*, 2010; Popov *et al.*, 2010). The first approach is based on the experimental pressure data recorded on the upper wing surface skin, the second approach is dependent on the wing's aerodynamic loads (drag and lift) given experimentally by the balance and the third approach relies on the transition area location determined by infrared measurements.

The ability of Kulite piezoelectric transducers to detect small pressure variations at high frequencies was validated on a morphing wing in a subsonic wind tunnel at the IAR-NRC. Sixteen Kulite transducers were installed on a diagonal line at 15 degrees situated with respect to the center line of the wing (Popov *et al.*, 2010). The successful performances of the Kulite transducers in locating the transition area during the CRIAQ 7.1 project wind tunnel tests triggered their use for the CRIAQ MDO-505 project.

The MDO-505 project, entitled 'Morphing Architectures and Related Technologies for Wing Efficiency Improvement', is a continuation of the CRIAQ 7.1 project. The objective is to

confirm the feasibility (previously demonstrated for a bi-dimensional wing prototype) of a real tridimensional wing design and its manufacture. The novelty of the project consists of the design, analysis, manufacture and validation of a wind tunnel test model having structural and aerodynamic properties of a real aircraft wing-tip. Figure 1.2 illustrates the location of the morphed upper skin on a typical aircraft wing.

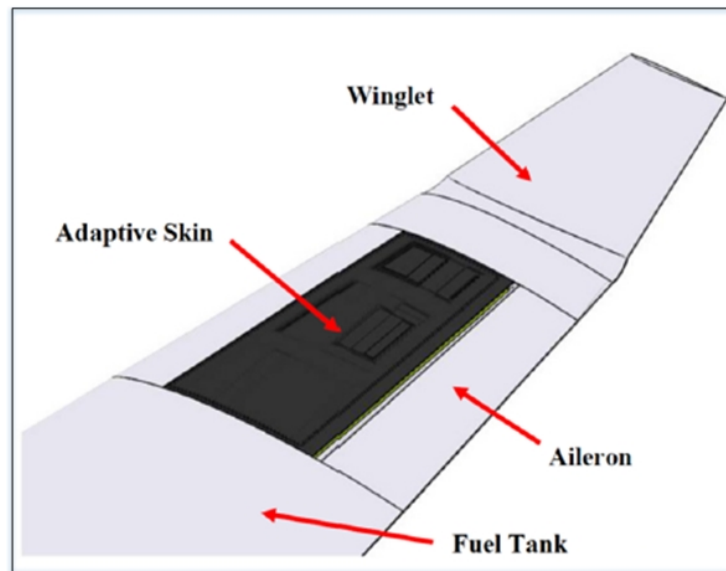


Figure 1.2 Morphing skin location on a typical wing aircraft

The prototype is a tridimensional wing with an internal structure manufactured in aluminum. The adaptive upper surface, composed of specially-designed composite materials, extends from 20% to 65% of the wing chord. The wing model is equipped with a rigid aileron situated at 72% of the chord, which will be replaced by a flexible one for test purposes. Four electrical actuators are disposed in two lines situated at 32% and 48% of the chord and are fixed on the central ribs. The actuators are controlled to push or to pull on the flexible skin to change the airfoil's shape. The cross section and the bottom view of the model used in the CRIAQ MDO-505 project are presented in Figure 1.3.

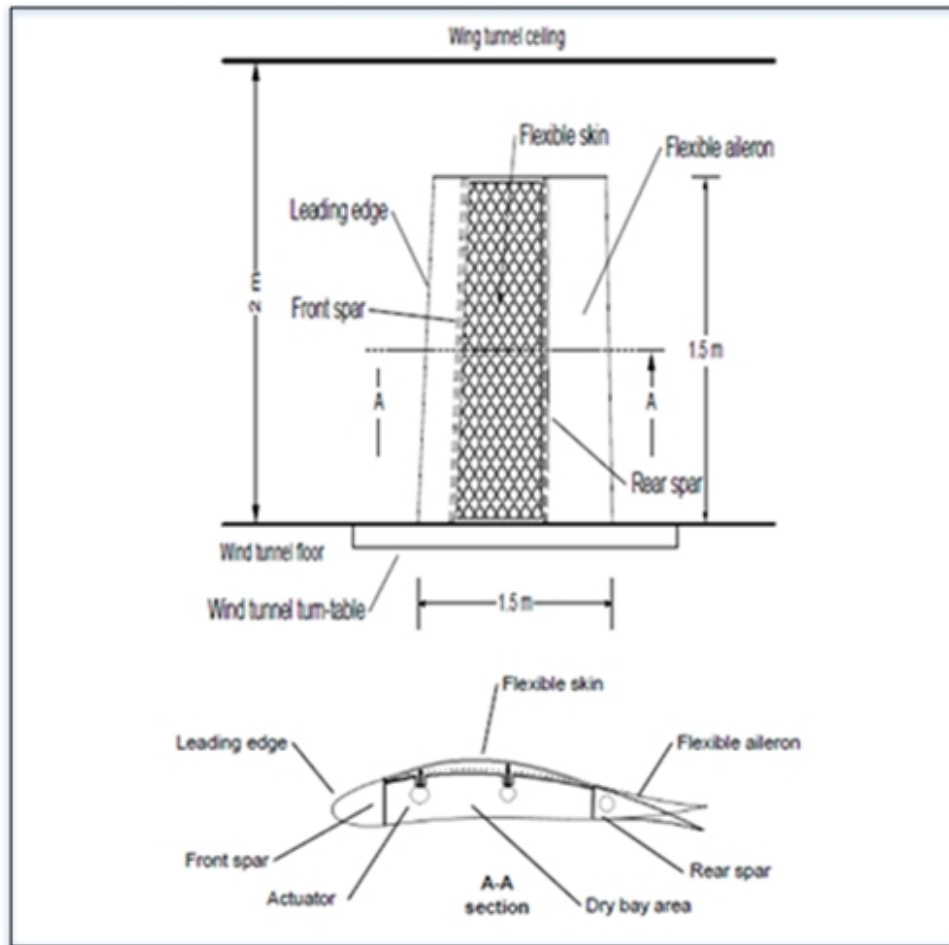


Figure 1.3 Cross section and bottom view of the MDO-505 wing model
Taken from Korenschi *et al.* (2015)

Aerodynamic optimizations of the wing airfoil were achieved by the LARCASE team at the ETS. The team conceived and developed an "in-house" methodology and code combining a genetic algorithm methodology and an Xfoil 6.96 open source aerodynamic solver (Korenschi, Sugar et Botez, 2015). The objective of this optimization was to modify the initial airfoil shape of the prototype according to the flow conditions to obtain improved airfoil shapes that increase the wing's laminarity. A 2D mathematical model (a B-splines representation) of the airfoil shape was morphed by means of two mobile control points, physically represented by the two actuators' lines on the wing. Figure 1.4 illustrates the wing airfoil section, showing the two mobile control points.

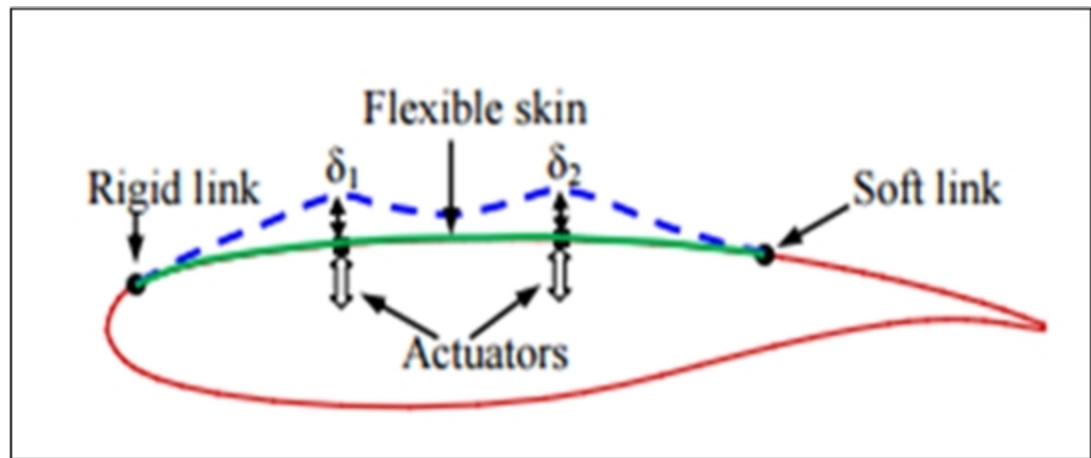


Figure 1.4 Wing airfoil section optimization
Taken from Mamou et al. (2010)

The control points can be moved up and down on the airfoil during the optimization process, as shown in Figure 1.4. The optimization must result from the displacements of control points which are linearly adapted, via the control system, to find the true displacements of actuators. Various control architectures were developed within the LARCASE team to command the vertical displacements of the actuators (Kammegne, Botez et Grigorie, 2016). The IAR-NRC team was charged with the manufacture of the rigid wing prototype, while the ETS structure team was in charge of the design and manufacture of the flexible skin.

The experimental tests were conducted in the subsonic wind tunnel situated at the IAR-NRC laboratory. The design and manufacture of the morphing aileron took place in Italy, with the participation of Naples Frederico University II, Alenia and CIRA (the Italian Aerospace Research Center).

1.4 State of the Art: Numerical Prediction and Experimental Detection of the Laminar to Turbulent Boundary Layer Transition

1.4.1 Boundary Layer Theory

In Fluid Mechanics, a fluid is characterized as "perfect" when it is possible to study its flow without considering its viscosity heat transfer. This kind of fluid does not exist in reality and

is generally only useful only for ideal mathematical representations. Let us consider a viscous fluid such as "air", which flows in front of a flat plate with a velocity equal to U_∞ and that passes over the plate. Since the effect of viscosity is resistance fluid motion, the velocity of the fluid close to the solid plate continuously decreases downward and finally is equal to zero at the overlapping region between the fluid and the plate; that is, the "no slip condition". But, far from the flat plate, the flow speed remains equal to U_∞ . Figure 1.5 shows the flow speed variation over a flat plate.

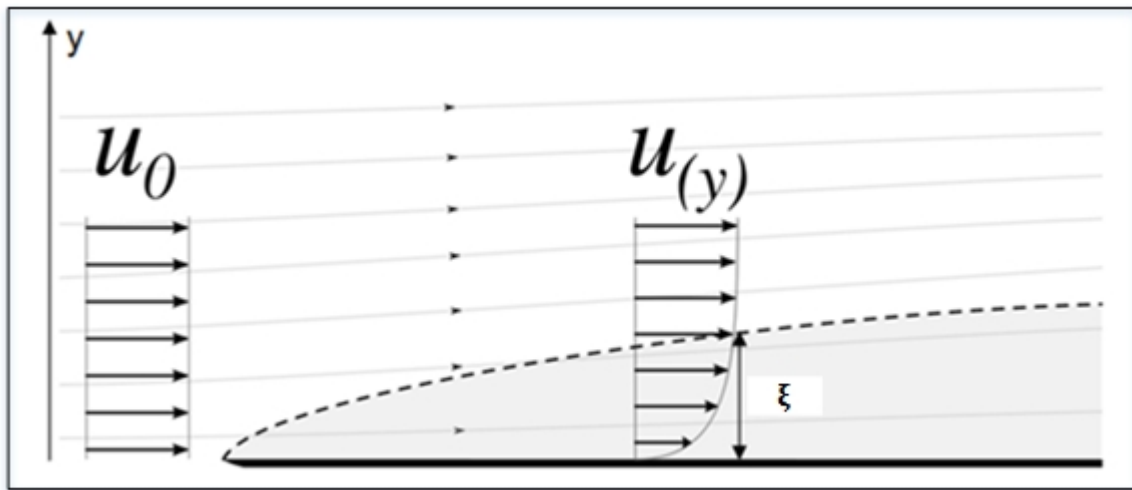


Figure 1.5 Boundary layer of a flow over a plane plate

The flow speed diagram presents two distinct regions. The first is the region near the plate, where the flow speed decreases downwards due to the friction between the fluid and the plate. This first region is called the boundary layer. The second region, called the main flow, is outside the above region and is not affected by the friction. The boundary layer thickness ξ is usually smaller than the main flow dimension, and is considered to be the distance from the flat plate surface to the point where the flow velocity reaches 99% of the main flow velocity. It depends on the non-dimensional Reynolds number.

In aerodynamics, the characterization of the flow over a wing within the boundary layer is an important factor, one with which both the wing lift and drag are quantified, as well as the evaluation of the heat transfer that occurs at high speeds. The boundary layer's nature can be

laminar or turbulent depending on the value of the Reynolds number. For low Reynolds values, the boundary layer is laminar and is characterized by fluid particles flowing smoothly and constantly in parallel layers due to the viscous forces that are dominant to inertial forces. On the contrary, turbulent boundary layers exhibit the high property changes and random flow patterns that are associated with high Reynolds numbers. The flow transition occurs at a critical Reynolds number value Re_{cr} lying between 2×10^5 and 3×10^6 , and is dependent upon the physical parameters of the tested model, such as the roughness and the curvature of the surface (Young *et al.*, 2010).

The passage from laminar to turbulent boundary layer does not happen instantaneously, but requires a certain length in the direction of the flow. This length is called the "laminar to turbulent transition zone". The boundary layer of the flow generally starts in its laminar state and can transition to a turbulent state following different path, depending on the initial flow conditions, such as its disturbance amplitude and surface roughness (Saric, Reed et Kerschen, 2002). In fact, even a slight perturbation can progressively grow and turn the most laminar flow into a complex turbulent one.

For many years, the theoretical understanding of the boundary layer transition process did not really advance; most of its current understandings are based on experimental results. However, the gap between theory and experimental knowledge has recently been attenuated following several research efforts (White, 2006, p 439).

There are several assumptions regarding the flow transition in boundary layer theories; they may diverge sometimes, but most of them agree on the existence of different phases through which the fluid flow passes. The linear and weakly non-linear phases of flow transition were fairly well understood (Herbert, 1988; Kachanov, 1994). However, many questions still remain regarding the late non-linear transition phases (Kleiser et Zang, 1991). These different phases are known as:

- "Receptivity": This phase consists of the transformation of the outside disturbance into perturbations within the boundary layers. The initial disturbance, which is quite small (often unmeasurable) at the basic state of the flow, grows at varying rates depending on its nature and the basic state behavior. Perturbations such as Tollmien-Schlichting (Ts) waves or crossflow instabilities begin (Schlichting, 1968). The Ts waves' disturbance is one of the more common methods by which a laminar boundary layer transitions to turbulence. Their theory and evolution through the boundary layer were fully described in Smith and Gamberoni (1956).
- "Linear instabilities": In this phase, the perturbations that originate in the receptivity stage remain two-dimensional and small enough that the linear stability theory (Mack, 1984) can be used to describe their evolution.
- "Secondary instabilities" (non-linear growth and vortex breakdown to turbulence): The amplitude of the linear perturbations continues to increase until the perturbations turn into three dimensions, so that the linear theory can no longer be applied. Nonlinear instabilities are characterized by temporal and spatial incoherence of the flow, and an expansion of the frequency bandwidth that would rapidly lead to the occurrence of turbulent flow.

1.4.2 Numerical Prediction of the Boundary Layer Transition: N-factor Method

The first version of the e^9 (later known as the e^N) method for the semi-empirical prediction of the transition of two-dimensional incompressible boundary layers was first implemented by Van Ingen (1956). This approach, even though it is based on linear stability theory (Mack, 1984), has been used to predict the laminar to turbulent transition, which is definitely a nonlinear phenomenon. The method was able to calculate the amplification e^N of the unstable perturbation (such as Ts waves or CF instabilities) in the laminar boundary layer according to the following equation:

$$N(x, f) = \frac{A(x, f)}{A(x_0, f)} \quad (1.1)$$

where $N(x, f)$ represents the linear amplification of a given perturbation mode of frequency f , on a varying length $x - x_0$. The transition is supposed to start when any amplitude A of any mode within the perturbation families reaches the threshold value A_T (Crouch et Ng, 2000). The beginning of the transition is then located by the Equation 1.2:

$$\max(A(x, f)) = A_T \quad (1.2)$$

which means that the transition flow begins for a certain value of the N factor, given by equation 1.1 for $A(x, f) = A_T$.

For a good prediction of the flow transition on an airfoil, the N factor value needs to be calibrated, as it incorporates the receptivity and physical parameters of the model such as the surface roughness and the characteristic length. Mack, (1977) provided one of the earliest attempts to systematically model the variation of the N factor associated with Ts-wave transition. Mack's empirical equation relating the turbulence intensity T_u to the N factor was written as follows:

$$N = -8.43 - 2.4 \ln(T_u) \quad \text{for } 10^{-3} \leq T_u \leq 2.10^{-2} \quad (1.3)$$

N factor method equations are implemented in many aerodynamic solvers, including Xfoil software. Therefore, this is the approach that has been used for the numerical prediction of the boundary layer flow transition of the various aerodynamic profiles within the CRIAQ MDO-505 project, and which has been further tested in the IAR-NRC subsonic wind tunnel for experimental validation of the numerical simulation results.

1.4.3 Experimental Determination of the Boundary Layer Transition Region

Many flow visualization techniques have been developed over the years to clarify aerodynamic phenomena; for example, where shock waves occur or whether the flow is laminar, turbulent or transitional. In the absence of flow visualization, the transition process can be very difficult to explain. Methods using Schlieren photography (Bracht et Merzkirch, 1977), tufts (Crowder, 1980) and oil flow visualization (Loving et Katzoff, 1959) were and continue to be used in wind tunnel and flight tests.

These experimental methods for characterizing the boundary layer are always based on physical flow parameters and their properties (such as pressure, temperature, and viscous forces), and they are different for laminar and turbulent regimes. They each have their advantages and limitations.

1.4.3.1 Color Changes in Liquid Crystal Coatings

Originally discovered in 1888, the Liquid Crystal Method has been applied in the Aerospace industry for aerodynamic investigations in wind tunnel tests for boundary layer transition measurements. The method is based on the liquid crystal's change of color when the liquid crystal is subjected to changes in shear stress, temperature or pressure. The color changes should be noticeable enough to differentiate a turbulent boundary layer from a laminar one (Holmes *et al.*, 1986).

A complete review of the current thermochromic liquid crystal products was produced by Hallcrest, in which the chemical, physical and reference temperature bands were indicated for transition detection.

This transition detection method was applied by Holmes *et al.*, (1986), in which they were able to visualize the laminar to turbulent boundary layer transition. When the liquid crystal coating was applied on the model, the coating needed to have a uniform thickness over the

whole model surface to obtain the maximum level of clarity in transition pattern development.

The method has the advantages that the changing color of the crystal coating is reversible and that its time response is under 0.2 seconds (Holmes *et al.*, 1986), even though the performance of the airflow model can be affected by coating imperfections.

1.4.3.2 Oil Film Interferometry

The oil film interferometry method was theoretically proven and experimentally validated by Tannera and Blows, (1976). This method is based on the behavior of a silicon oil film placed on a surface and subjected to a flow. Tanner and Blows demonstrated that the evolution of the oil film motion during the experiment can only be related to the skin friction resulting from the flow boundary layer if the oil film remains thin enough (on the order of 10 μm). The product of "oil film thickness" and "time" becomes constant over time (for a given position x of oil film on the model). The "oil film thickness" is measured using the "Fizeau interferometry technique", based on "laser ray reflection". The measuring procedure is fully described in Sykora and Holmes, (2011). The measured thickness of the oil film is representative of the skin friction over the surface model, allowing the distinction between the laminar and the turbulent boundary layers.

Oil film interferometry was successfully applied in several wind tunnel tests to characterize the boundary layer properties of models as part of the development of long-endurance aircraft designed to extend the laminar flow region for drag reduction (Drake, 2010).

This method presents advantages in terms of its low cost of materials and equipment, but the measuring procedure takes a relatively long time and is very sensitive.

1.4.3.3 InfraRed (IR) Thermography Visualization

Theoretically, laminar and turbulent boundary layers exhibit different behaviors in convective heat exchange. A turbulent boundary layer is marked by a transfer coefficient higher than the laminar one. The difference between the experimental model temperature and the flow temperature will attenuate more rapidly in a turbulent flow than in a laminar flow regime (Crawford *et al.*, 2013). For example, a cold surface will heat faster under the influence of a turbulent boundary layer than in a laminar boundary layer. The principle of using InfraRed (IR) visualization for transition detection is based on this difference in the rate of the heat transfer characterizing a laminar versus a turbulent regime.

Generally, the initial temperature of the experimental model should be different than the flow temperature. To be assured of this initial difference, the experimental model could then be cooled or heated depending on the expected temperature of the flow, which should ideally remain constant over time. In this way, the temperature change of the model's surface will largely depend on the heat transfer capacity of the flow, and thereby differentiate between the laminar flow and the turbulent regime.

The experimental setup for the IR visualization required two additional main components: an InfraRed camera and an insulator. The infrared camera was used to capture the temperature distribution along the model's surface area. An insulator is required to eradicate any heat signature resulting from the model's components, which could be significant enough to overshadow any heat transfer occurring from flow effects, including flow transition (Joseph, Borgoltz et Devenport, 2014). The insulator should be smooth enough to preserve the model airfoil so that the aerodynamic performance is not altered. Joseph, Borgoltz, and Devenport (2014) used a coating (paint) as an insulator for the IR camera detection of the laminar to turbulent boundary layer in both wind tunnel and flight test environments.

The IR visualization technique has the advantage of being non-intrusive, as all of the equipment is external to the model, and therefore does not alter the airflow.

1.4.3.4 Second Derivative of the Pressure Distribution

Several methods for distinguishing the laminar from the turbulent regime are based on the pressure distribution of an airfoil.

Popov et al., (2008) theoretically and experimentally demonstrated that the transition zone can be localized by detecting the pressure step increase in the pressure distribution. This pressure step increase had earlier been identified and explained by Galbraith and Coton (1990) as representing the separation bubble that appears in the boundary layer during the flow transition process. Figure 1.6 shows a pressure distribution on the NACA 4415 airfoil predicted by Xfoil software, in which the predicted transition zone is visible as an increase in the pressure step (Popov, Botez et Labib, 2008).

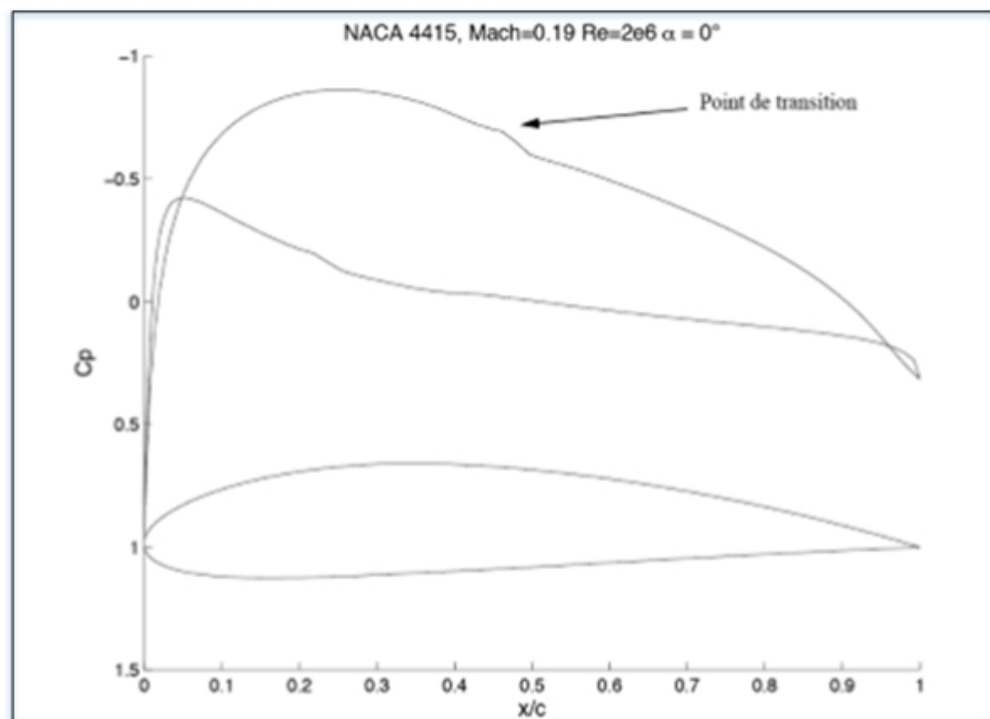


Figure 1.6 Pressure distribution of a NACA 4415 profile for a Mach number of 0.19, a Reynolds number of $2e6$ and an angle of attack of 0 degrees (Popov et al., 2008)

The method proposed by Popov, Botez and Labib (2008) has shown that the maximum of the second derivative of the pressure distribution with respect to x corresponds to the maximum curve of the pressure plot, which represents the beginning of the transition.

To experimentally verify their theory, Popov, Botez and Labib (2008) designed a NACA 4415 airfoil wing, for which the upper surface of the model was equipped with 84 pressure sensors, so that the pressure distribution could be detected with sufficient accuracy. Both the Spline and the PCHIP (piecewise cubic Hermite interpolating polynomial) (Hussain and Sarfraz, 2009) methods were used for interpolation between the local points recorded by the sensors before applying the second derivative method. Figure 1.7 and Figure 1.8 show an interpolated C_p distribution of the NACA 4415 airfoil and second derivative of its pressure distribution respectively, wherein the maximum second derivative value is identified at 48.1% of the chord.

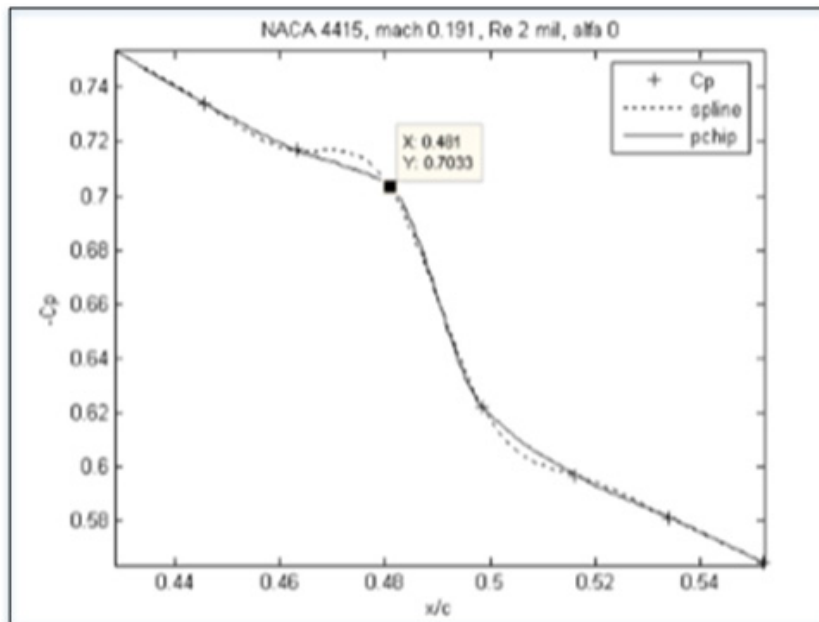


Figure 1.7 Pressure coefficient distribution in the vicinity of the transition point interpolated using the Spline and PCHIP methods.

Taken from Popov et al., (2008)

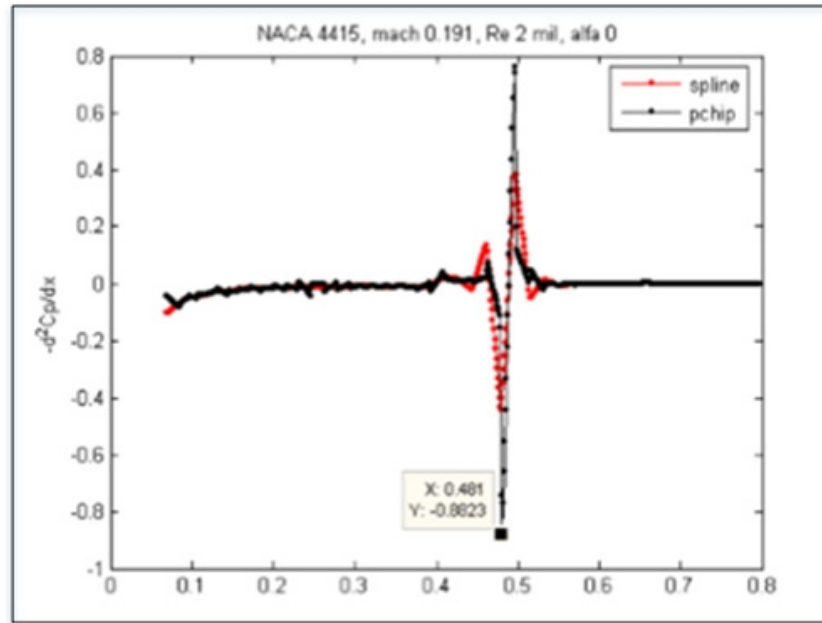


Figure 1.8 Second derivative of the pressure coefficient distribution interpolated using the Spline and PCHIP methods.
Taken from Popov *et al.*, (2008)

This method has a huge advantage in that it can detect the transition in real time, but it requires a significant number of pressure sensors to obtain a high level of accuracy, which can be a practical disadvantage for a model with a large area.

1.4.3.5 Pressure Distribution Spectral Analysis

While Popov, Botez and Labib (2008) focus on deviations of the mean pressure over the total wing chord, the spectral analysis method considers the recorded pressure fluctuations over time to evaluate which sensors belong to the laminar and which to the turbulent zone. The pressure fluctuations are expected to be more intense in a turbulent flow than in a laminar one (Parameswaran and Jayantha, 1999), due to the amplification of the nonlinear perturbations occurring during the transition. Therefore, this method mainly utilizes the difference in pressure fluctuations to determine the transition area.

The pressure fluctuations are visualized and quantified by means of Fast Fourier Transforms (FFT) (Mathworks, 2006) and Standard Deviation (SD) algorithms (Mathworks, 2006) applied on the recorded data. This approach was applied by (Popov *et al.*, 2010) to experimentally determine the transition area of several optimized airfoils for multiple wind tunnel tests during the CRIAQ 7.1 morphing wing project. Their model was equipped with 16 Kulite piezoelectric sensors, capable of sensing high frequency fluctuations of up to 10 KHz. The Kulite transducers present many other advantages, such as their relatively small size and their very precise and accurate measurements and accuracy. Thirty-six optimized airfoils for drag reduction were found for the flight cases expressed by combinations of Mach numbers 0.2, 0.225, 0.25, 0.275, 0.3 and angles of attack -1, -0.5, 0, 0.5, 1 and 2 degrees (Popov *et al.*, 2010).

The good correlation between the experimental methods and the Xfoil numerical simulations results obtained during the CRIAQ 7.1 project led to the choice of the pressure distribution spectral analysis for the experimental determination of the laminar to turbulent transition area in the CRIAQ MDO 505 project.

1.5 Aeroelastic Behavior and Vibration Measurements of a Wing

1.5.1 Aeroelastic Behavior

Flight and wind tunnel testing on wing models always involve some vibrations studies, as vibrations should be minimized, not only to preserve the wing's aerodynamic performance, but also to ensure the safety of all the operators around the model. Courchesne, Popov and Botez (2010) performed aeroelastic studies to avoid possible flutter occurrences during wind tunnel testing on a morphing wing model. Their analysis showed that the wind tunnel tests could be performed safely because aeroelastic instabilities for the studied morphing configurations could only occur at Mach number 0.55, which was higher than the wind tunnel Mach number limit speed of 0.3.

Flore and Cubillo (2015) studied the dynamical behavior of an aircraft wing structure. They analyzed the change of the dynamic behavior of the wing structure relative to the applied loading to simulate real aircraft operating conditions. During experimental tests, they proved that both strain gages and accelerometers could be used for vibration sensing with satisfactory results.

1.5.2 Strain Gages

Omega Engineering, (2000) defines a strain gage as a device for indicating the strain of a material or structure at the point of attachment. It uses the change in electrical resistance to measure strain when it is subject to mechanical motions. Strain gages can have several applications, such as in shock analysis and vibration measurements. The displacement measurements are accomplished by using the proportional relation between the deflections of a loaded mechanical member and the strains at every point in the member, as long as all strains are within their elastic limits. Wilson, (1976) gave a complete review of strain gage instrumentation at that time. Strain gage theory and applications have been widely represented. Pisoni *et al.* (1995) and Burrows (1975) used strain gage equipment for the real time determination of displacements at various points of a vibrating body; this information could be especially valuable for position control measurements of aeroelastic systems.

1.5.3 Accelerometers

Accelerometers are sensors that measure the acceleration of the body they are installed on. Such a device can be used for many applications, including tilt sensing (Chendjou et Botez, 2014), shock quantification (Broch, 1980), and vibration measurements (McFadden et Smith, 1984). Several types of accelerometers are available. The most common types are piezoelectric and Micro Electro-Mechanical System (MEMS) accelerometers.

Albarbar *et al.*, (2009) provided detailed information about MEMS accelerometers performance, describing the devices high level of performance despite their relatively low

cost. MEMS accelerometers were therefore selected for use in the CRIAQ MDO-505 project to sense and measure vibration data for the experimental validation of aeroelastic studies on the model (Koreanschi *et al.*, 2016).

CHAPTER 2

PRESSURE DATA ACQUISITION SYSTEM AND POST PROCESSING METHODOLOGY

2.1 Context

One of the main objectives of the MDO 505 project was to improve the aerodynamic performances of a morphing wing prototype by delaying the occurrence of the laminar to turbulent boundary layer transition zone. The success of the experimental tests in the IAR-NRC wind tunnel relied on the validation of the numerical predictions. This validation necessitated an accurate experimental characterization of the airflow, which includes both a reliable data acquisition system and reliable post-processing methods, as well as correct interpretations of the post-processed results. The frequency analysis method of the pressure distribution airflow was chosen for detecting the transition zone location at the chord situated at 40% of the wing span. The sensors' measurements should be accurate enough to determine the pressure distribution over this wing section airfoil, and they should have a sufficiently large bandwidth to capture the pressure fluctuations resulting from the Tollmien-Schlichting waves. The Infra Red thermography visualization over the wing surface was used as supplementary method to detect the transition over the whole wing span. A wind tunnel balance was also used to evaluate the load variations (lift, drag, moments) resulting from the morphing procedure.

This chapter first fully describes the wing model. This is followed by a description of the real time acquisition system equipment, as they are used to gather the pressure data. The description focuses on the pressure sensors and their characteristics. Next, the post processing procedures for obtaining the C_p distribution profile and for determining the laminar to turbulent boundary layer transition are detailed. The interpretation of a sample case is presented to clarify the procedure. More results are displayed in Chapter 4.

2.2 Description of the Wing Model

The wing model had the dimensions of a real aircraft wing tip (wing and aileron), provided by Bombardier (one of the project's partners), which was representative of their type of transport aircraft and capable of withstanding 1g in-flight loads. The wing prototype measured 1.5 meters for its span, and its root chord was also 1.5 meters, with a taper ratio of 0.72 and a leading edge sweep angle of 8 degrees. The adaptive upper skin, designed and optimized from carbon material composite, was situated between 20% and 65% of the chord. Figure 2.1 presents the wing-tip model dimensions and its internal structure.

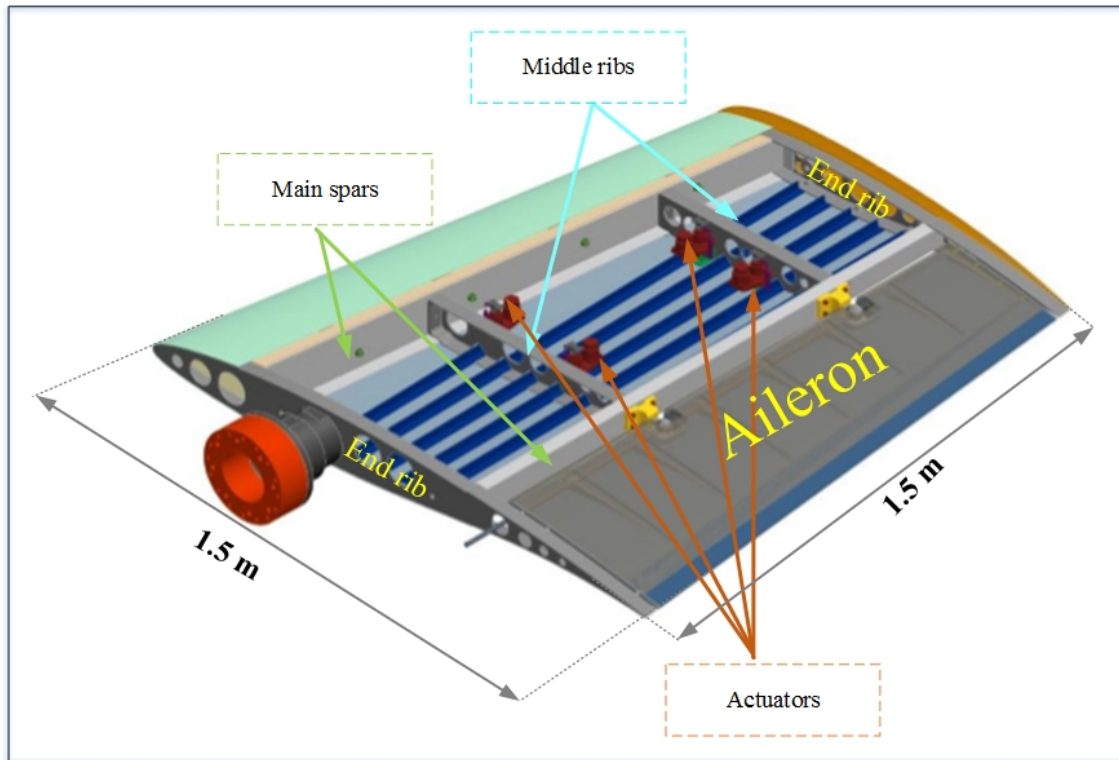


Figure 2.1 Internal structure of the wing model

The wing's internal structure was mainly manufactured from Aluminum and had four ribs, two main spars and two secondary spars (showed in blue on Figure 2.1), reinforcing the lower and upper skins. The wing's flexible upper skin was manufactured from composite materials (Michaud, Joncas et Botez, 2013). It therefore had the capacity of changing its

shape in order to efficiently withstand different load conditions. To realize the desired shape changing, four electrical actuators distributed along two lines (32% and 48% of the chord) were installed inside the wing. The actuators were supported by the two middle ribs, which acted as embedment supports. The two ends ribs and spars ensured a satisfactory rigidity of the wing, as required by industry specifications, despite its flexibility.

2.3 Real Time Acquisition System for Pressure Measurements: Kulite Transducers Setup and their Installation on the Wing.

The sensors used for the pressure distribution and for flow transition detection during the wind tunnel tests were ultra-miniature Kulite XCQ-062 pressure transducers. They are manufactured and distributed by Kulite Semiconductor. The Kulite XQC-062 transducers measure the differential pressure between two pressure points of the system. The first point is the local pressure on the model and the other is the referenced static pressure of the Wind Tunnel test section. This differential pressure is then proportionally converted into a displacement by using a force-summing device over a wide range of frequencies. The displacement is in turn, applied to an electrical transducer element (composed of a Wheatstone bridge plus a temperature compensator) in order to generate the required electrical output signal. Figure 2.2 presents a graphical representation of the Kulite XCQ-062 transducer as well as a photographic image.

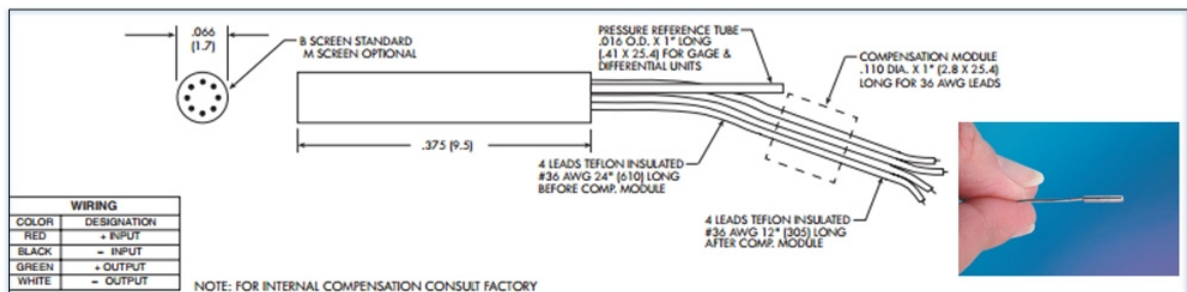


Figure 2.2 Graphical representation of Kulite XCQ-062 transducer (Annex I)
Adapted from Kulite Semiconductor (2014)

The force-summing device and the transducer element are physically combined into a micro-machined dielectrically isolated silicon diaphragm of dimensions 1.5 mm *9.5 mm, which has a reliable stiffness and a negligible mass. This diaphragm confers excellent properties to the Kulite sensors such as a wide frequency response, high sensitivity and immunity to acceleration and strain inputs, as seen in Annex I.

To install the Kulite sensors on the upper skin of the model, holes of 1.7 ± 0.005 mm were made on its surface, and sensors were perpendicularly set from the inside to the outside of the wing, ensuring that the sensors' extremities were aligned with the composite skin surface, as shown on Figure 2.3.

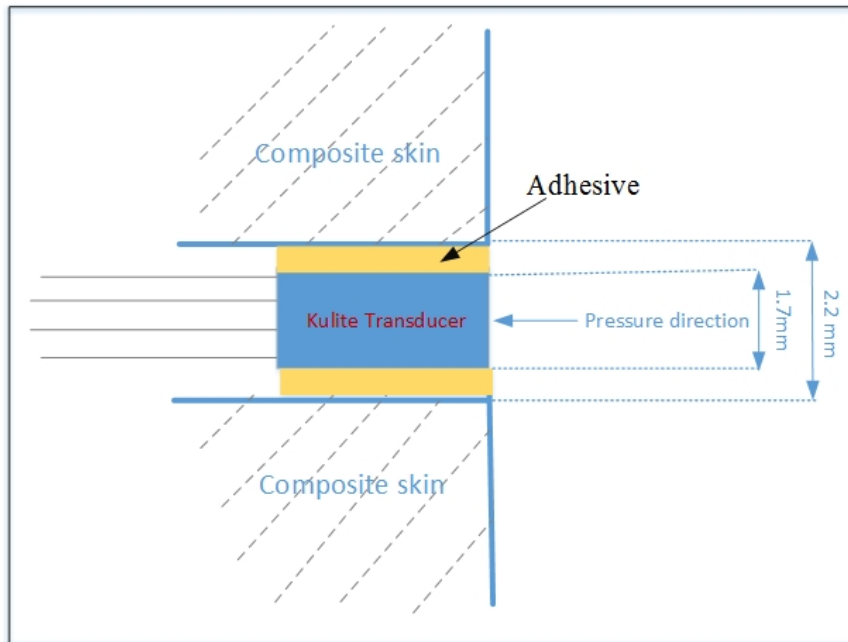


Figure 2.3 Sketch of a Kulite sensors installation on the composite skin

The sensors' positions were reinforced by using an adhesive (shown in yellow on Figure 2.3) to keep it fixed despite the vibration that generally occurs during the wind tunnel tests. Figure 2.4 displays the inside surface of the composite skin of the wing; the yellow circles indicate where the pressure sensors are installed.

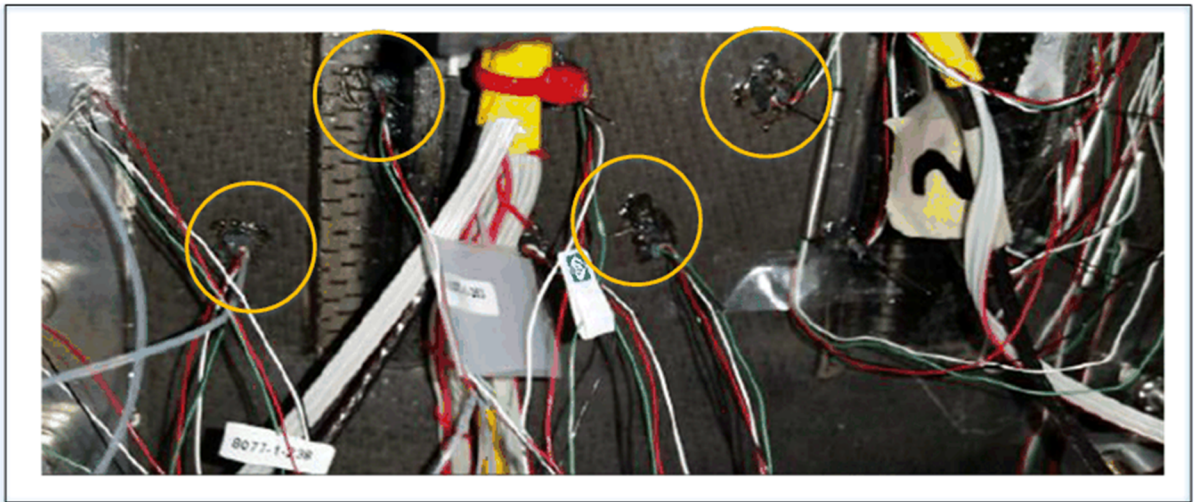


Figure 2.4 Inside surface of the composite skin

The real time acquisition system for Kulite pressure measurements was composed of a NI PXIe-1078 chassis equipped with a central processing unit, four NI PXIes-4330's each capable of handling eight analog inputs, with a sampling rate of up to 25,000 samples per second for each channel. A personal computer was also connected via an Ethernet network to the NI PXIe-1078 to monitor the data and handle their real-time visualization. Finally, a voltage source supplied the NI systems and the Kulite transducers. The connections between the different components are shown in Figure 2.5.

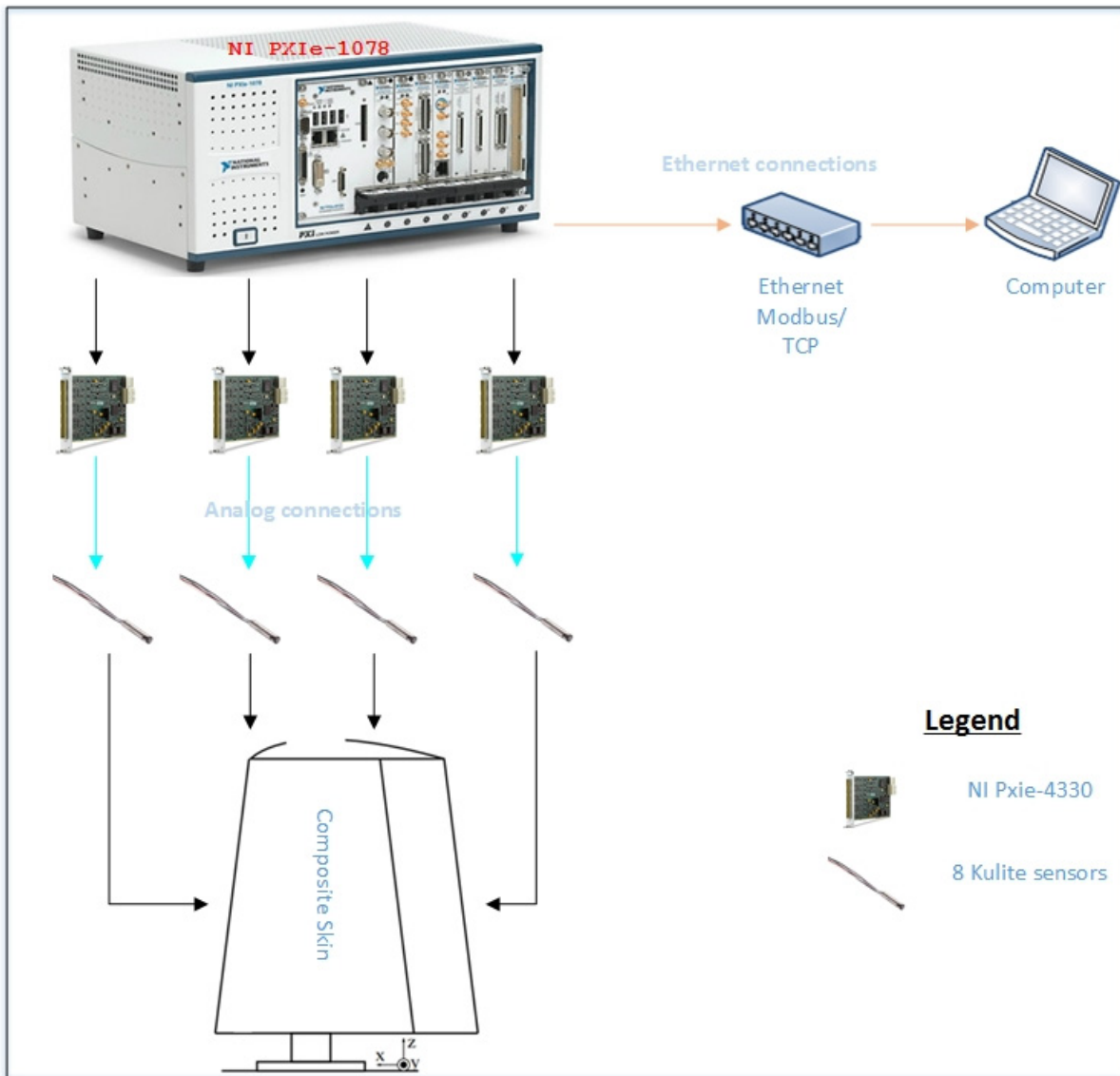


Figure 2.5 Overview of the pressure data acquisition system and connections between the components

Thirty-two Kulite sensors were installed on the wing model. They were disposed on the upper skin surface along two chord lines situated at 600 mm and 625 mm from the wing root, between 28% of the chord and 69% of the chord. Two successive sensors had a minimum distance between them of 30 mm and a maximum distance of 40 mm in order to avoid interferences, but also to minimize their pressure information losses. Figure 2.6 shows the representation of the Kulite sensors' disposition on the wing-tip.

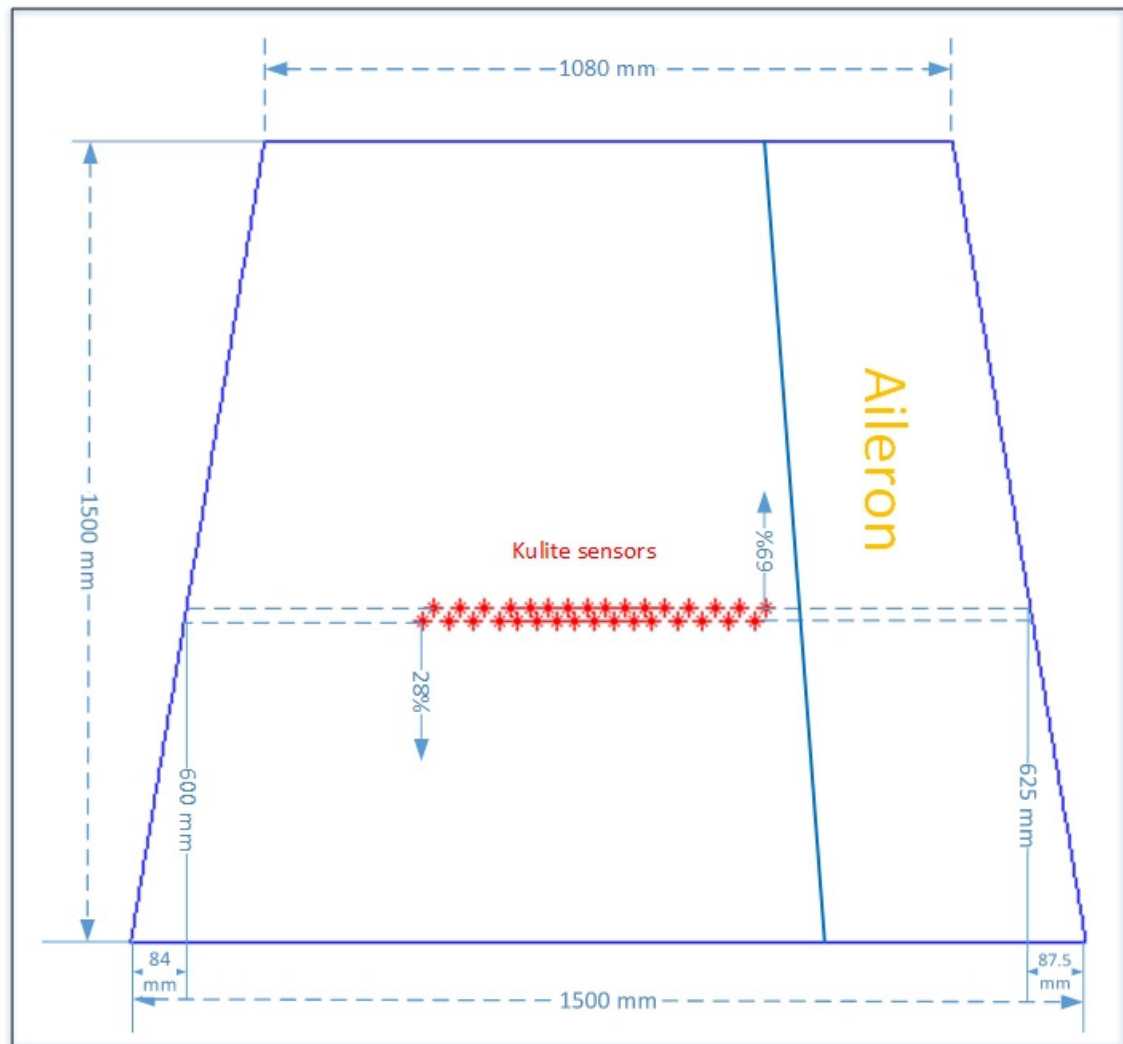


Figure 2.6 Representation of the wing dimensions and Kulite sensors distribution on the composite skin surface

Each Kulite sensor was therefore positioned at a percentage of chord, as presented in Table 2.1

Table 2.1 Chord percentage at which Kulite sensors are positioned on the wing

Sensor #1 : 28.5 %	Sensor #17 : 51.2 %
Sensor #2 : 29.5 %	Sensor #18 : 52.6 %
Sensor #3 : 33.4 %	Sensor #19 : 53.5 %
Sensor #4 : 35.2 %	Sensor #20 : 54.6 %
Sensor #5 : 36.3 %	Sensor #21 : 55.7 %
Sensor #6 : 37.5 %	Sensor #22 : 56.9 %
Sensor #7 : 38.2 %	Sensor #23 : 57.2 %

Table 2.1 (continued)

Sensor #8 : 39.1 %	Sensor #24 : 58.7 %
Sensor #9 : 41.3 %	Sensor #25 : 60.2 %
Sensor #10 : 42.4 %	Sensor #26 : 61.5 %
Sensor #11 : 43.6 %	Sensor #27 : 62.8 %
Sensor #12 : 44.3 %	Sensor #28 : 63.8 %
Sensor #13 : 45.2 %	Sensor #29 : 65.4 %
Sensor #14 : 46.2 %	Sensor #30 : 66.0 %
Sensor #15 : 50.0 %	Sensor #31 : 67.7 %
Sensor #16 : 50.8 %	Sensor #32 : 68.3 %

The Kulite sensors outputted differential pressure variations from 0 to 5 PSI in terms of tension, with a sensitivity of 20mv/PSI. These sensors also had an infinitesimal resolution and a natural frequency range of 150 KHz. The analog signal was conditioned by means of an anti aliasing filter incorporated in the NI PXIe-1078 chassis. The resulting output signal was sampled at the rate of 20 KHz, so that the pressure fluctuations from 0 to 10 KHz could be visualized through Fast Fourier Transform (FFT) representation. This rate was high enough to capture the nonlinear instabilities that occurred during the transition process. In fact, following the Nyquist-Shannon theorem (Bellanger et al., 2013), the sampling rate should at least be twice the highest frequency of the desired visualized signal for an accurate conversion of analog to discrete signals.

2.4 Numerical Aerodynamic Optimization and Prediction of the Performances of the Wing Airfoil

Before performing wind tunnel tests, the optimized airfoils for the various flight conditions were obtained by using a genetic algorithm developed 'in-house' (Koreanschi, Sugar-Gabor et Botez, 2014). Subsequently, numerical predictions of both the pressure coefficients and the transition area of the multiple airfoil configurations were achieved by using the Xfoil 6.96 open source aerodynamic solver, which were further confirmed using Fluent software. The prediction of the transition area through the Xfoil solver was based on the *N*-factor method described in section 1.4.2. Simulations on the Xfoil solver required the several parameters,

such as the coordinates of the airfoil we wanted to analyze, the Mach number, the angle of attack, the deflection angle of the aileron and the Reynolds number.

Ninety seven (97) different flight configurations were simulated, optimized for transition delay and further tested at the IAR-NRC wind tunnel for validation of their simulation results. Mach numbers of 0.15, 0.2 and 0.25 were considered as airspeeds. The angle of attack varied from -3° to 5° , while the aileron deflection angles changed from -6° to 6° . The Reynolds number was calculated from the air characteristics and the model dimensions (length L), as shown in equation 2.1:

$$Re = \frac{\rho V L}{\mu} \quad (2.1)$$

Where,

- $\rho = 1.225 \text{ Kg. m}^{-3}$ is the air density of air at the wind tunnel test conditions
- V is the airspeed which depends on the flight test configuration chosen
- $L = 1.32 \text{ m}$ is the characteristic length, which is equal to the length of the sensors chord line; and
- $\mu = 1.80 \cdot 10^{-5} \text{ Kg. m}^{-1} \cdot \text{s}^{-1}$ is the dynamic viscosity of the air.

Eighteen of the ninety-seven flight configurations are summarized in Table 2.2.

Table 2.2 Tested cases optimized for laminar flow improvement

Flight case number	Mach Number	Angle of attack	Aileron deflection	Reynolds number
15	0.15	-0.5	6	4.67
18	0.15	-2	-2	4.62
25	0.15	1.5	-2	4.66
38	0.25	0.5	-1	7.77
40	0.15	1	0	4.67
41	0.15	1.25	0	4.66
42	0.15	1.5	0	4.65

Table 2.2 (continued)

43	0.15	2	0	4.64
44	0.15	2.5	0	4.65
45	0.15	3	0	4.66
47	0.15	-2.5	2	4.66
68	0.2	0	4	6.22
69	0.2	0.5	4	6.23
70	0.2	1	4	6.23
71	0.2	1.5	4	6.22
72	0.2	2	4	6.25
80	0.2	3	-4	6.19
82	0.2	5	-4	6.18

2.5 Description of the Wind Tunnel Post Processing Procedure

The waveforms recorded during the wind tunnel tests contained pressure data from the 32 different sensors installed on the composite skin (Figure 2.3). The data were recorded at the rate of 20 KHz for each sensor channel, and the recording procedure was repeated for ninety-seven different flight configurations on the morphing wing and on the un-morphed wing. The data were processed and further interpreted with the aim of validating the numerical simulation results by comparing them to the pressure coefficient distributions resulting from wind tunnel data. An evaluation of the backward motion of the transition area as a positive effect of the applied morphing was also performed.

2.5.1 Pressure Coefficient Distribution

For the generation of the pressure coefficient distribution over the wing airfoil, conventional pressure tab sensors were used to record static pressure measurements on the rest of the wing section (inner surface and aileron), since the Kulite sensors were only installed on the composite skin upper surface.

The pressure coefficient for each sensor is computed from the row data by using equation 1.4:

$$C_p = \frac{\Delta P}{\frac{1}{2}\rho U^2} \quad (2.2)$$

where ΔP is the mean pressure of each sensor recorded data, ρ is the air density and U is the flow velocity. Figure 2.7 presents a comparison between the numerical and experimental pressure coefficients for the wing section located at 40% of the span (Kulite sensor line chord), for flight case #15 (Mach=0.15, $\alpha=-0.5^\circ$, $\delta=6^\circ$).

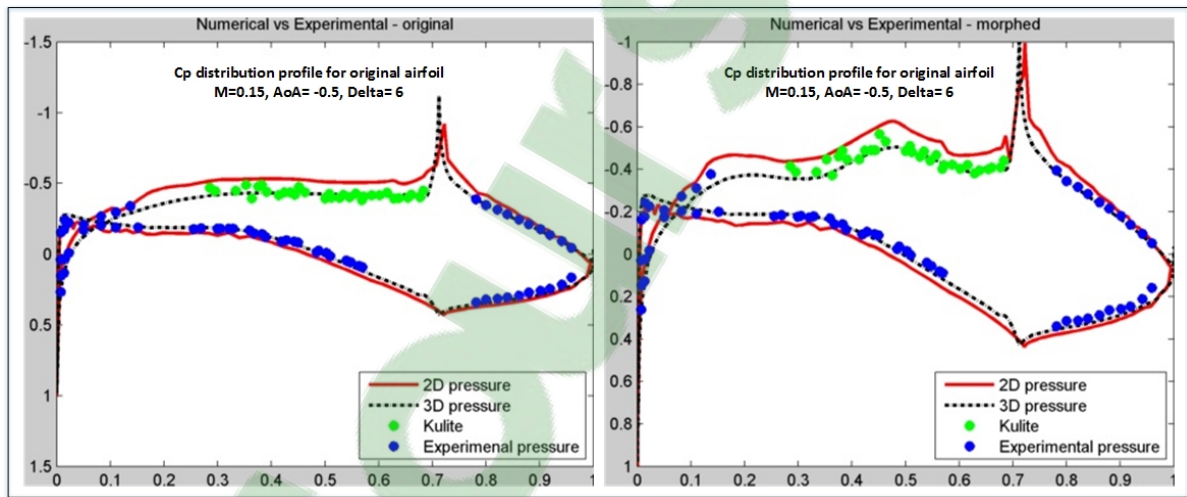


Figure 2.7 Comparison of the numerical versus the experimental pressure coefficient distribution for flight case #15; original airfoil (left) and optimized airfoil (right)

From Figure 2.7, an acceptable similarity between the 2D numerical predictions and the wind tunnel tests results can be observed for flight case #15 (Table 2.2). As expected, a very good agreement is observed between the 3D numerical and the experimental pressure values. The influence of the surface change due to morphing can be clearly observed from the original to the optimized airfoil pressure coefficients, measured on the interval situated between 28% and 68% of the chord (Kulite sensor region is represented in "green" in Figure 2.7). In fact, the skin morphing extends the wing upper surface laminar region where the air accelerates, and therefore generates more favorable conditions for laminar flow. This effect is clearly visible on the left and right hand sides of Figure 2.7.

2.5.2 Laminar to Turbulent Boundary Layer Detection

2.5.2.1 Architecture of the Post Processing Software

The data processing for estimating the laminar to turbulent boundary layer transition area was performed by filtering the raw data to eradicate unwanted noise. The resulting data was then visualized according to Power Spectrum Density (PSD) and Standard Deviation (SD) visualizations of the pressure distribution. To visualize the pressure fluctuations (in each Kulite sensor's recorded data) using Power Spectrum Density (PSD), the Fast Fourier Transform (FFT) algorithm was applied to consecutive frames of 1024 pressure data points, for a good frequency resolution. After the acquisition rate was set to 20 KHz, the frequency resolution was assumed to be about 19.5 Hz, which was small enough for our purpose of transition detection. Each 1024-point data frame was divided into 25 segments (possibly overlapping) before computing the PSD. The obtained PSDs were averaged following Welch's Method (Mathworks, 2006) to reduce the variance of the Power Spectrum Density estimate of the entire frame.

Standard Deviation (SD) is a measure that quantifies the amount of variation of a set of values around their average point (Mathworks, 2006). The SD is therefore representative of the amplitude of the pressure fluctuations detected by each sensor. For a discrete set of N pressure data, the standard deviation ΔP_{SD} is given by equation 2.3.

$$\Delta P_{SD} = \sqrt{\frac{1}{N} \sum_{i=1}^N (\Delta P_i - \Delta P)^2} \quad (2.3)$$

where ΔP_i is the i th recorded pressure and ΔP is the arithmetic mean of all the recorded pressures.

Before computing the standard deviation (SD), the raw signal was high pass filtered at 1 KHz, and band pass filtered around 5 KHz with the aim of erasing all possible noises caused by either the wind tunnel or the aileron actuator's motor. We considered as noise each peak that appeared on every pressure sensor (not necessarily with the same amplitude) regardless of the angle of attack, the morphing of the wing shape or the aileron deflection, as illustrated in Figure 2.8.

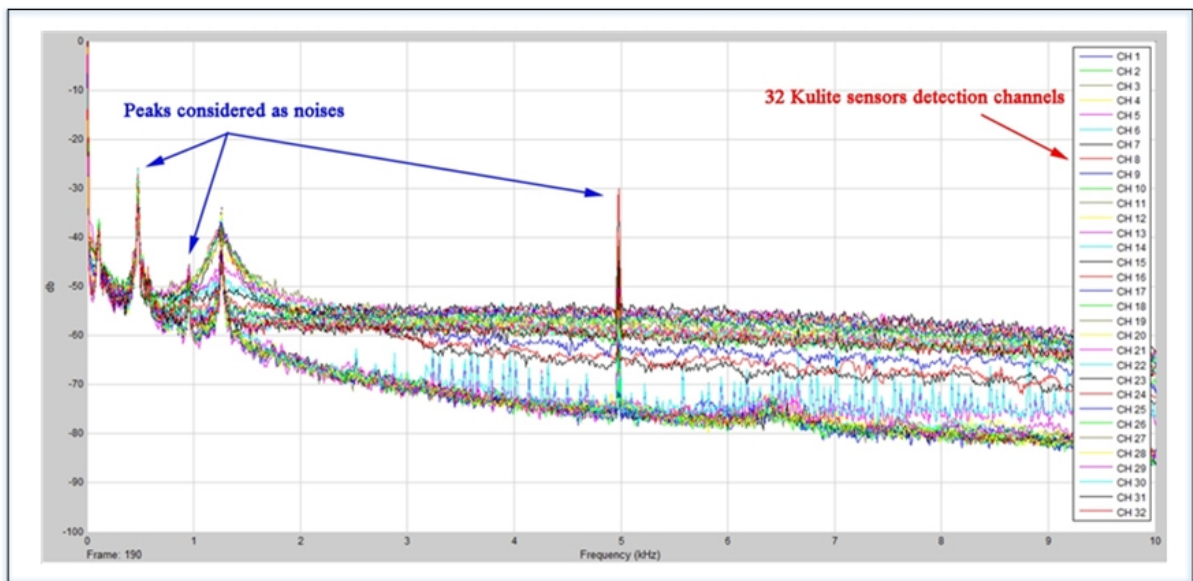


Figure 2.8 Noises representation of the thirty-two sensors' power spectrums

To obtain a good match between the Power Spectrum Density and the Standard Deviation plots, both were computed instantaneously for every data frame (1024 data points per frame). To be sure that the 1024- data points frame chosen for interpretation was representative enough of all the recorded points, we first computed the "average SD" of all the recorded data points, and compared them with the instantaneous ones (previously saved). The comparisons between the "average SD" and the "instantaneous SDs" were achieved by the use of a mean square error algorithm. To preserve the good correlation (match) between the PSD and the SD, we chose to interpret the instantaneous SD that was the closest to the average, and the PSD graph that corresponded to it. Figure 2.9 shows the process described above.

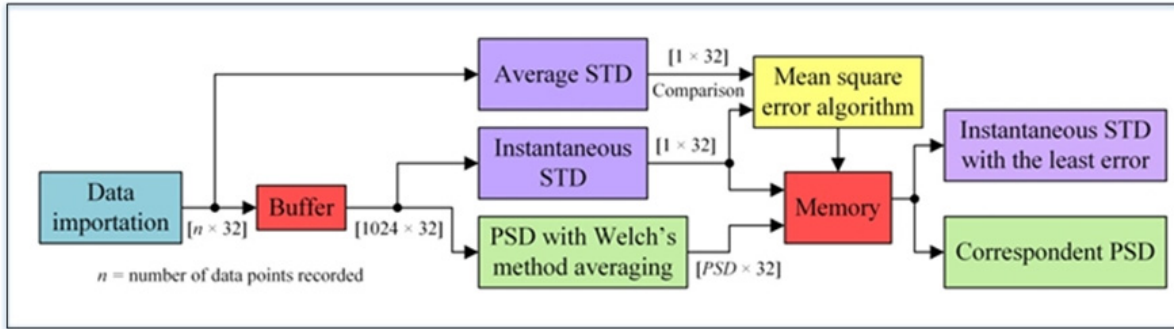


Figure 2.9 Block diagram of the pressure data Post processing software

2.5.2.2 Interpretation Procedure of the Obtained Results

For illustration, the results are interpreted here only for the original and the optimized airfoils subjected to flight case#68 (Mach=0.2, $\alpha=0^\circ$, $\delta=4^\circ$). More interpretations and comparisons of results are presented in Chapter 4.

To interpret the SD and PSD results, the flow was considered to be transitional in a chord region delimited by two distinct sensors. The first is the sensor from which the power spectrum amplitudes began to be greater than the amplitudes of the previous sensors, showing the increase of the flow's pressure fluctuations. This sensor position represents the beginning of the transition area. The second sensor measured the maximum of the standard deviation plot, showing the maximal fluctuation of the flow, and thus the end of the transition area (indicating the beginning of the turbulent region).

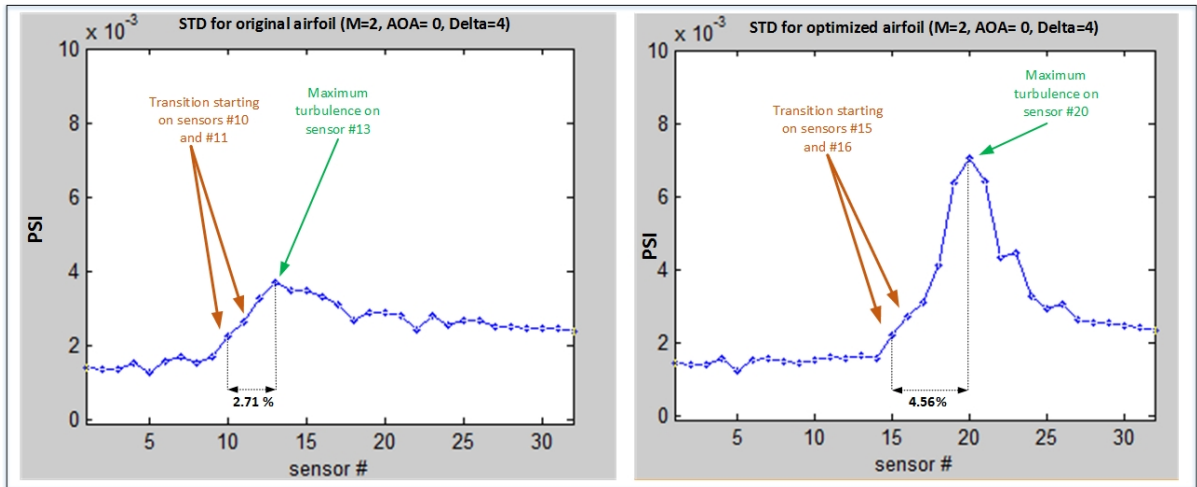


Figure 2.10 Standard deviation of the pressure data acquired for flight case #68; original airfoil (left) and optimized airfoil (right)

The Standard Deviations (SDs) for pressure data acquired for flight case #68 (Mach=2, $\alpha=0^\circ$, $\delta=4^\circ$) are presented in Figure 2.10 for both un-morphed (original) and morphed (optimized) airfoils. From the SD related to the un-morphed airfoil on the left, it is clear that the transition began at sensor #10, which is positioned at 42.45% of the chord; while for the optimized airfoil, the transition appeared at sensor #15, positioned at 50.04% of the chord. In addition, the maximum level of turbulence, indicating the end of the transition area, was found at sensor #13 (45.16% of the chord) for the original airfoil and at sensor #20 (54.60 % of the chord) for the optimized airfoil.

The PSD plots associated with the same flight configuration (case #68) show the pressure fluctuations in term of frequencies for the original airfoil (Figure 2.11) and for the optimized airfoil (Figure 2.12). The 32 channels are grouped as follows in the first four graphs: "ch1-8", "ch9-16", "ch17-24" and "ch25-32". The fifth graph in each figure depicts the results for all 32 channels; this centralized representation was performed to better observe the FFTs curves' detachment in correlation with the first four graphs.

When analyzing the PSD curves, the data from sensors #12 and #16 were found to be influenced by parasitic noises and were therefore not considered in the post processing procedure. A good correlation can be observed between the FFT curves and the STD plots.

In Figure 2.11's representation of the un-morphed airfoil, sensor #10's measurement is slightly detached from the lower FFT curves' package, indicating the beginning of the transition zone. A more visible separation appears at the position of sensor #11, producing the flow transition to the upper FFT curves' package.

For the optimized airfoil, represented in Figure 2.12, the FFT plots suggest that the transition begins at sensor #15, and that the maximum level of turbulence appears in the region delimited by sensor #19 to sensor #21.

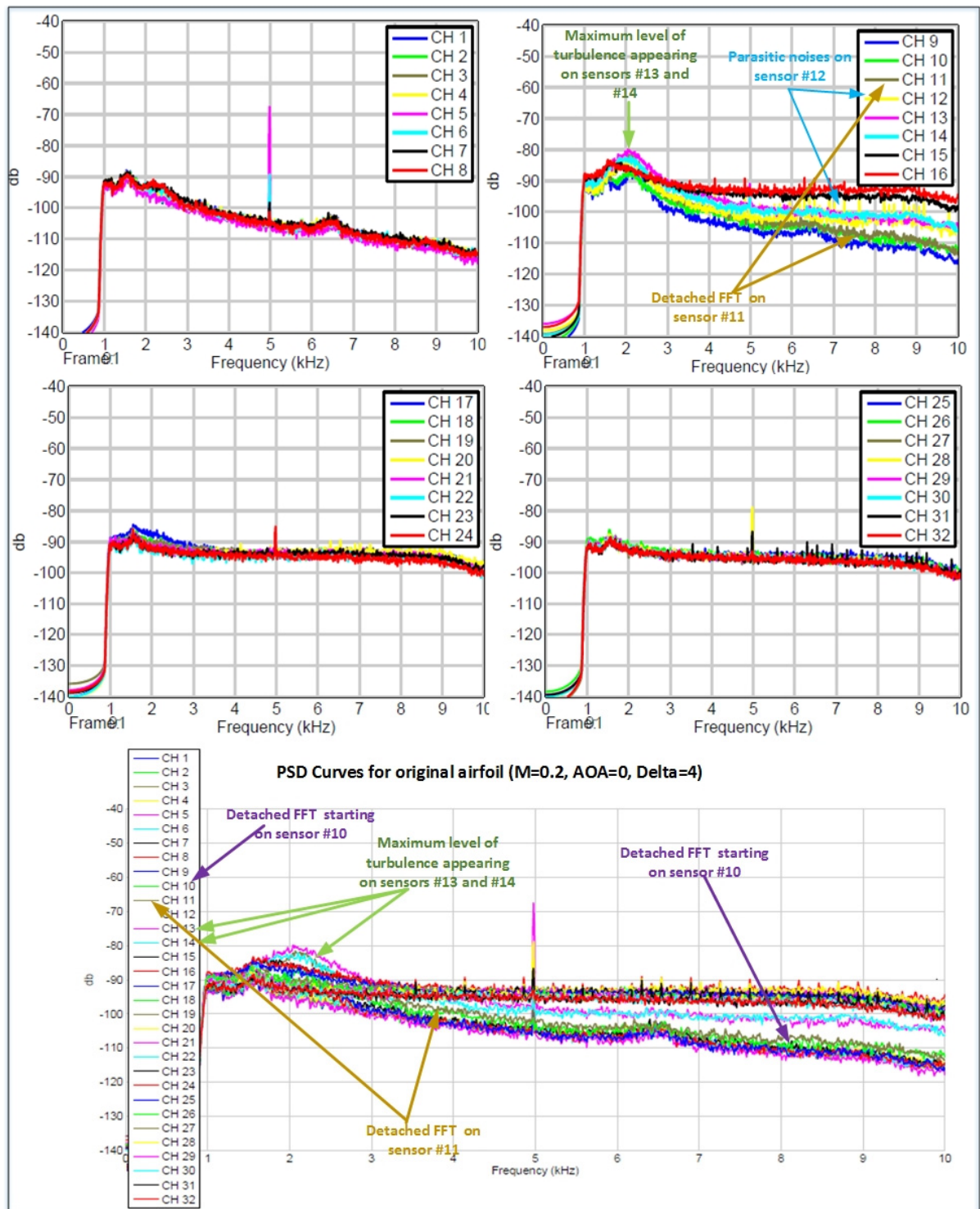


Figure 2.11 PSD representation of the original airfoil of case #68
(Mach number=0.2, $\alpha=0^\circ$, $\delta=4^\circ$)

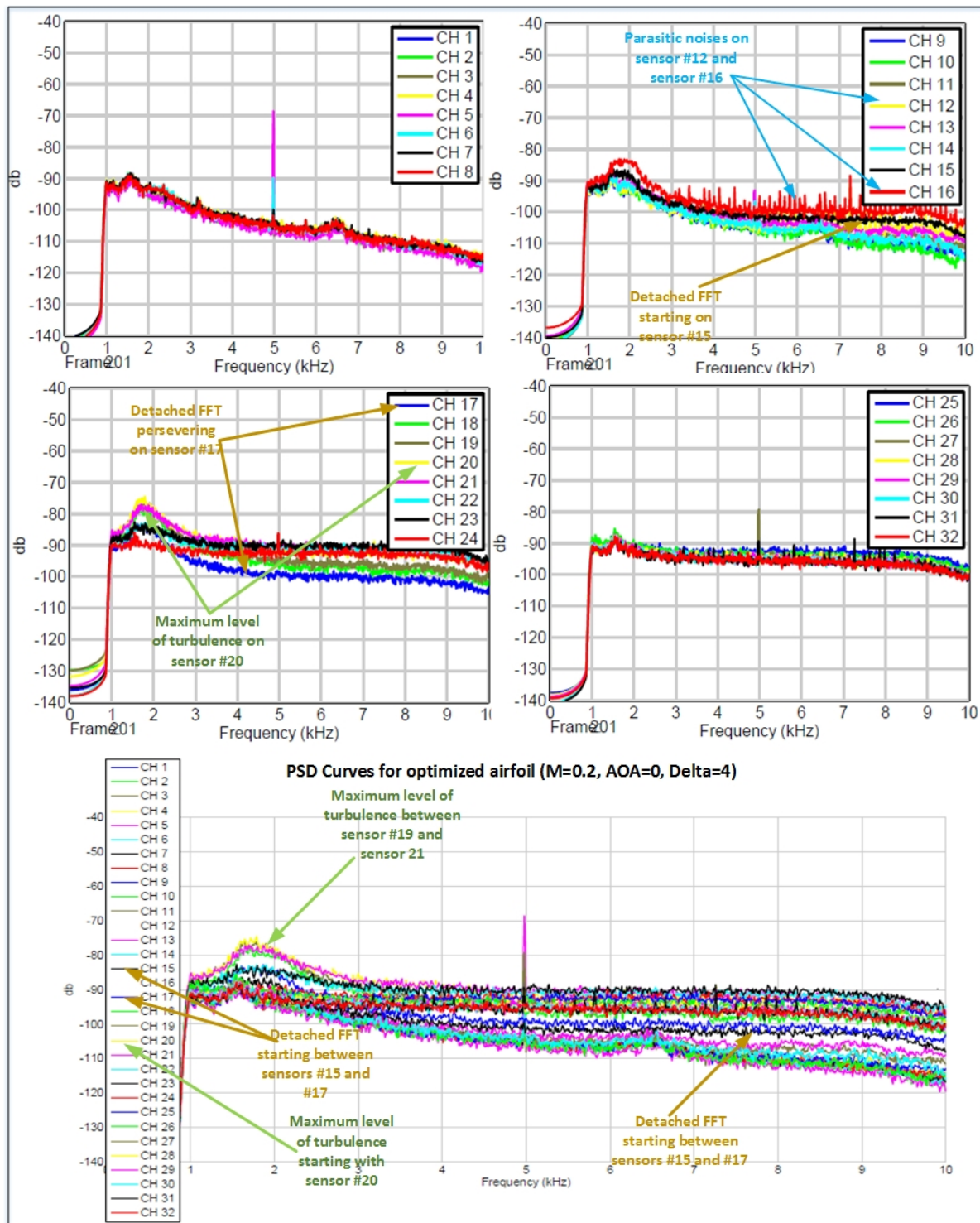


Figure 2.12 PSD representation of the optimized airfoil of case #68
(Mach number=0.2, $\alpha=0^\circ$, $\delta=4^\circ$)

For case #68, the post-processing of the Kulite pressure data has revealed that after the morphing procedure, the transition area moved from [42.45% , 45.16%] to [50.04% , 54.60%] of the chord, showing an average transition delay of 8.5% of the wing chord that was situated at 40% of the span. The post - processing details of other flight cases are shown in chapter 4 for additional illustrations of the procedure.

To validate the results obtained by using Kulite sensors, several measurements were performed using Infrared thermography camera visualization to capture the transition region on the entire wing model surface. IR thermography visualization allows the identification of the laminar-to-turbulent transition region based on the temperature gradient between the two flow regimes (section 1.4.3.3). The wing's leading edge and the upper surface flexible skin were coated with high emissivity black paint to obtain the highest possible IR photographs quality. The aileron flow behavior was then analyzed according to the IR measurements. The IR measurements and the photographs' post processing were conducted by NRC team member Youssef Mébarki. Figure 2.13 shows the IR measurements' visualization of the wing model for flight case #68 ($Mach=0.2$, $\alpha=0^\circ$, $\delta=4^\circ$).

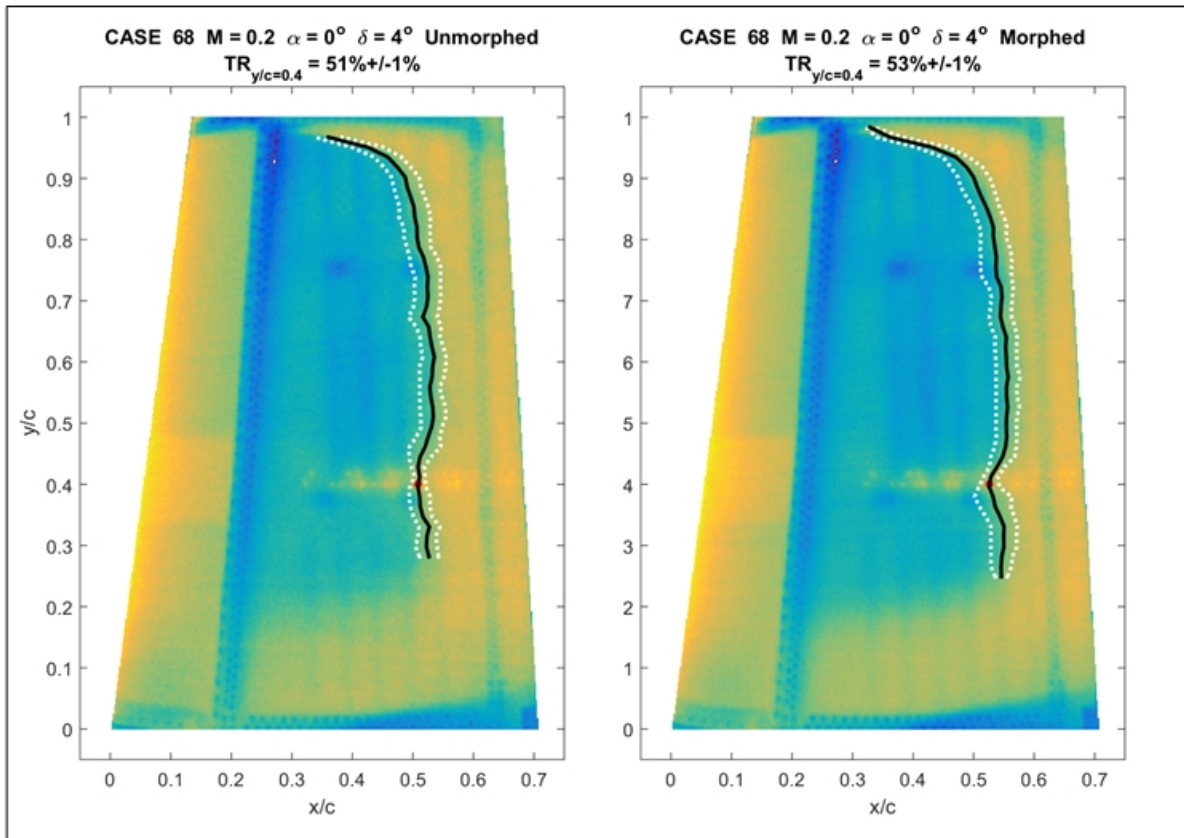


Figure 2.13 Infra-Red measurements for transition location on the wing upper surface for flight case #68, original airfoil (left) and optimized airfoil (right)

In the two images presented in Figure 2.13, the wind blows from the left to the right. The "blue" region indicates the low temperature area, representing the laminar zone, while the "yellow" region represents a warmer zone, indicating the turbulent area. The "black" line, which separates the two distinct zones, represents the average transition and its variation along the entire wing span. The two "white" dashed lines show the estimated extent of the transition area, which varies depending on the chord-wise gradient between the laminar and turbulent regimes. The two more horizontal "yellow" points' shapes situated between 30% and 70% of the chord lines, and at 40% of the wing span show the thermal signature of the Kulite sensors, and the "red" dot corresponds to the estimated average transition on the Kulite sensors line chord. For that Kulite sensors chord section, the IR results suggest that the transition moved from 51.01% to 53% of the chord, after the wing morphing. The NRC team member in charge of the IR measurement and post-processing estimated the accuracy of the

transition detection at $\pm 1\%$ of the local chord for both the morphed and the non morphed airfoils.

The successful transition delay obtained by IR measurements for the sensors' line, even though it was relatively less important in term of chord length than the Kulite sensors detection, could be seen occurring not only locally (as observed by Kulite sensors), but on a large percentage of the wing span. From the wind tunnel balance measurements, the maximum aerodynamic improvement gained from the transition delay for the flight case #68 is estimated as 0.15% of drag reduction, for a 0.37% gain in lift.

CHAPTER 3

VIBRATION DATA ACQUISITION SYSTEM AND REAL TIME PROCESSING

3.1 Context

During wind tunnel testing, flow fluctuations influenced the vibrations of the wing model, a phenomenon which could affect the overall wing performance and even jeopardize the safety of those working close to this wing model when the amplitudes become too high. In order to be able to observe the flutter vibrations, if indeed they occur despite the flutter analysis results, three accelerometers were installed on the wing box, on the aileron box and on the balance. The accelerometers' voltages were acquired in real time by using an NI acquisition system box that can handle their analog to digital conversion; the voltages were further processed in real time by the use of LABVIEW software for Fast Fourier Transform (FFT) visualization and amplitude vibration quantification, expressed in terms of accelerations.

This chapter is dedicated to a full description of the vibration acquisition system. The hardware equipment is fully described, as well as the software development using LABVIEW. The real time processing for amplitude vibration monitoring in terms of acceleration is also presented. The results are presented in chapter 4, along with their interpretation to confirm the absence of aeroelastic flutter during the wind tunnel tests as predicted by the flutter studies performed on the wing.

3.2 Data Acquisition System

3.2.1 Hardware Development

The wing model subjected to vibrations measurements was described in Section 2.2. An accelerometer sensor was installed in the wing box in order to quantify the wing vibrations and to prevent any flutter vibration that could occur in the wing. A second accelerometer was set inside the aileron box to assess the vibration stability of its actuation system, with respect

to the wing box. Finally, a third accelerometer was set on the wind tunnel balance to confirm its stability, as it was used as embedded support for the wing model during the wind tunnel tests. The wing and aileron accelerometers axes were disposed in such way that they coincided as much as possible with the wing (or aileron) vibration direction. The bending mode could occur along the Z axis, while the torsional mode and the lateral-bending mode were predicted to occur on the X and Y axes. Figure 3.1 presents the position of the accelerometers and their orientations on the wing.

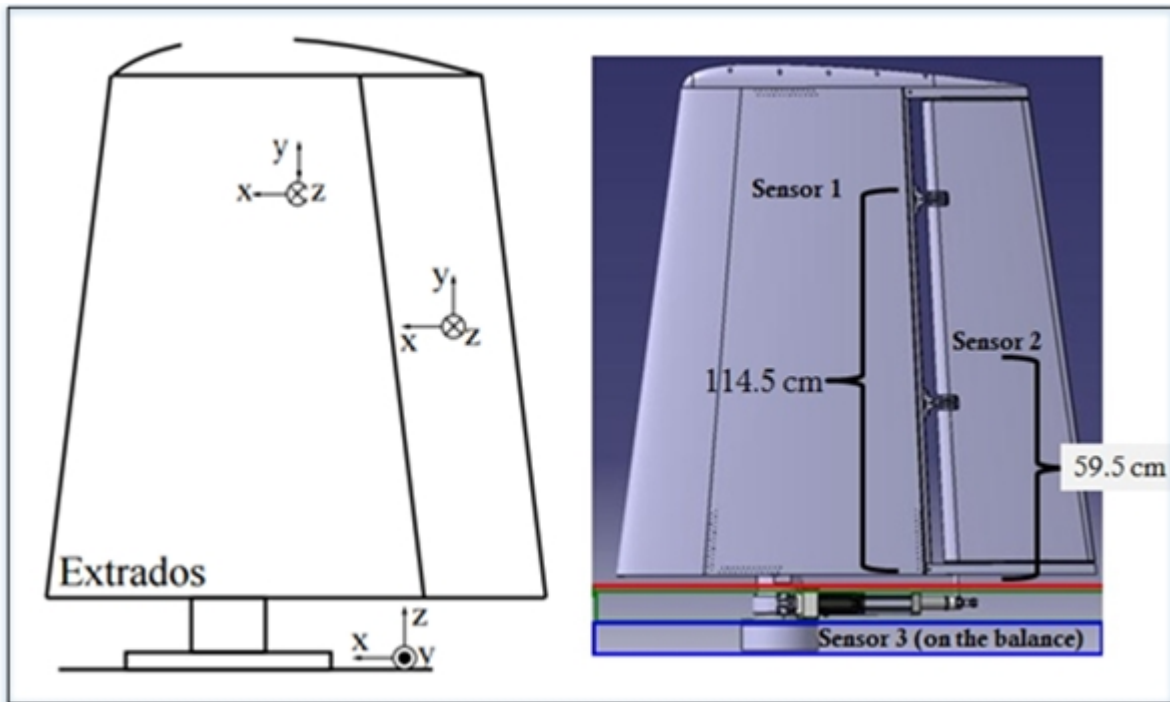


Figure 3.1 Accelerometers setup on the wing box, aileron box and balance

One of the key objectives of this research was to perform acceleration measurements on the wing and aileron boxes in terms of analog voltage signals, which could be processed in real time for vibration amplitude monitoring and for the graphical representation of accelerations in time and frequency domains.

The acquisition system was composed of three ADXL-326 type accelerometers (Annex II), an NI USB-6212 box, and an in-house software developed using NI's LabVIEW software

installed on a personal computer. The ADXL-326 is a small power, 3-axis accelerometer with signal- conditioned voltage outputs. It is able to sense the static acceleration of gravity in tilt-sensing applications, as well as the dynamic acceleration resulting from motions, shocks, or vibrations. Its functional block diagram is shown in Figure 3.2.

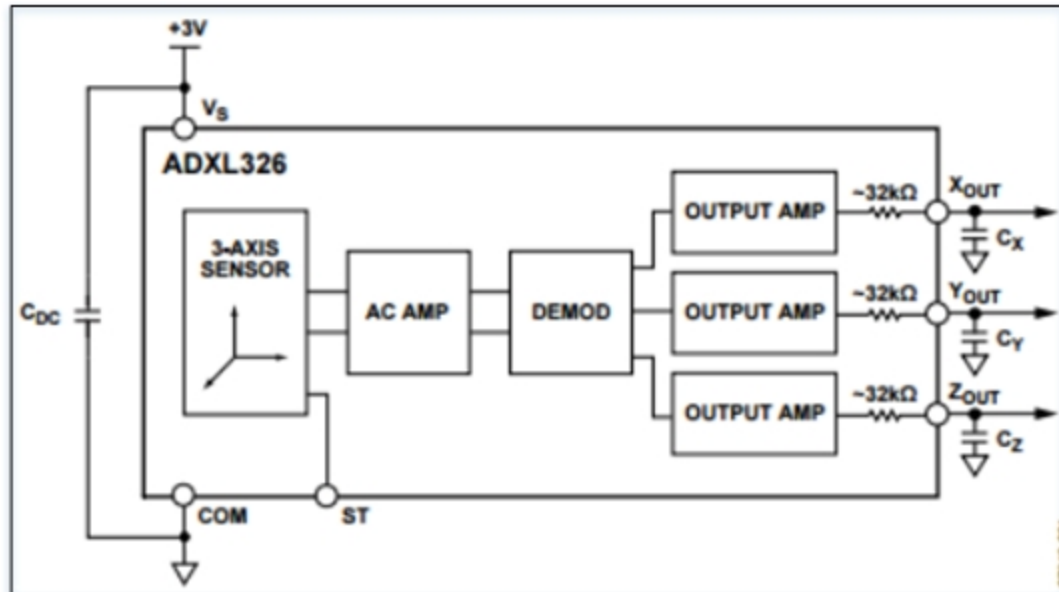


Figure 3.2 Functional block diagram of the ADXL-326 type accelerometer
Taken from Analog Devices (2009)

The accelerometers output analog signals from three different channels related to the instantaneous accelerations about X, Y and Z axes. On each axis, the acceleration is measured up to $\pm 16g$, with a zero g voltage of 1.5 V and an output sensitivity of 57 mV/g when the sensor is powered at 3 V. The ADXL326 is capable of performing frequency measurements in the bandwidth from 0.5 Hz to 1600 Hz (Annex II) for the accelerometers' X and Y axes, and from 0.5 Hz to 550 Hz (Annex II) for the accelerometers' Z axis. The complete sensor characteristics are given in Annex II.

For the real time acquisition, the accelerometers were connected to the NI USB-6212 box, which handled the Analog to Digital Conversion (ADC) of the acceleration outputs' voltage, for further digital processing and communication with the software installed on the personal computer. The NI USB-6212 has an ADC resolution of 16 bits and a sampling rate of up to

40,000 samples per second for the aggregate channels (Annex III), which is equivalent to a maximum sampling rate of 4,444 samples per second for each of the nine axes of all three accelerometers. This sampling rate value was high enough for the purpose of vibration measurements, since from the Nyquist-Shannon sampling theorem (Bellanger *et al.*, 2013) and the accelerometers' specifications (Annex II), the minimum sampling rate required for a suitable acceleration acquisition is approximately 3,200 Hz for the X and Y axes, and 1,110 Hz for the Z axis. The voltage measurements on the three accelerometers were made with respect to a common ground (Ground Reference Voltage Measurement), provided by the NI USB-6212 box.

The NI USB-6212 box finally communicated with the personal computer software by means of a USB port. Its specifications are listed in Annex III. Figure 3.3 presents the vibration data acquisition system and the connections between its various components.

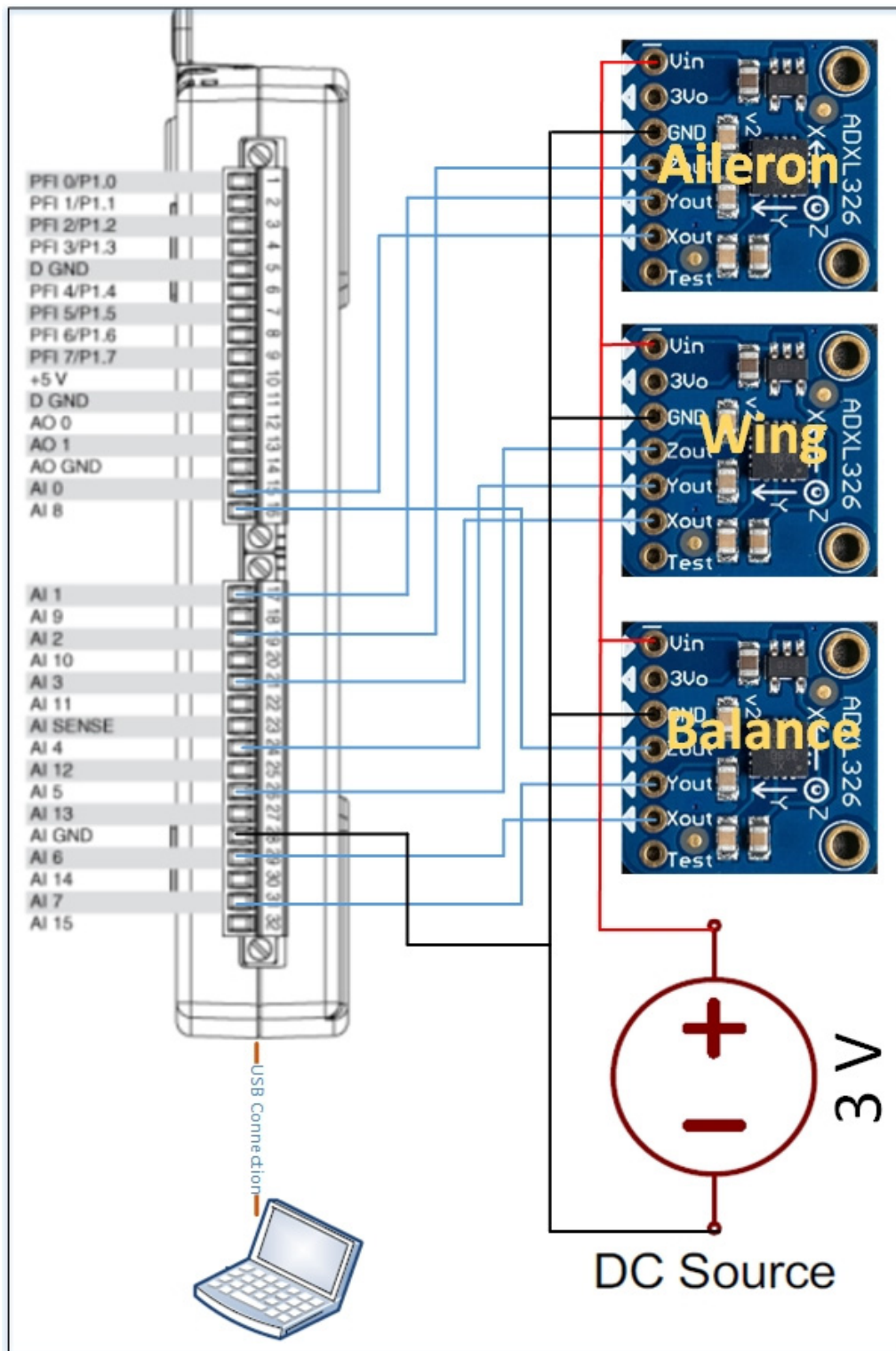


Figure 3.3 Architecture of the vibration data acquisition system

3.2.2 Software Development

3.2.2.1 Real Time Data Acquisition

The software development for the vibration data acquisition system was realized by using the LabVIEW programming language. This software should be able to acquire acceleration values in real-time, graphically visualize them in both the time-domain and the frequency-domain, and record the data for further post processing.

Two main parameters must be considered for a suitable real time data acquisition from sensors. The first parameter is the "*sampling rate*". It largely depends on the frequency bandwidth of the sensor and should be equal to at least two times the highest frequency of the sensor bandwidth, according to the Nyquist-Shannon sampling theorem (Bellanger *et al.*, 2013), as shown by equation 3.1:

$$f_s \geq 2 * BW_{max} \quad (3.1)$$

where f_s is the sampling rate and BW_{max} is the highest value of the frequency bandwidth. Since the highest value of the ADXL 326's frequency bandwidth is 1,600 Hz for the X and Y axes and 550 Hz for the Z axis (Annex II), the sampling rate was set to 3,200 samples per second to satisfy the Nyquist-Shannon sampling theorem for all the axes. The chosen sampling rate also satisfied the requirements of the NI USB-6212 box, which allows a sampling rate of up to 4,444 samples per second for each channel (Annex III).

The second parameter is the number of samples that should be considered for the time domain visualization of accelerations and their real time Fast Fourier Transform (FFT) computation. The value of the number of samples ' N ' always determines the acquisition time, which is the time it takes to acquire one of the numerous frames (of N data samples) that are successively processed in real time. The acquisition time T is given by equation 3.2

$$T = \frac{N}{f_s} \quad (3.2)$$

spectrum visualization through the FFT algorithm. When the airflow was in its steady state, the data savings was powered on to record accelerations. For the vibration amplitude monitoring, the maximum amplitude for each accelerometer was computed and compared to the threshold $0.5\ g$. The threshold was deduced from aeroelastic predictions (Koreanschi *et al.*, 2016). The alarm was automatically powered on if any accelerometer maximum amplitude exceeded the threshold.

The maximum amplitude computation was computed as shown in section 3.2.2.2. An additional buffer was created to prevent the software from crashing when the main buffer was full. In fact, the time required for the data processing sometimes appeared to be higher than the acquisition time, thereby causing a rapid filling of the main buffer, which had limited capacity. In that case, an additional buffer supplemented the main buffer with more space until the main buffer emptied out. Figure 3.5 and Figure 3.6 show screen shots of the software interface, where we can see the accelerations displayed in the time domain and distinguish the switch that activates the data recording (Figure 3.5). In Figure 3.6, we can see the positions of the alarms' thresholds and the alarms lights on the software interface. The instantaneous processing time and the number of data frames saved on the additional buffer ("*element in queue*" in Figure 3.6) are also indicated.

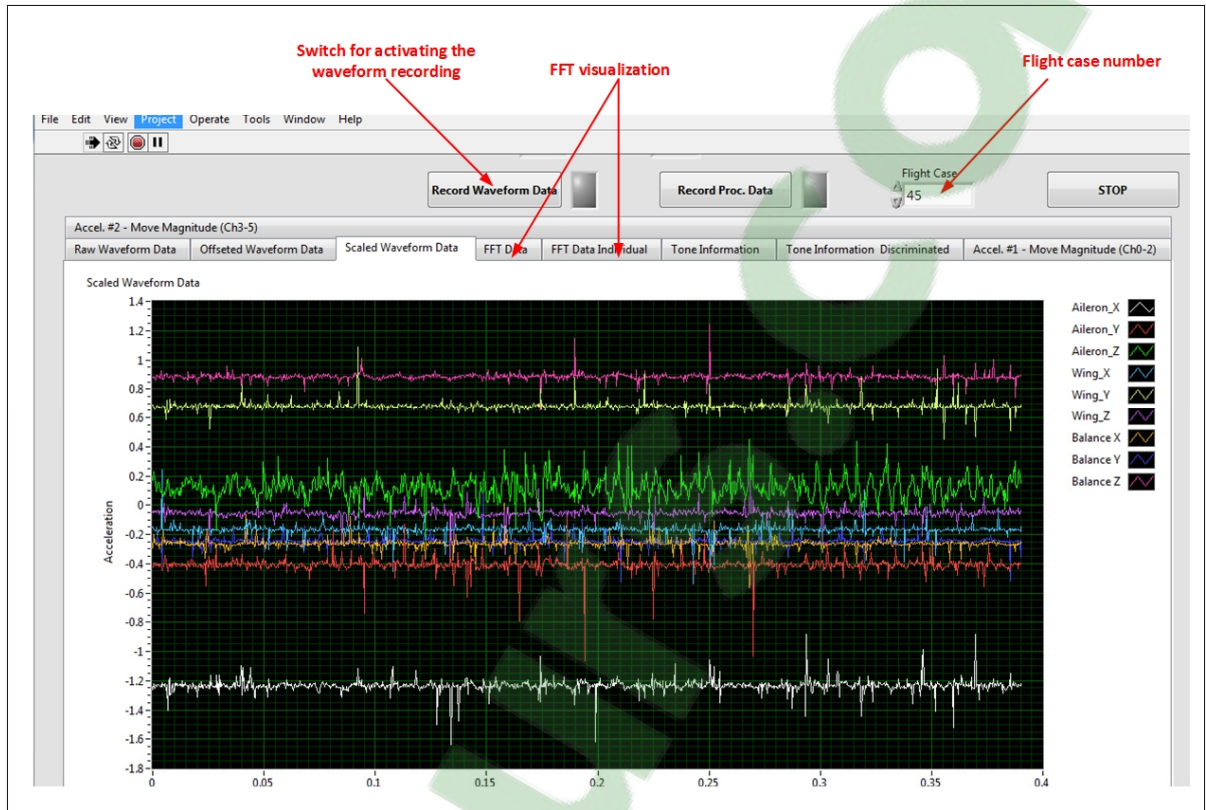


Figure 3.5 Screen shot of the software interface (1)

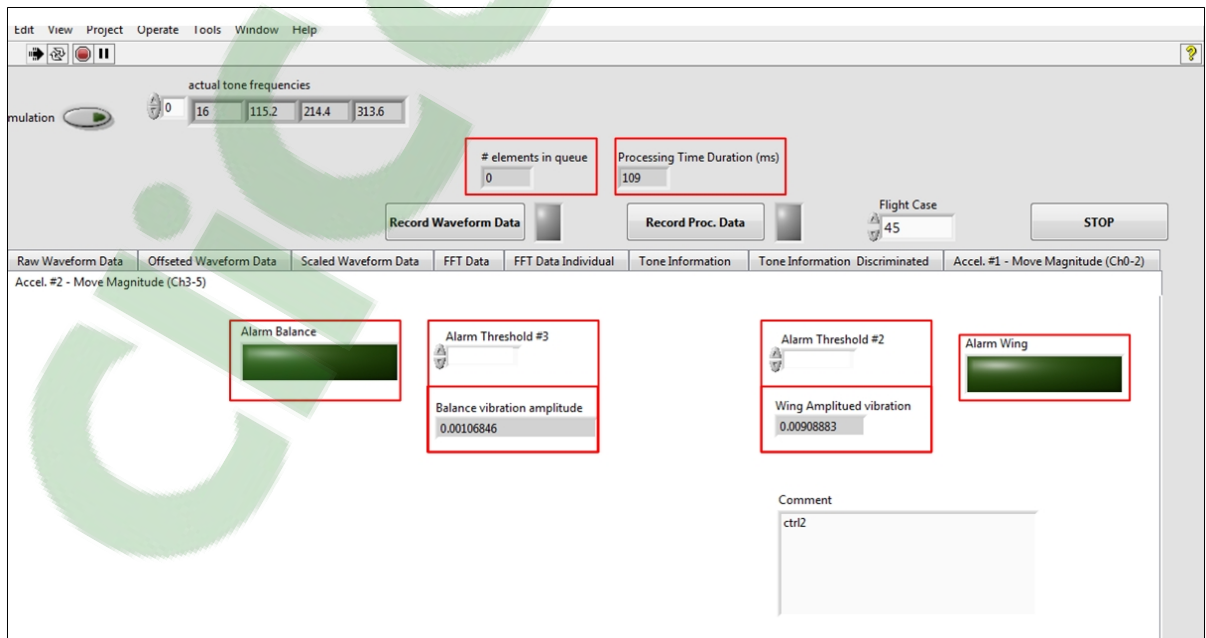


Figure 3.6 Screen shot of the software interface (2)

3.2.2.2 Real Time Processing: Acceleration Amplitude Monitoring

The maximum amplitude computation formula represents the key to vibration amplitude monitoring. We first had to quantify the magnitude of the acceleration provided by the wing and the aileron. A good method would have been to quantitatively relate the time domain amplitudes with the spectral amplitudes in the frequency domain by the means of energy methods such as the PARSEVAL theorem (Bellanger et al., 2013). This approach would have had the benefit of evaluating the signal strength of every single frequency band and we would therefore have been able to erase any undesirable contribution caused by parasitic noises from the vibration amplitude computation. The greatest barrier to implementing this method is being able to consider the windowing effect. Windowing methods are generally used to reduce the disruptions occurring during FFT computation due to uncentered frequency components (Thomas C, 2000). While windowing methods are essential for spectral visualization applications, they do cause reductions of the actual frequency amplitudes that should be considered for vibration amplitude computations. Generally, the windowing reduction coefficient depends on the type of windowing method used, and is not precisely explained in the literature for each windowing method. In addition, an incorrect evaluation of this coefficient could cause under-estimation of the time domain amplitudes (in terms of frequency domain amplitudes), which could jeopardize the vibration monitoring.

After evaluating the issues surrounding the windowing effect, we chose a method based on the Standard Deviation (SD) of the accelerations for calculating the maximum vibration amplitude. The calculated maximum amplitude may indeed include undesirable contributions from parasitic noises and contributions from actual wing acceleration changes that could result in overestimating the actual vibration amplitude. However, this overestimation did not affect the vibration monitoring; on the contrary, it represented a safety margin between the actual value of the vibration amplitude and its value displayed on the screen, which was finally considered as the value for the alarm signal.

The following demonstration is shown for the wing acceleration readings, and is also valid for the aileron accelerometer readings. To compute the maximum amplitudes of the recorded accelerations, we supposed that the recorded waveforms were composed of sums of sinusoid signals representing the vibration modes accelerations as shown in equation 3.2,

$$A(t) = \sum_i A_{X_i} \sin(2\pi f_{X_i} t + \phi_{X_i}) \vec{i} + \sum_i A_{Y_i} \sin(2\pi f_{Y_i} t + \phi_{Y_i}) \vec{j} + \sum_i A_{Z_i} \sin(2\pi f_{Z_i} t + \phi_{Z_i}) \vec{k} \quad (3.3)$$

With $f_{X_i} \neq f_{Y_i} \neq f_{Z_i}$, where $A_{X_i}, A_{Y_i}, A_{Z_i}$ represent the acceleration amplitudes of the torsional mode (on the X-axis), lateral-bending mode (on the Y-axis), and the bending mode (the Z-axis), respectively, $f_{X_i}, f_{Y_i}, f_{Z_i}$ are the corresponding frequencies, and $\phi_{X_i}, \phi_{Y_i}, \phi_{Z_i}$ are the corresponding phases (Lalanne, 2013).

The demonstrations below only concern the Z-axis accelerometer readings, but they remain valid for the X and Y axes. The aim is to find a single value corresponding to the boundary of the recorded Z-axis accelerations.

By considering two sinusoids such that the bending acceleration is equal to the sum of those two sinusoids, we can write:

$$\begin{aligned} A_Z(t) &= A_Z \sin(2\pi f_Z t + \phi_Z) \\ &= A_{Z_1} \sin(2\pi f_{Z_1} t + \phi_{Z_1}) + A_{Z_2} \sin(2\pi f_{Z_2} t + \phi_{Z_2}) \end{aligned} \quad (3.4)$$

The standard deviation values computed from the two sinusoids verify equation 3.5 (Mathematics, 2014)

$$(SD_{Z_1+Z_2})^2 = SD_{Z_1}^2 + SD_{Z_2}^2 \quad (3.5)$$

where

- $SD_{Z_1+Z_2}$ is the standard deviation of A_Z ,
- SD_{Z_1} is the standard deviation of the first sinusoid, and $SD_{Z_1} = \frac{A_{Z_1}}{\sqrt{2}}$,
- SD_{Z_2} is the standard deviation of the second sinusoid, and $SD_{Z_2} = \frac{A_{Z_2}}{\sqrt{2}}$.

Equation 3.5 leads to:

$$(SD_{Z_1+Z_2})^2 = \frac{A_{Z_1}^2 + A_{Z_2}^2}{2} \quad (3.6)$$

Equation 3.6 can be written as:

$$4 (SD_{Z_1+Z_2})^2 = 2 (A_{Z_1}^2 + A_{Z_2}^2) \quad (3.7)$$

Equation 3.8 to equation 3.11 show that $2 (A_{Z_1}^2 + A_{Z_2}^2)$ is always higher than $(A_{Z_1} + A_{Z_2})^2$ for any real numbers A_{Z_1} and A_{Z_2} .

Start with:

$$(A_{Z_1} - A_{Z_2})^2 \geq 0 \quad (3.8)$$

and then square equation 3.8 to yield

$$A_{Z_1}^2 + A_{Z_2}^2 - 2A_{Z_1}A_{Z_2} \geq 0 \quad (3.9)$$

which is equivalent to:

$$A_{Z_1}^2 + A_{Z_2}^2 \geq 2A_{Z_1}A_{Z_2} \quad (3.10)$$

Adding the positive number $A_{Z_1}^2 + A_{Z_2}^2$ on both side of the inequality, equation 3.10 leads to equation 3.11

$$2 (A_{Z_1}^2 + A_{Z_2}^2) \geq 2A_{Z_1}A_{Z_2} + A_{Z_1}^2 + A_{Z_2}^2 \quad (3.11)$$

which is equivalent to:

$$2 (A_{Z_1}^2 + A_{Z_2}^2) \geq (A_{Z_1} + A_{Z_2})^2 \quad (3.12)$$

By replacing equation 3.7 in equation 3.12, equation 3.13 is obtained

$$4 (SD_{Z_1+Z_2})^2 \geq (A_{Z_1} + A_{Z_2})^2 \quad (3.13)$$

$$2 * SD_{Z_1+Z_2} \geq A_{Z_1} + A_{Z_2} \quad (3.14)$$

$$\begin{aligned} &\geq |A_{Z_1} \sin(2\pi f_{Z_1} t + \phi_{Z_1}) + A_{Z_2} \sin(2\pi f_{Z_2} t + \phi_{Z_2})| \\ &|A_{Z_1} \sin(2\pi f_{Z_1} t + \phi_{Z_1}) + A_{Z_2} \sin(2\pi f_{Z_2} t + \phi_{Z_2})| \leq 2 * SD_{Z_1+Z_2} \end{aligned} \quad (3.15)$$

Equation 3.15 has been demonstrated for two sinusoids, but this inequality can be extended for n sinusoids (n is a natural number) following mathematical induction. It can be rewritten in the following form:

$$\left| \sum_{i=1}^n A_{Z_i} \sin(2\pi f_{Z_i} t + \phi_{Z_i}) \right| \leq 2 * SD_{Z_1+\dots+Z_n} \quad (3.16)$$

Equation 3.16 is valid for the accelerometers' reading on the Z-axis. The accelerometers' readings on the X and Y axes are indicated in equation 3.17 and equation 3.18.

$$\left| \sum_{i=1}^n A_{X_i} \sin(2\pi f_{X_i} t + \phi_{X_i}) \right| \leq 2 * SD_{X_1+\dots+X_n} \quad (3.17)$$

$$\left| \sum_{i=1}^n A_{Y_i} \sin(2\pi f_{Y_i} t + \phi_{Y_i}) \right| \leq 2 * SD_{Y_1+\dots+Y_n} \quad (3.18)$$

The whole wing motion is verified with equation 3.19

$$\begin{aligned}
& \sqrt{\left(\sum_{i=1}^n A_{X_i} \sin(2\pi f_{X_i} t + \phi_{X_i})\right)^2 + \left(\sum_{i=1}^n A_{Y_i} \sin(2\pi f_{Y_i} t + \phi_{Y_i})\right)^2} \\
& \quad + \left(\sum_{i=1}^n A_{Z_i} \sin(2\pi f_{Z_i} t + \phi_{Z_i})\right)^2 \\
& \leq 2\sqrt{(SD_{X_1+\dots+X_n})^2 + (SD_{Y_1+\dots+Y_n})^2 + (SD_{Z_1+\dots+Z_n})^2}
\end{aligned} \tag{3.19}$$

The maximum amplitude accelerations were computed following equation 3.19 for every frame of 1,600 data points recorded during the real time processing, and these were then used for vibration monitoring. The maximum vibration amplitudes are displayed in terms of accelerations in the fourth (next) chapter for the Mach numbers of 0.15 and 0.25 that were considered during the subsonic wind tunnel tests at IAR-NRC.

CHAPTER 4

WIND TUNNEL TESTS AND RESULTS

4.1 Wind Tunnel Test Procedure

This chapter is dedicated to the description of the wind tunnel tests and the data post processing results. The NRC wind tunnel facilities and characteristics are described, as well as the test preparations. Those descriptions are followed by interpretations of the aerodynamic pressure experimental data, and their comparison with numerical predictions. Finally, vibration measurements are also displayed in order to demonstrate the absence of aeroelastic phenomena at speeds $M = 0.15$, $M = 0.2$ and $M = 0.25$ during the wind tunnel tests.

4.1.1 NRC Wind Tunnel Description

Wind tunnels are usually designed for a specific technical purpose and a precise speed range. There are several different ways to classify them. Depending on their circuit shapes, wind tunnels are basically distinguished into two different types (open and closed). An open return circuit tunnel is characterized by its two open sides, and has the particularity of gathering the air using an engine in the room where the tunnel is located in order to supply air to the test section. This type of wind tunnel has the advantages of a lower construction cost and a suitable design for propulsion and smoke visualization, since it does not allow the accumulation of exhaust products inside its circuit. However, the simplicity of this type of wind tunnel construction design comes at the expense of the flow quality in the test section. In addition, it incurs higher operating costs, as the fan must continuously maintain the accelerated flow during these tests.

In a closed wind tunnel, the air is conducted from the exit of the fan to the contraction section by a series of ducts and turning vanes. This type of wind tunnel was used in the CRIAQ

MDO-505 project in the M2 building of the NRC Institute for Aerospace Research (IAR-NRC) in Ottawa. Due to its shape (represented in Figure 4.1), the closed return tunnel allows the continuous circulation of the air through its various sections.

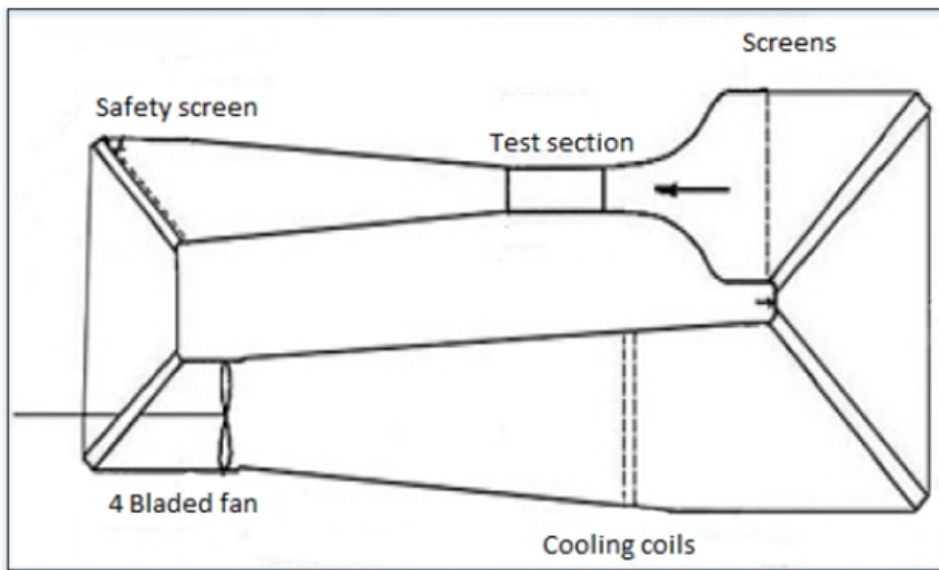


Figure 4.1 Simplified scheme of the wind tunnel at the NRC (closed return)
Taken from (Guezguez, 2015)

Closed return tunnels do offer a higher quality flow in test section than that available to an open wind tunnel, but their construction costs are higher (compared to those of open wind tunnels) due to their more complex design. However, the operating costs for this type of wind tunnel remain relatively low. The NRC wind tunnel is classified as subsonic, with a maximum Mach number of 0.3. The test section is equipped with a six-axis aerodynamic balance for measuring both forces and moments acting on the model during the tests. Table 4.1 shows the specifications of the NRC subsonic wind tunnel.

Table 4.1 NRC Wind Tunnel Technical Specifications
Adapted from IAR-National Research Council of Canada (2013)

Tunnel geometry	Test section: 1.9 m *2.7 m *5.2 m
	Test section area: 5.07 m ²
Tunnel characteristics	Fan power: 1.5 MW
	Maximum speed: 140 m/s
	Turbulence level: 0.14%
	Speed uniformity: ± 0.7
Main balance	Measurement accuracy: $\pm 0.1\%$ to $\pm 0.05\%$ full scale
	Maximum model weight: 450 kg
	Lift, drag, side force (kN): $\pm 6.7, \pm 2.3, \pm 4.4$
	Pitch, roll, yaw (kN.m) $\pm 2.7, \pm 2.7, \pm 2.7$

4.1.2 Wind Tunnel Test Preparation and Progress

The morphing wing with a rigid aileron was wind tunnel tested during two different test periods. The first took place in April 2015, and the second in June 2015. Before a wind tunnel test can take place, a significant amount of preparations are necessary to ensure a proper conduct of the operations. These tests were conducted by the NRC team, in collaboration with the LARCASE team. The NRC team installed the morphing wing model inside the test chamber, in collaboration with the LARCASE team. The wing was set and fixed on the turntable so that the wing chord remained perfectly aligned to the flow direction. The obtained position therefore matched the zero angle of rotation on the turntable, thus making the wing angle of attack proportional to the turntable angle.



Figure 4.2 CRIAQ MDO 505 project wing model setup
in the NRC wind tunnel section

After installing the mechanical structure as shown in Figure 4.2, all the additional materials were installed and connected to the wing. These additional materials included equipment for aileron and actuation controls, for pressure sensing and their data acquisition, and finally equipment for vibration sensing and data logging. Figure 4.3 presents a plan of the NRC wind tunnel wing model and its associated hardware equipment installation.

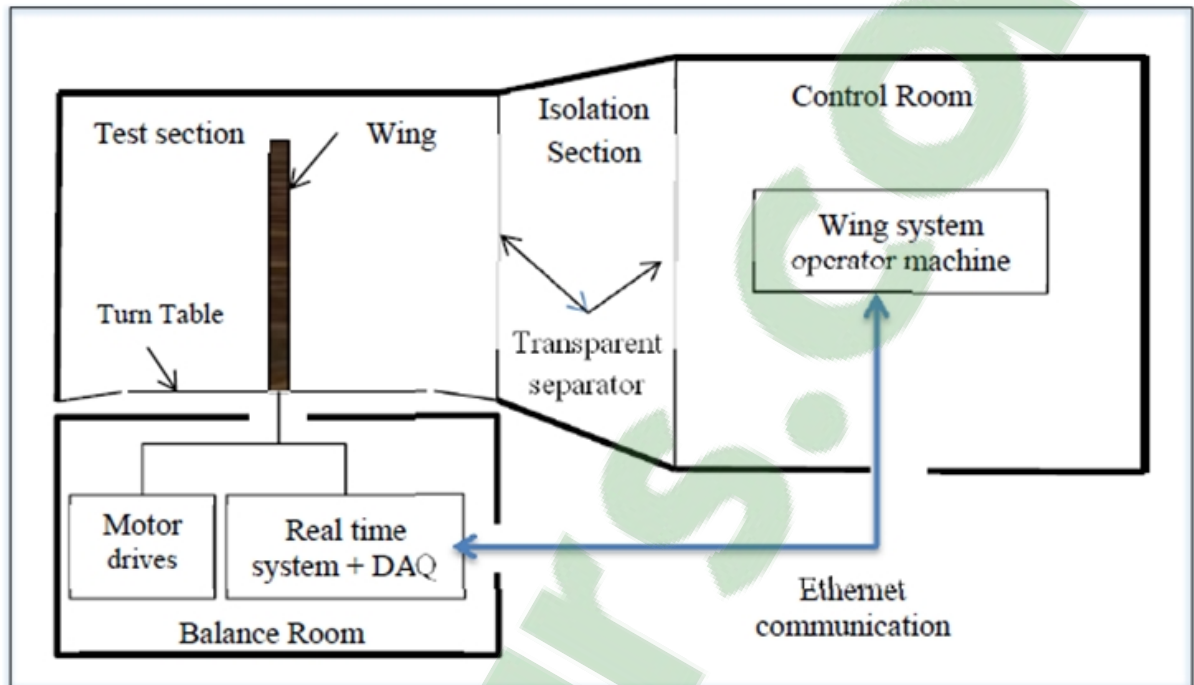


Figure 4.3 NRC subsonic wind tunnel facilities plan

Most of the hardware equipment (motor drives, real time systems) were located in the balance room and were used to link the model (in the test section) to the operator machines in the control room. This hardware setup allowed the model to be fully controlled from the control room.

The successful progress of the wind tunnel tests was the result of the active participation and collaboration of the two teams. The procedure was written and proposed by the NRC team; it was then accepted and adopted by the LARCASE team and all the other partners. The control of the wing actuators, the aileron deflections, and the pressure and acceleration data logging were operated from the control room by the LARCASE team. The NRC team members were in charge of controlling the wind tunnel speed and the wing angle of attack. The control room was separated from the test section by an isolator section, which ensured the security of the people involved in the tests.

After the hardware setup, the NRC team had to check and confirm the efficiency and readiness of their wind tunnel control and data acquisition systems. For their part, the LARCASE team inspected the connections and the proper functioning of the actuators and the aileron controllers, the vibration data acquisition system and the pressure data logging system. Finally, both teams ensure the efficient coexistence of all the control and acquisition systems.

Before starting the first test run, some additional verifications were performed on the wind tunnel:

- A smoke test; in which the wing model airflow was visualized in real time in order to determine the exact location of the wake rake;
- A turntable test, to ensure the proper rotation of the turntable in both directions; and
- Balance load limit verification: The balance measures the aerodynamic loads (forces and moments) created by the wing airflow. Balance load limit verification ensures that the amplitudes of the loads created by the most extreme test conditions will remain lower than the sensor amplitudes' limits.

4.2 Overview of Aerodynamics Results

Interpretations of the wind tunnel data processing figures are displayed below. Figure 4.4 to Figure 4.9 show the standard deviation plots related to flight case #40 to flight case #45.

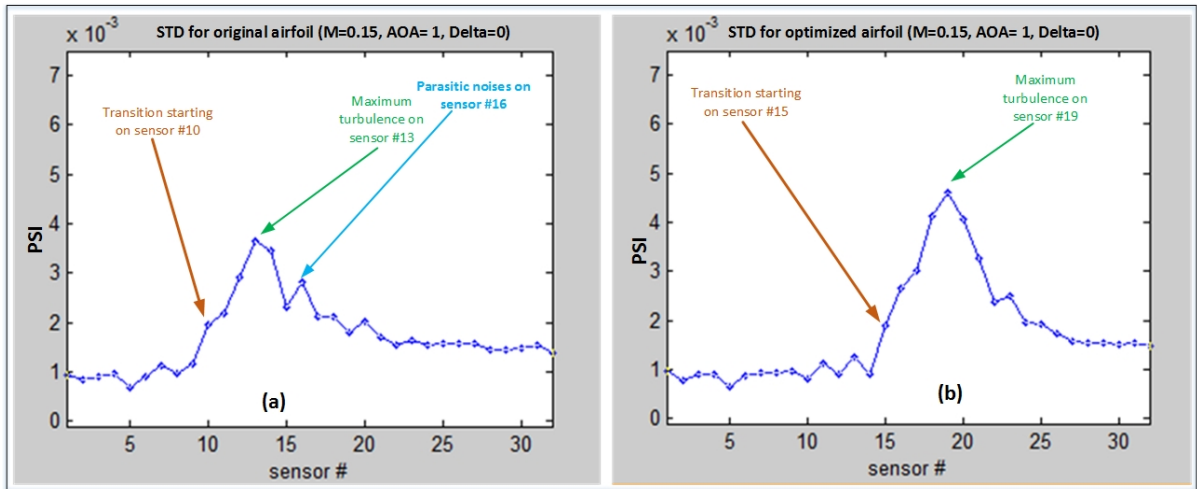


Figure 4.4 Standard deviation of pressure data acquired for flight case #40, for the original (a) and the optimized airfoil (b)

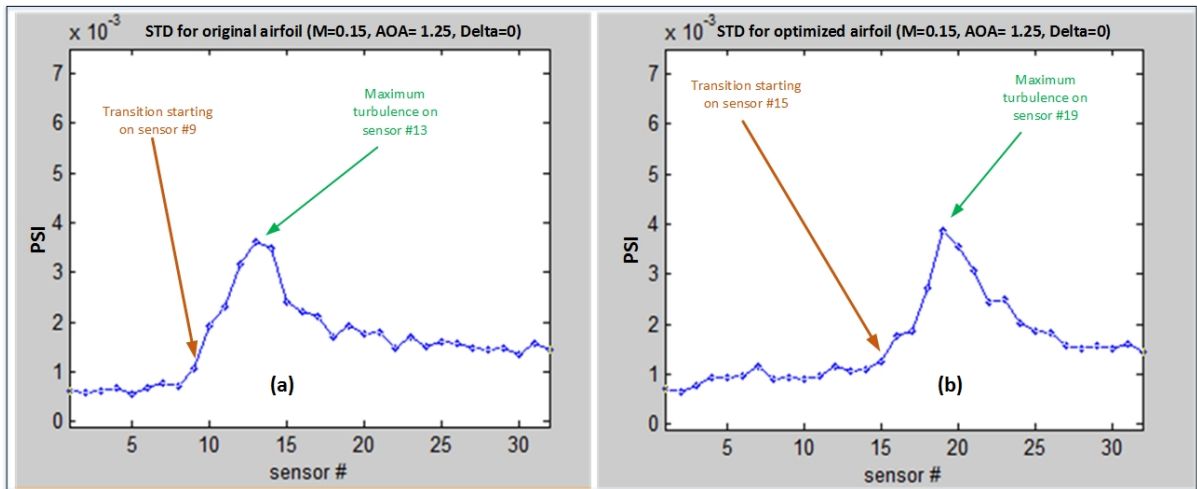


Figure 4.5 Standard deviation of pressure data acquired for flight case #41, for the original (a) and the optimized airfoil (b)

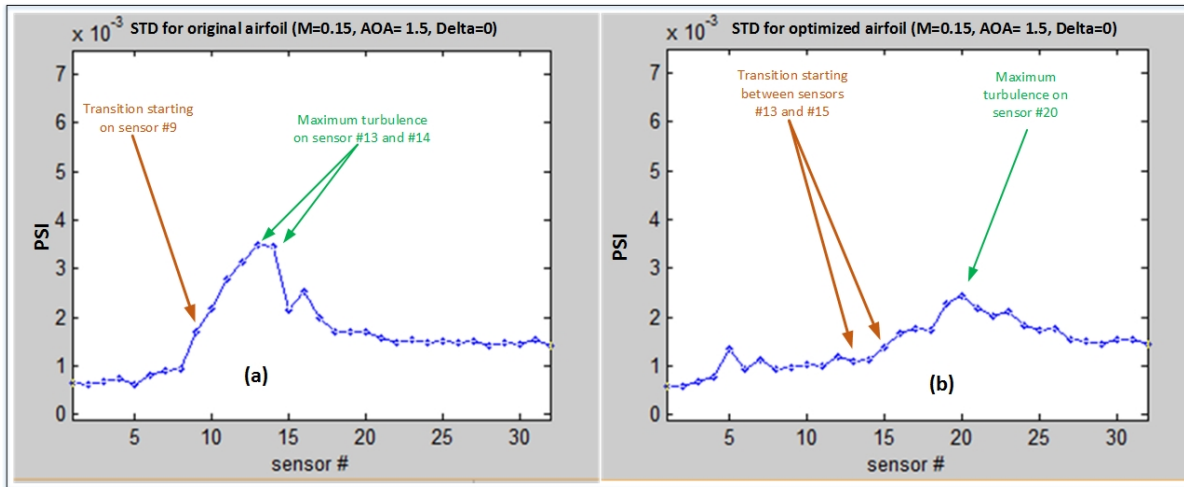


Figure 4.6 Standard deviation of pressure data acquired for flight case #42, for the original (a) and the optimized airfoil (b)

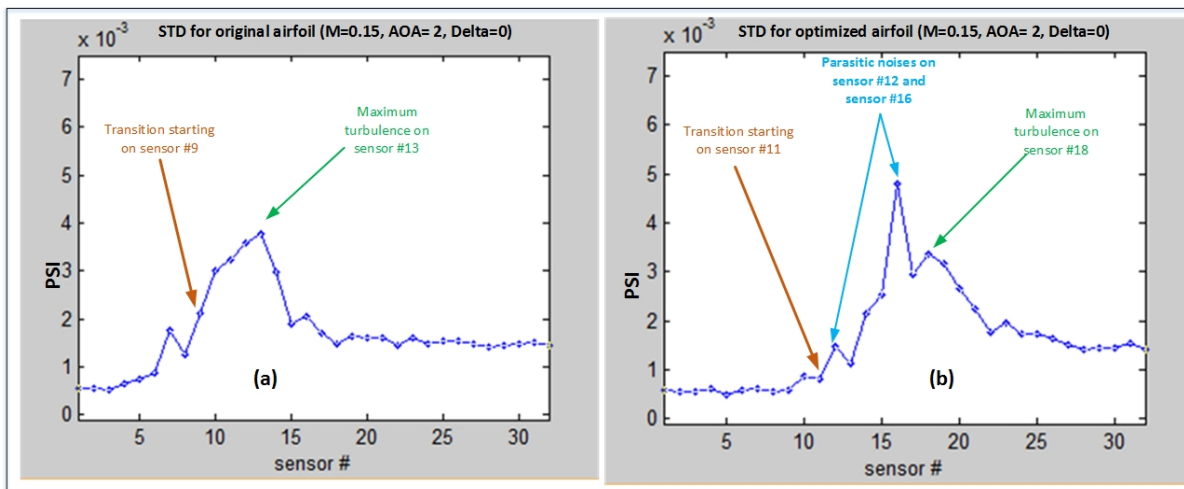


Figure 4.7 Standard deviation of pressure data acquired for flight case #43, for the original (a) and the optimized airfoil (b)

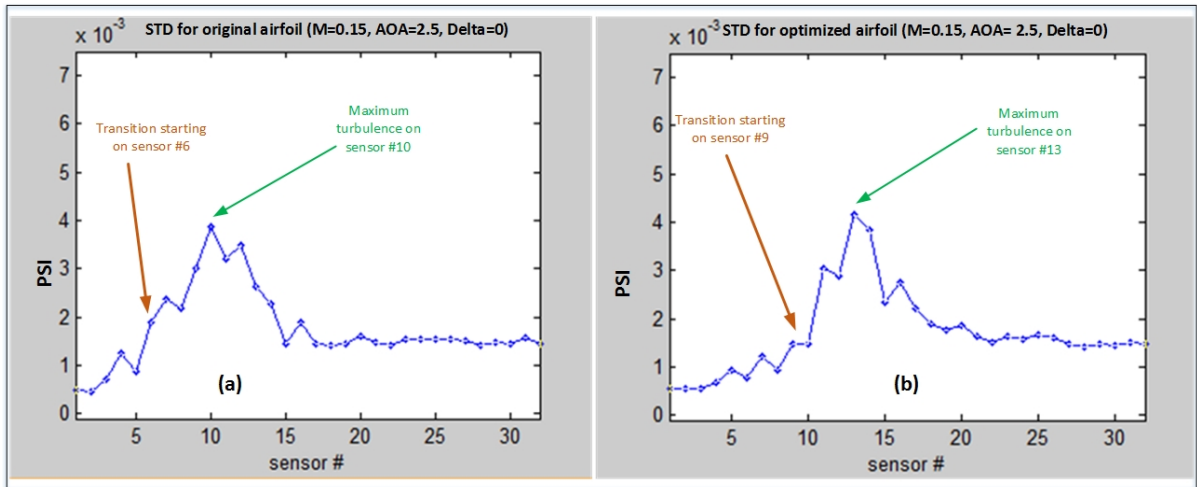


Figure 4.8 Standard deviation of pressure data acquired for flight case #44, for the original (a) and the optimized airfoil (b)

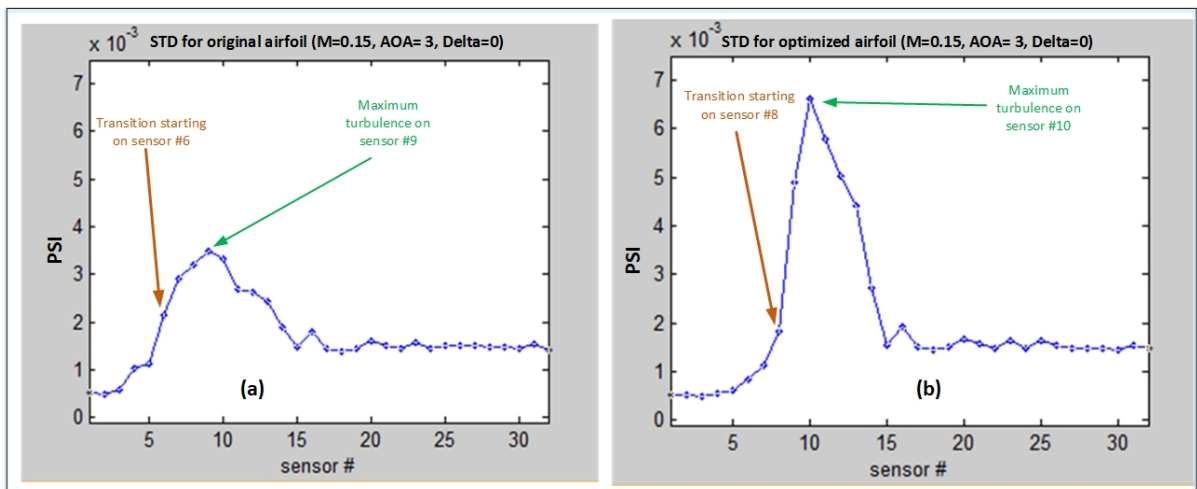


Figure 4.9 Standard deviation of pressure data acquired for flight case #45, for the original (a) and the optimized airfoil (b)

Figure 4.10 to Figure 4.21 illustrate the Power Spectrum Density (PSD) plot interpretations for flight case #40 to flight case #45. Figure 4.10 to Figure 4.15 are dedicated to the original airfoils' PSD's and Figure 4.16 to Figure 4.21 show the optimized airfoils' PSD's. The sensor's numbers are denoted by "CH".

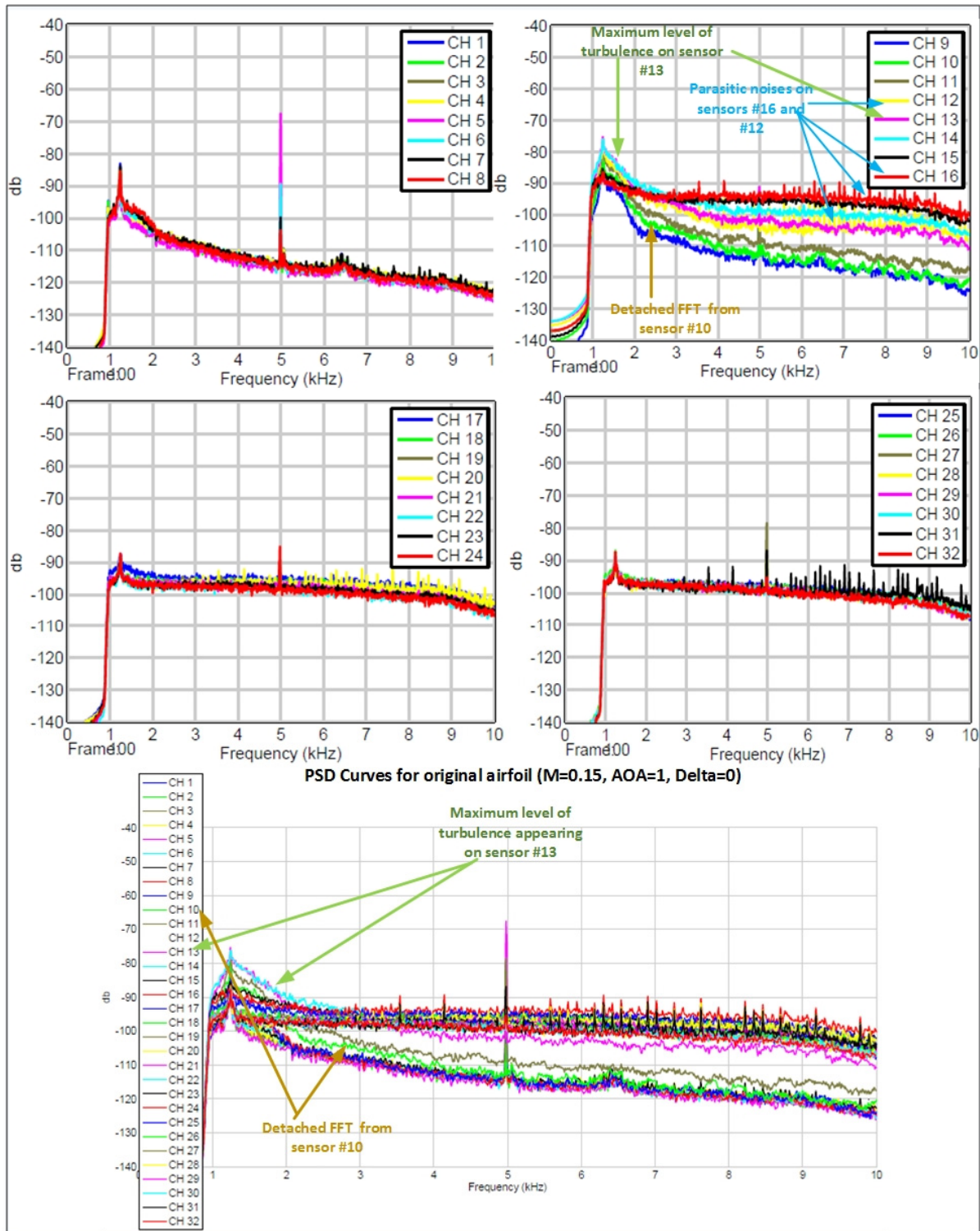


Figure 4.10 PSD representation for the original airfoil, case #40 (Mach=0.15, $\alpha=1^\circ$, $\delta=0^\circ$)

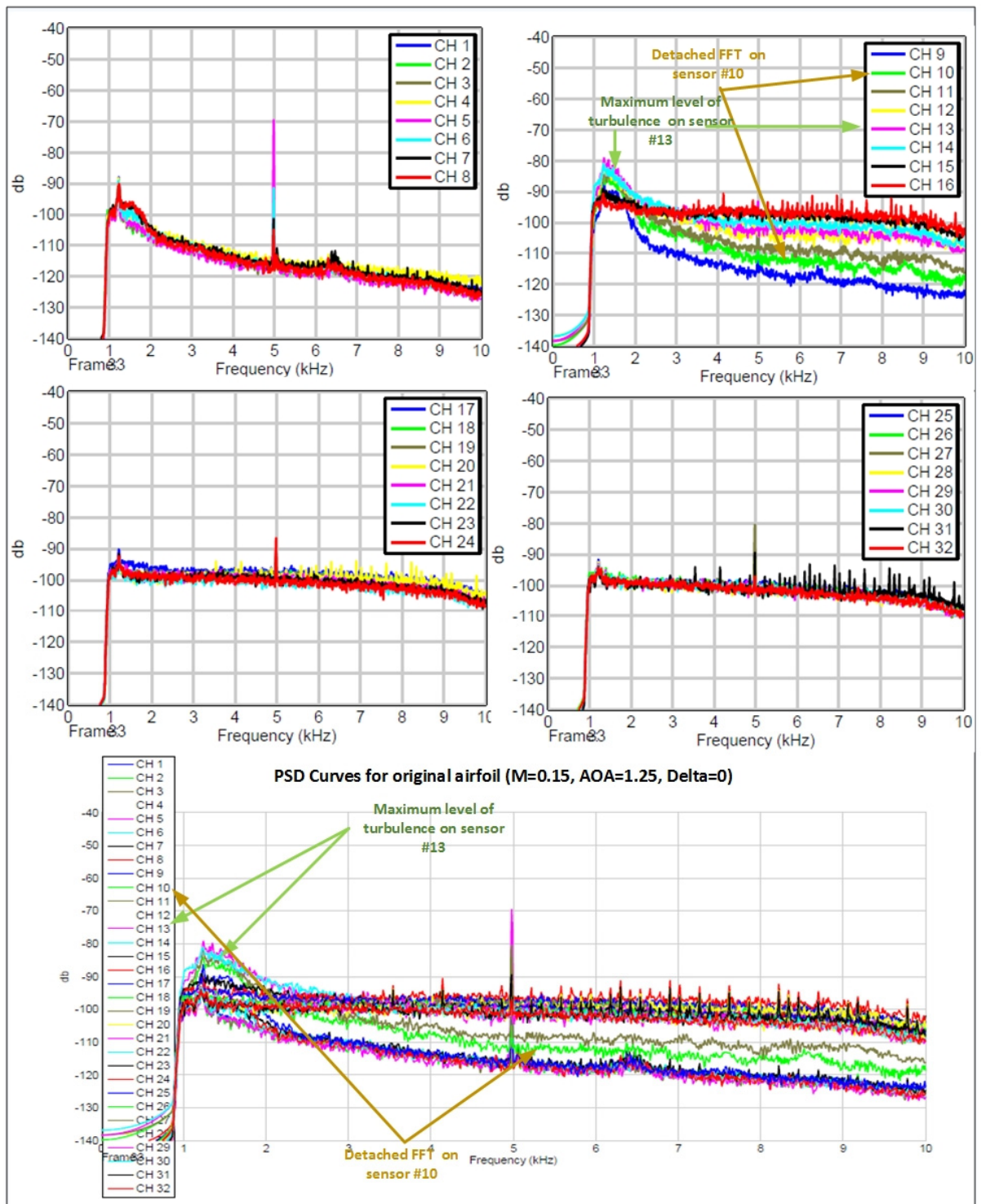


Figure 4.11 PSD representation for the original airfoil, case #41 (Mach=0.15, $\alpha=1.25^\circ$, $\delta=0^\circ$)

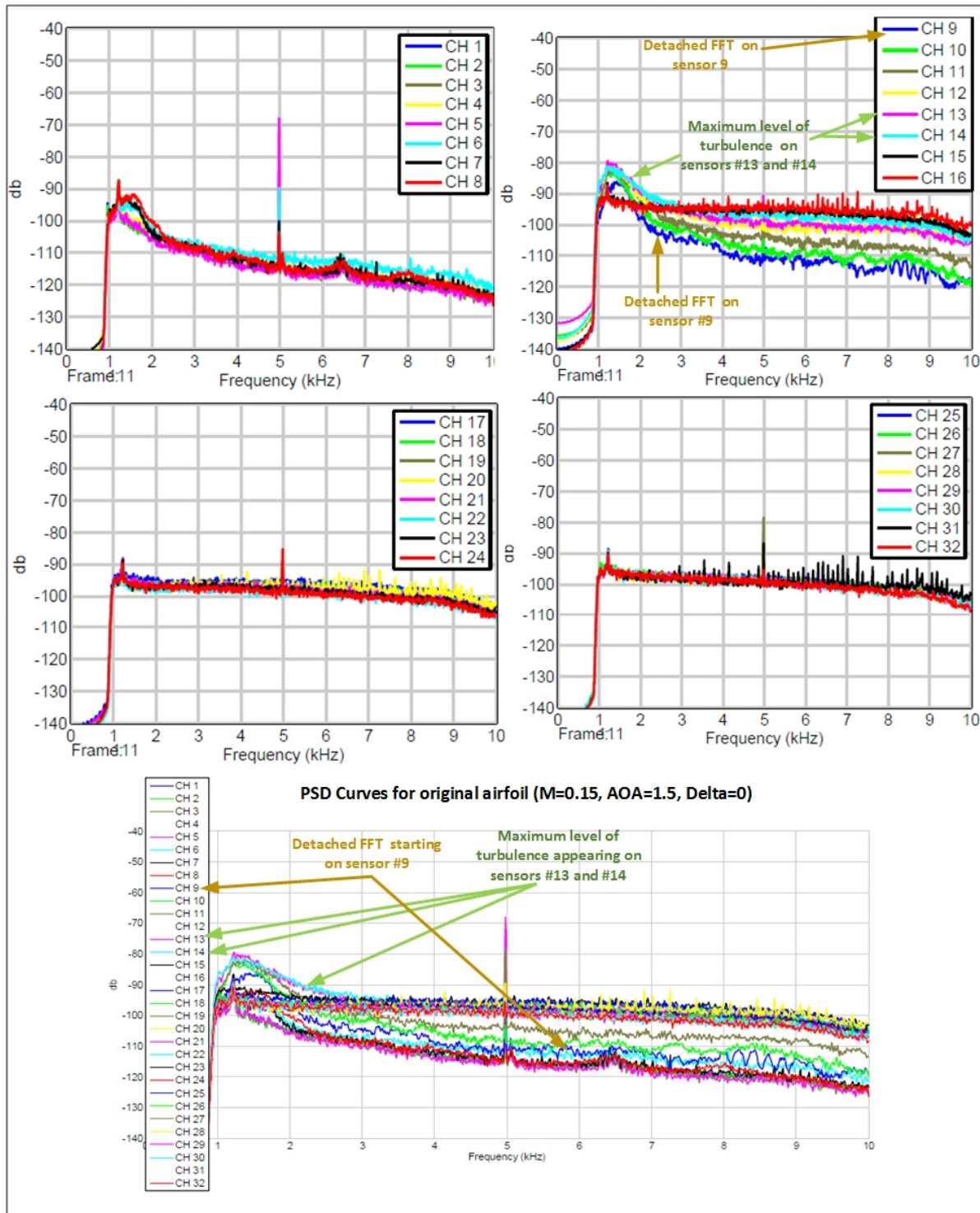


Figure 4.12 PSD representation for the original airfoil, case #42 ($Mach=0.15$, $\alpha=1.5^\circ$, $\delta=0^\circ$)

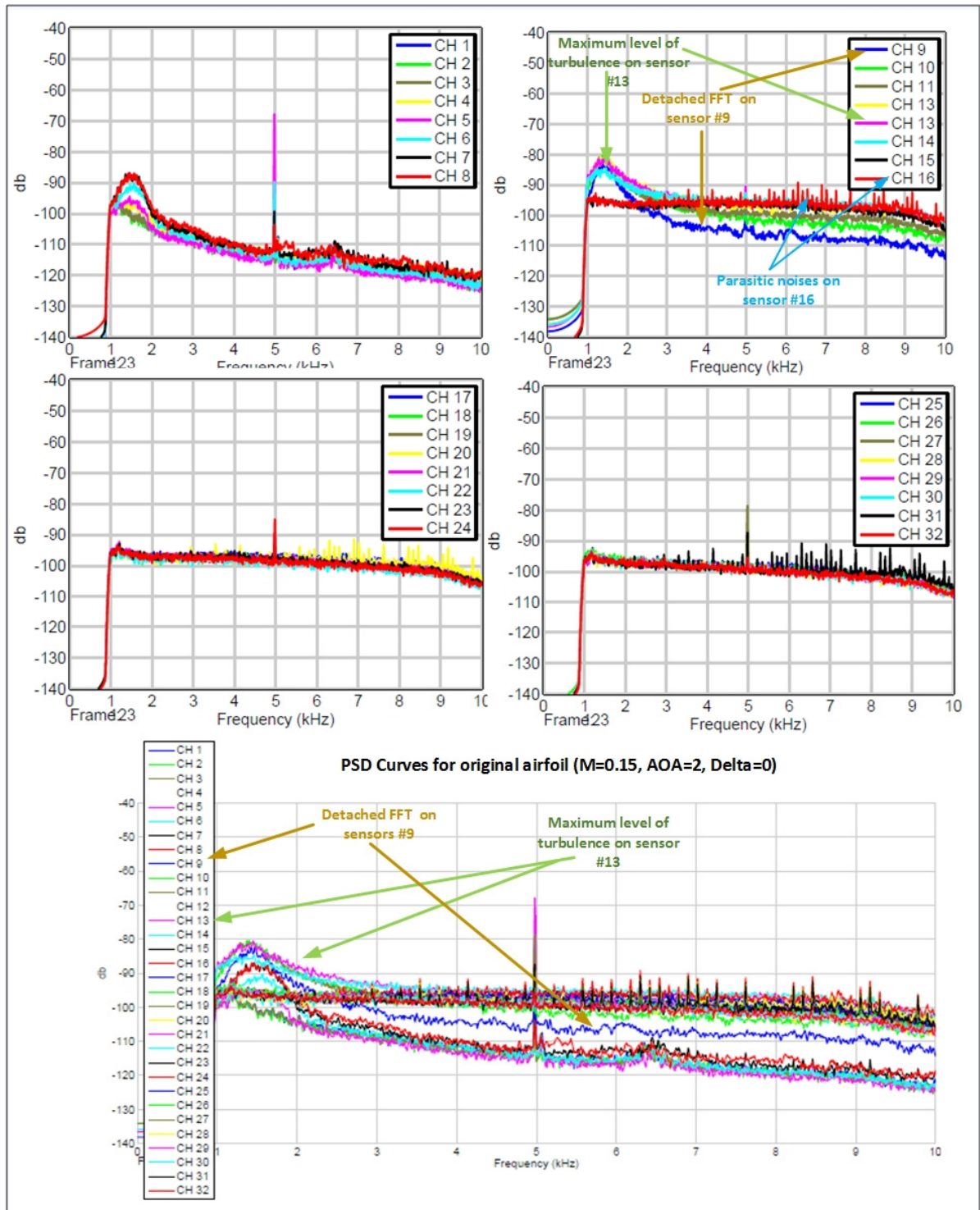


Figure 4.13 PSD representation for the original airfoil, case #43 ($Mach=0.15$, $\alpha=2^\circ$, $\delta=0^\circ$)

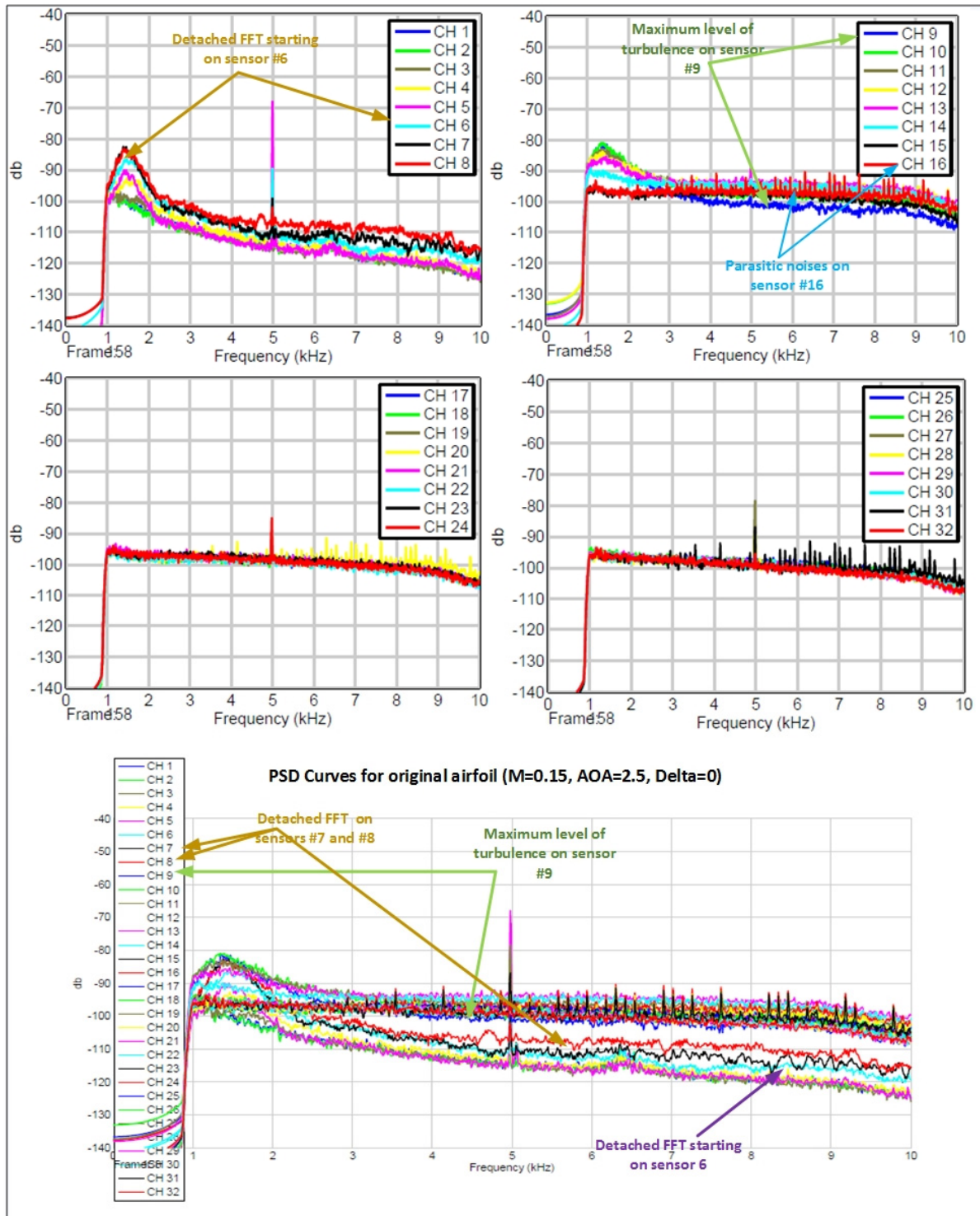


Figure 4.14 PSD representation for the original airfoil, case #44 (Mach=0.15, $\alpha=2.5^\circ$, $\delta=0^\circ$)

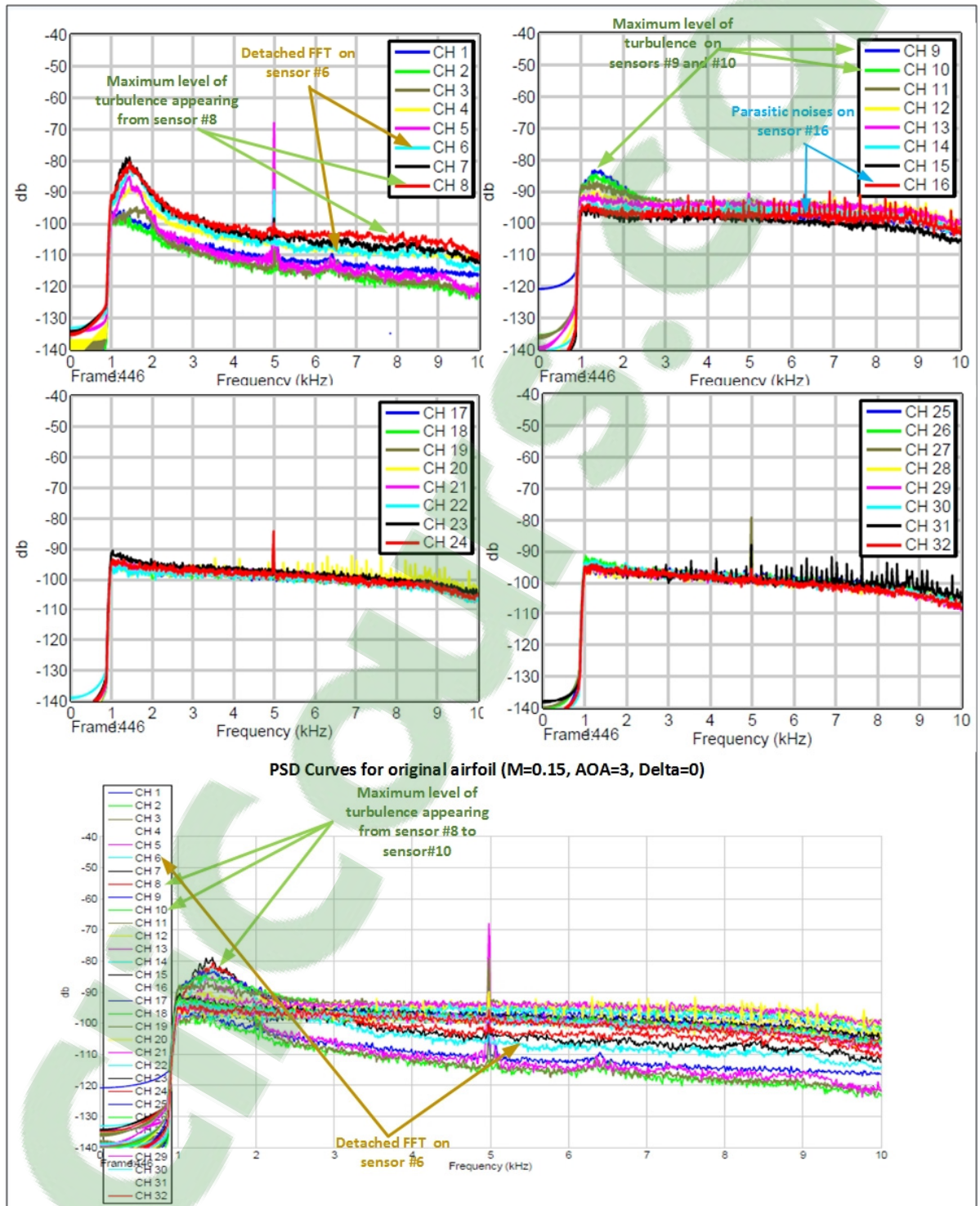


Figure 4.15 PSD representation for the original airfoil, case #45 (Mach=0.15, $\alpha=3^\circ$, $\delta=0^\circ$)

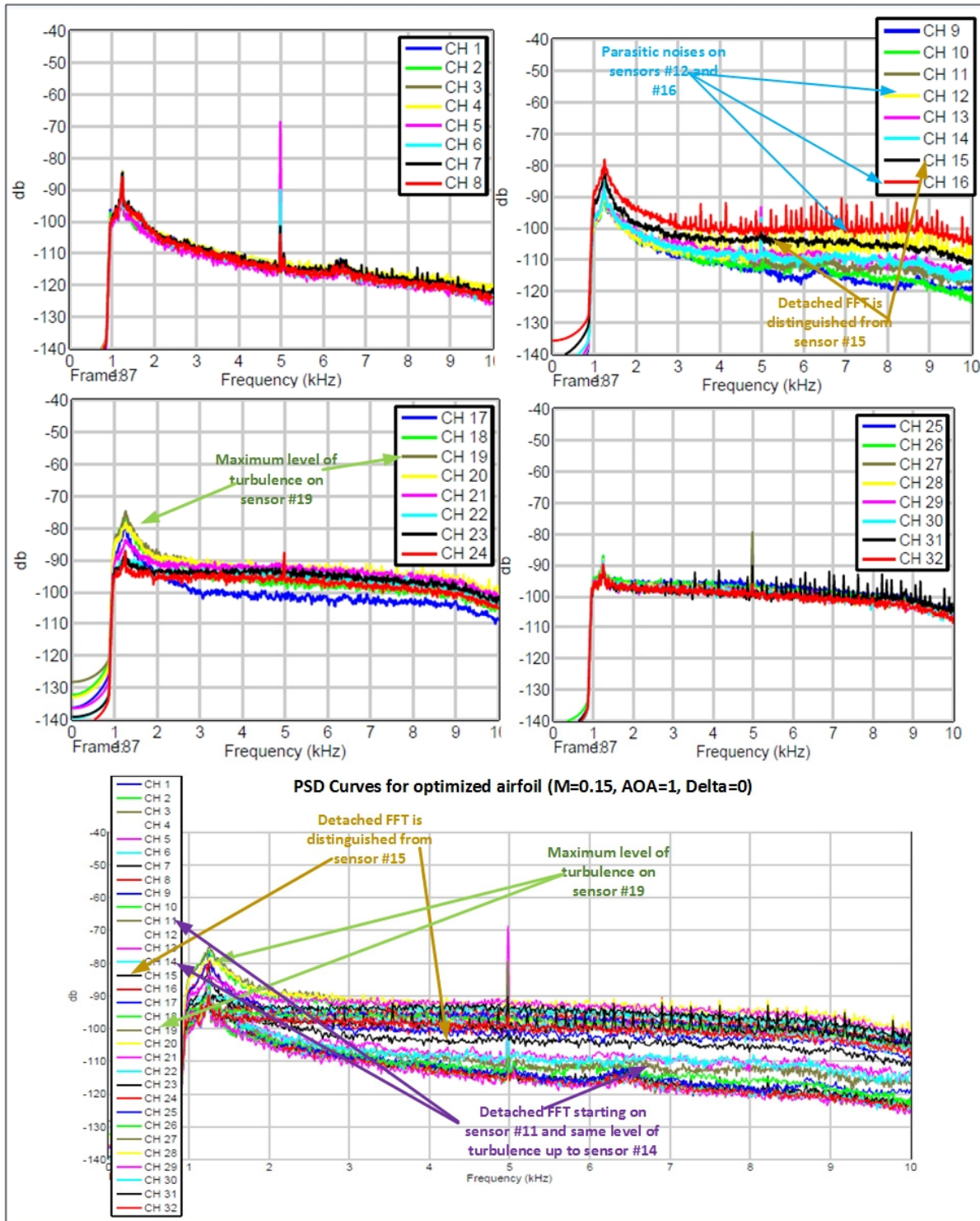


Figure 4.16 PSD representation for the optimized airfoil, case #40 (Mach=0.15, $\alpha=1^\circ$, $\delta=0^\circ$)

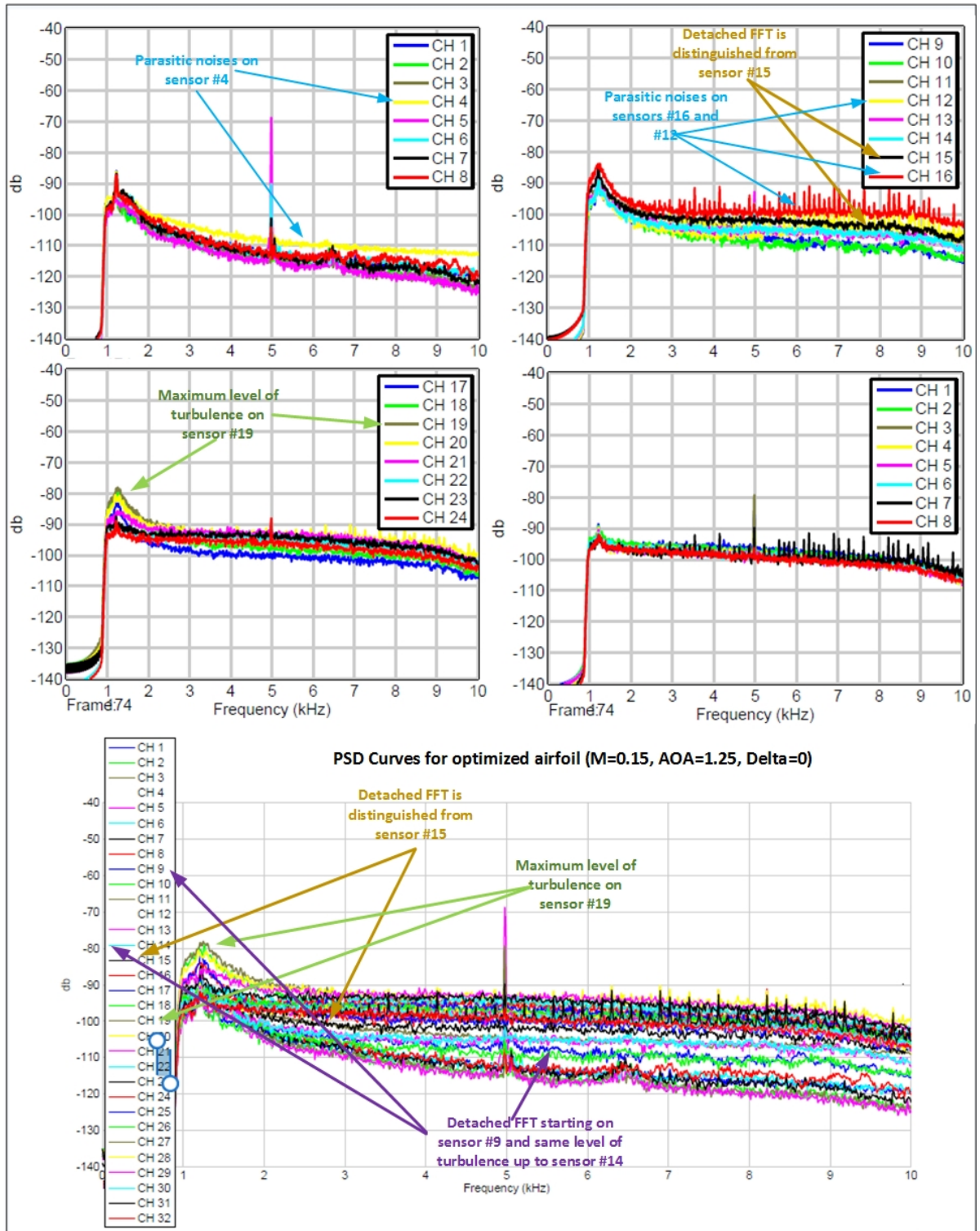


Figure 4.17 PSD representation for the optimized airfoil, case #41 (Mach=0.15, $\alpha=1.25^\circ$, $\delta=0^\circ$)

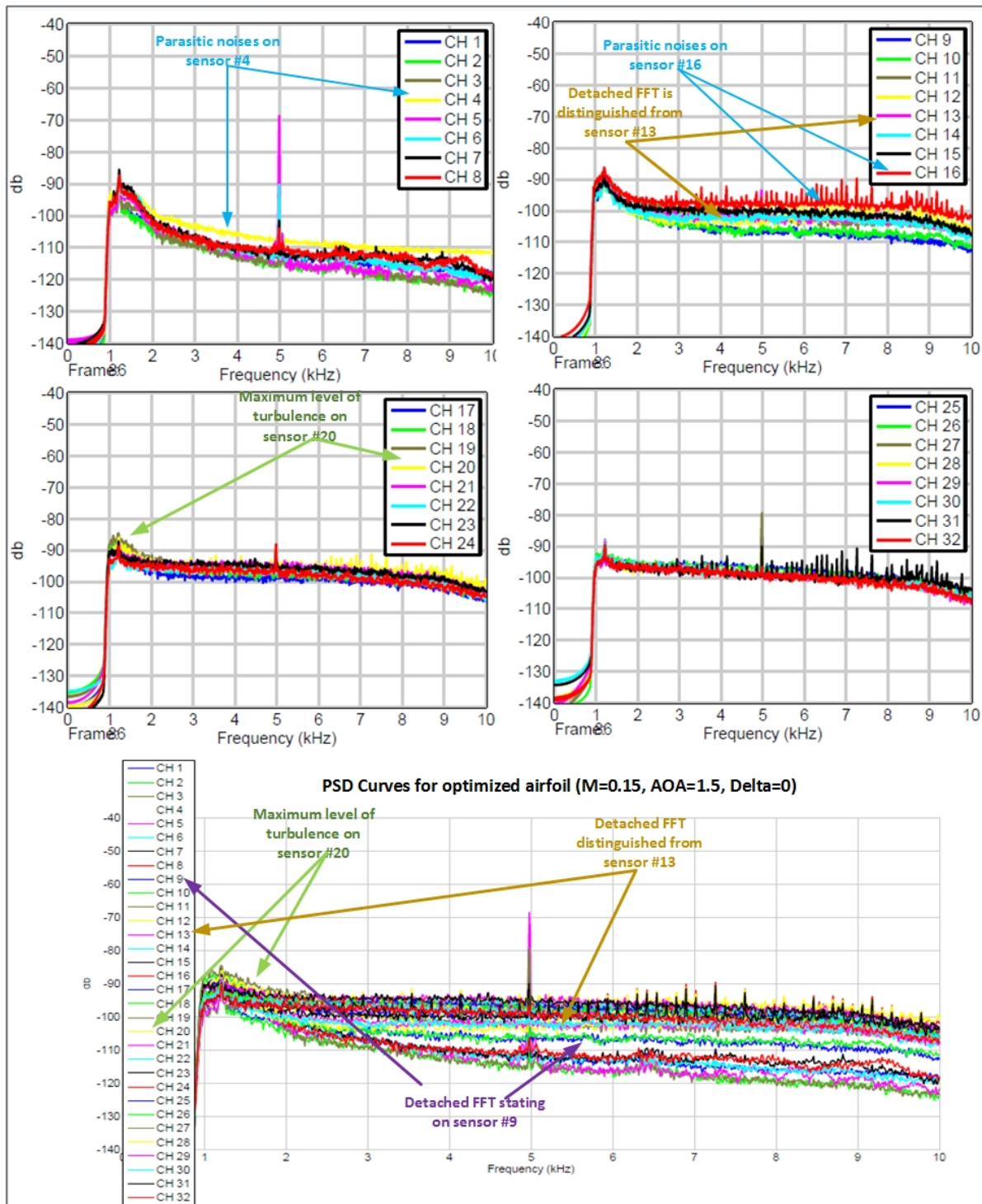


Figure 4.18 PSD representation for the optimized airfoil, case #42 (Mach=0.15, $\alpha=1.5^\circ$, $\delta=0^\circ$)

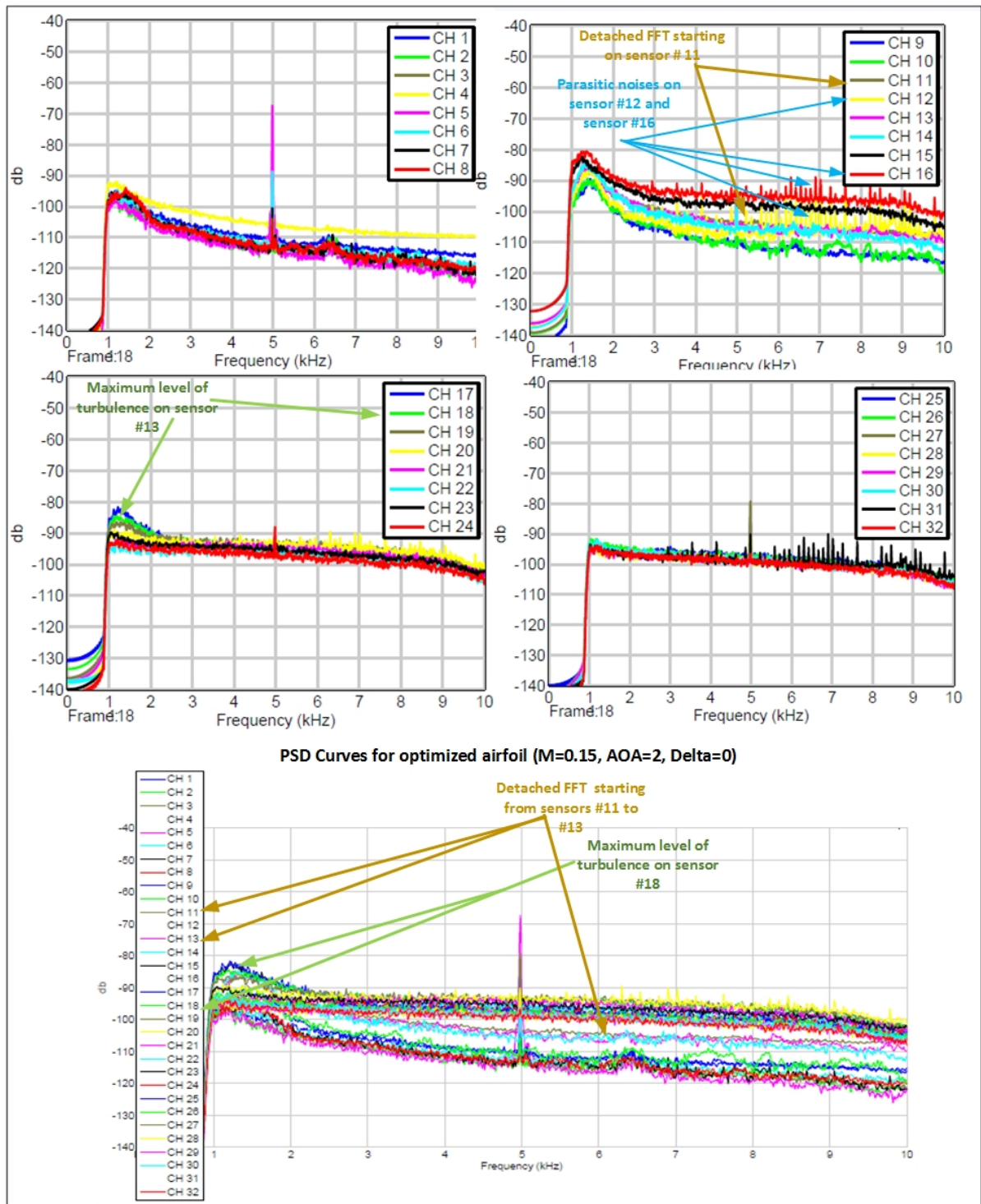


Figure 4.19 PSD representation for the optimized airfoil, case #43 ($Mach=0.15$, $\alpha=2^\circ$, $\delta=0^\circ$)

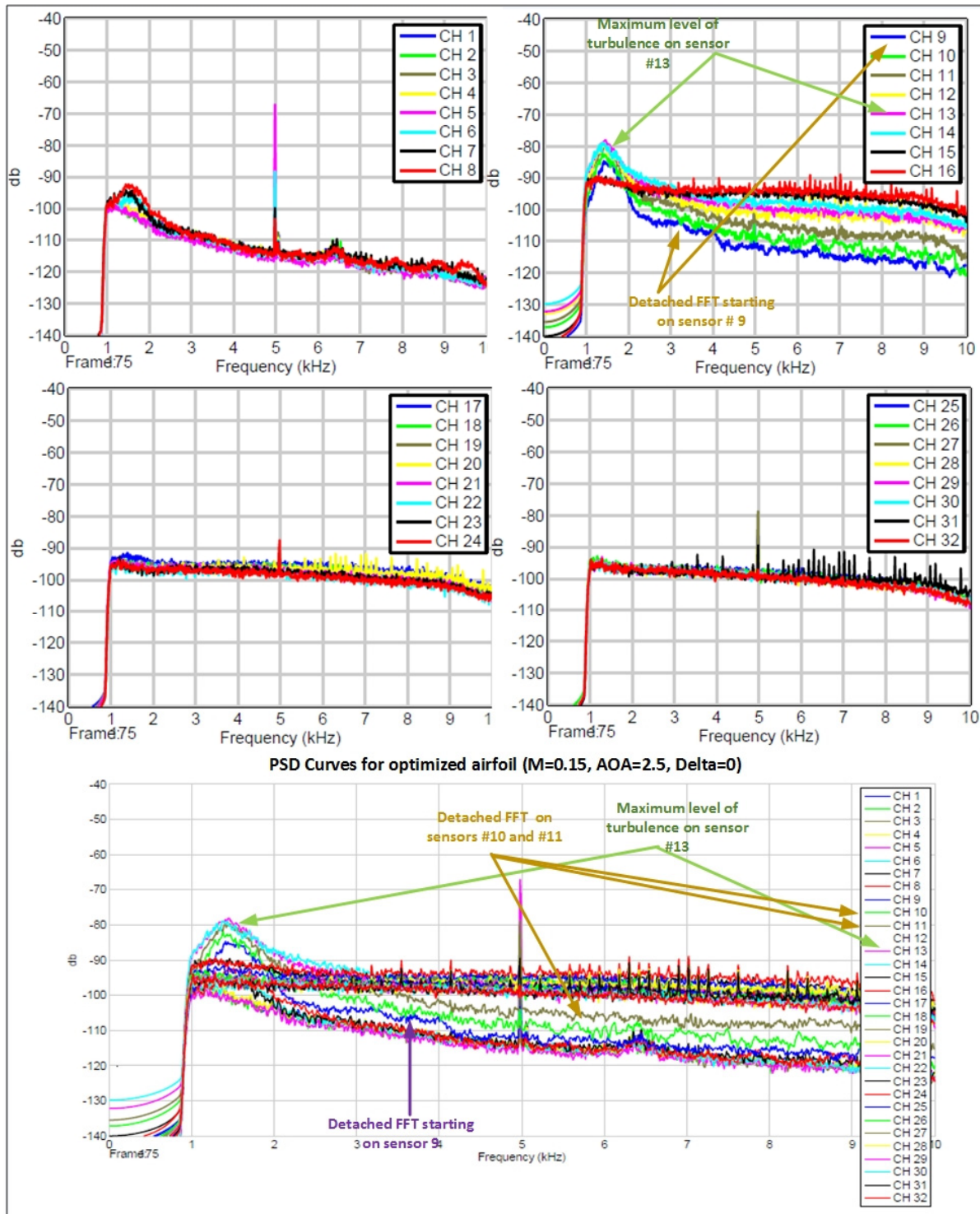


Figure 4.20 PSD representation for the optimized airfoil, case #44 ($Mach=0.15$, $\alpha=2.5^\circ$, $\delta=0^\circ$)

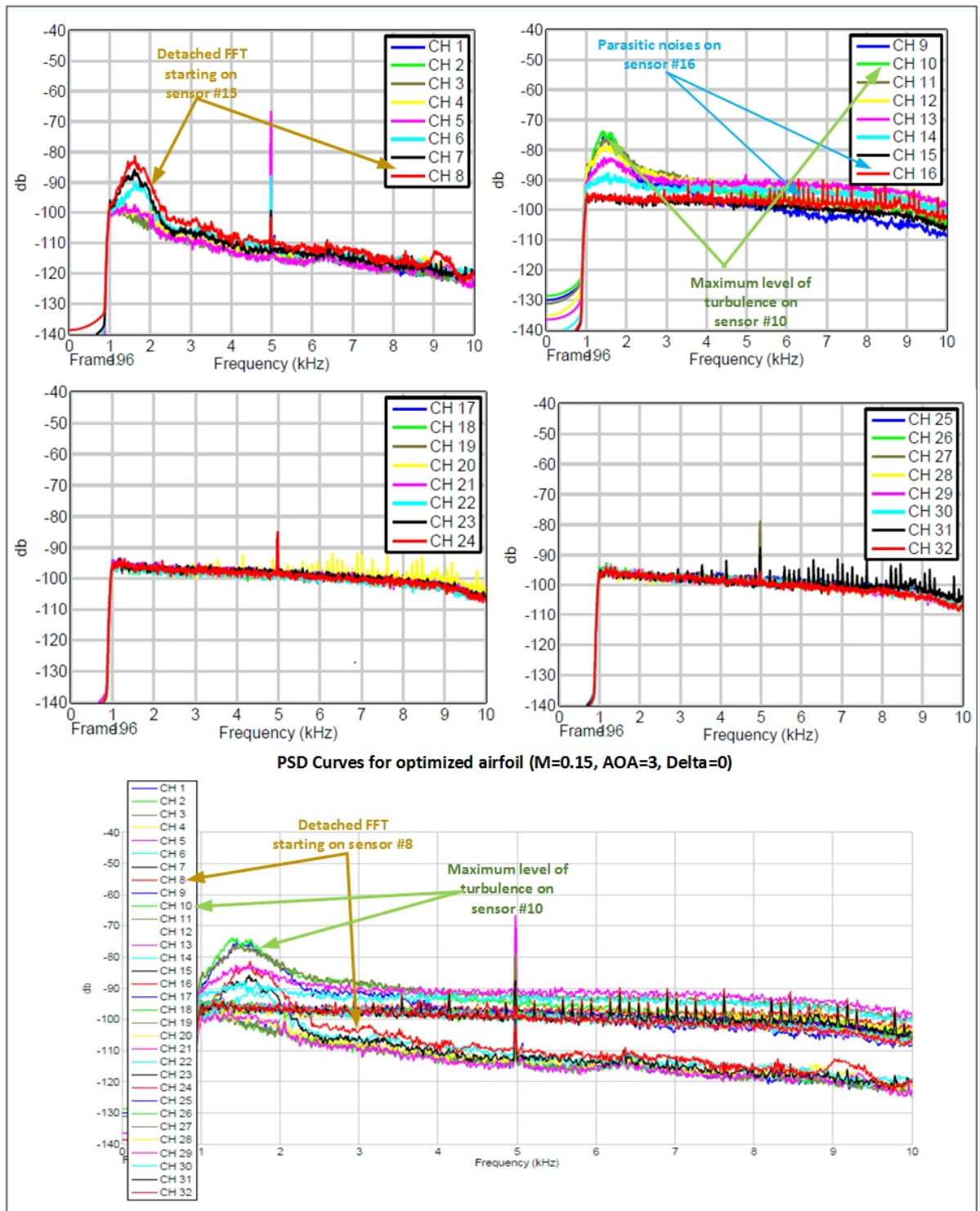


Figure 4.21 PSD representation for the optimized airfoil, case #45 ($Mach=0.15$, $\alpha=3^\circ$, $\delta=0^\circ$)

Figure 4.22 shows the average flow transition location for the chord located at closed to 40% of the wing span for flight cases 40 to 45. The transition was found using XFOIL software and was experimentally detected by Kulite sensors, for original and optimized airfoils.

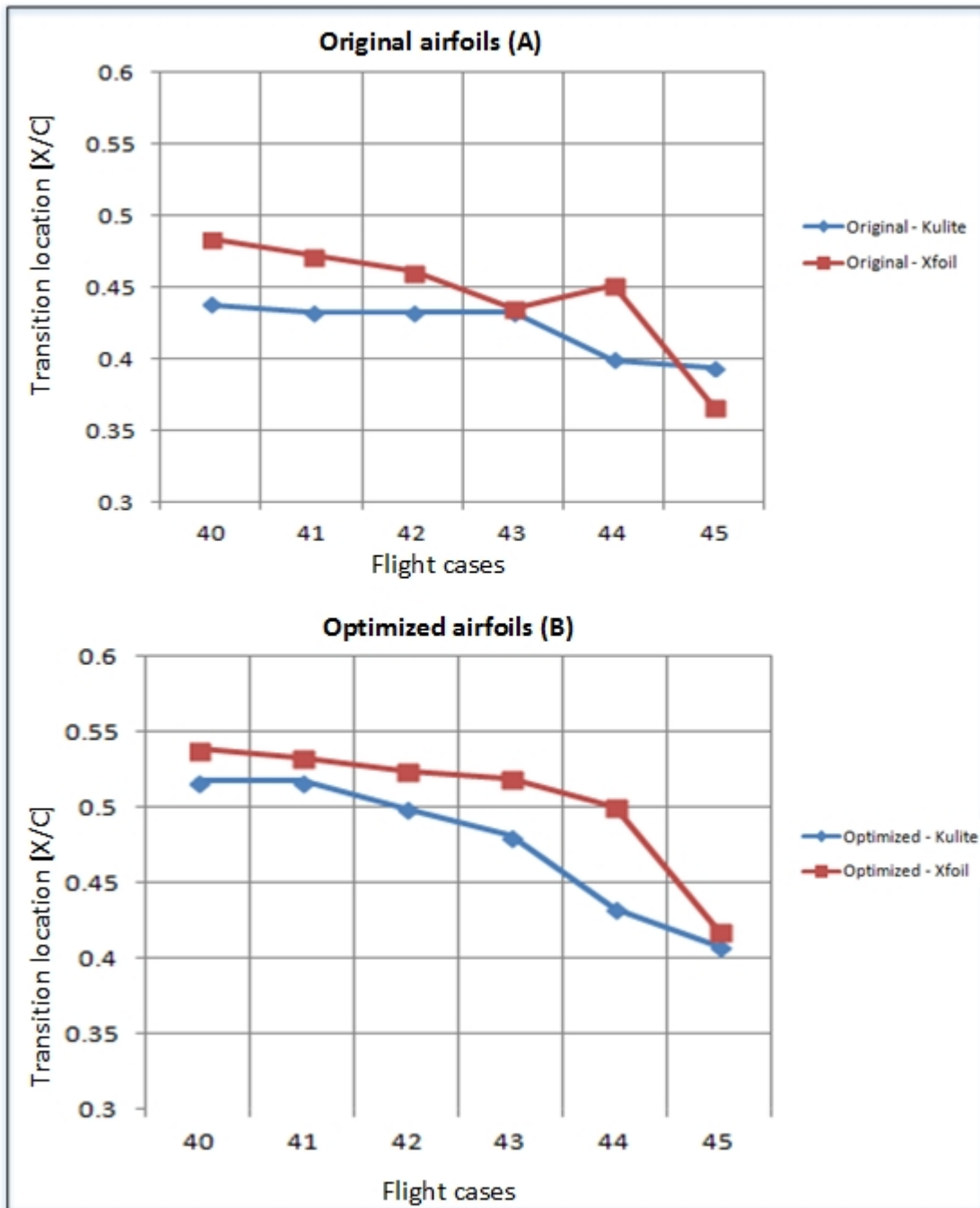


Figure 4.22 Average transition location calculated with 2D XFOIL software and experimentally determined with Kulite sensors, for case #40 to case #45.

On this figure, it is clear that there is a reasonable agreement between the 2D XFOIL predictions and the experimental results obtained for the flow transition location on the chord, as well as successful improvement of the laminar flow resulting in the delay of the transition location toward the leading edge. From the aerodynamic balance measurements, these transition delays produced the drag reduction indicated on Table 4.2, while the lift remained constant. In addition, it can be seen that the experimental results show a transition occurrence earlier than that of the numerical predictions for most flight configurations (for both original and optimized airfoils) at 2.5% of the chord on average ($0.025 [X/C]$ on the figure). The numerical and experimental results are superposed for the original airfoil of flight case #43.

Table 4.2 Experimental wing lift and drag coefficients for un-morphed and morphed wing configurations for case #40 to case #45

Case number	Original airfoil		Optimized airfoil		Drag variation [%]
	CL	CD	CL	CD	
40	0.2150	0.0156	0.2165	0.0156	-0.20%
41	0.2324	0.0168	0.2329	0.0167	-0.47%
42	0.2483	0.0180	0.2490	0.0178	-0.51%
43	0.2794	0.0206	0.2788	0.0204	-0.60%
44	0.3102	0.0235	0.3109	0.0234	-0.40%
45	0.3434	0.0267	0.3424	0.0266	-0.23%

As shown in Table 4.2, the wind tunnel balance measurements show that the morphing of the upper surface skin caused a reduction of the wing model's drag coefficient, with values between 0.20% and 0.60%.

In addition, comparisons in terms of flow transition area location between pressure fluctuation analysis results and infrared visualization results (for the section situated at 40% of the wing span) are displayed on Figure 4.23 for original airfoils and on Figure 4.24 for optimized airfoils.

For the original airfoils, Figure 4.23 displays an average difference of about 5% of the chord (0.05 [X/C] on the figure) between the Kulite sensors and the infrared measurement's detection. Since the angles of attack vary with different flight cases (Table 2.2), the overall influence of the angle of attack variation is clearly visible via Kulite and infrared measurements for both original and optimized airfoils. A better agreement between the two experimental methods was obtained for the optimized airfoil, as seen on Figure 4.24.

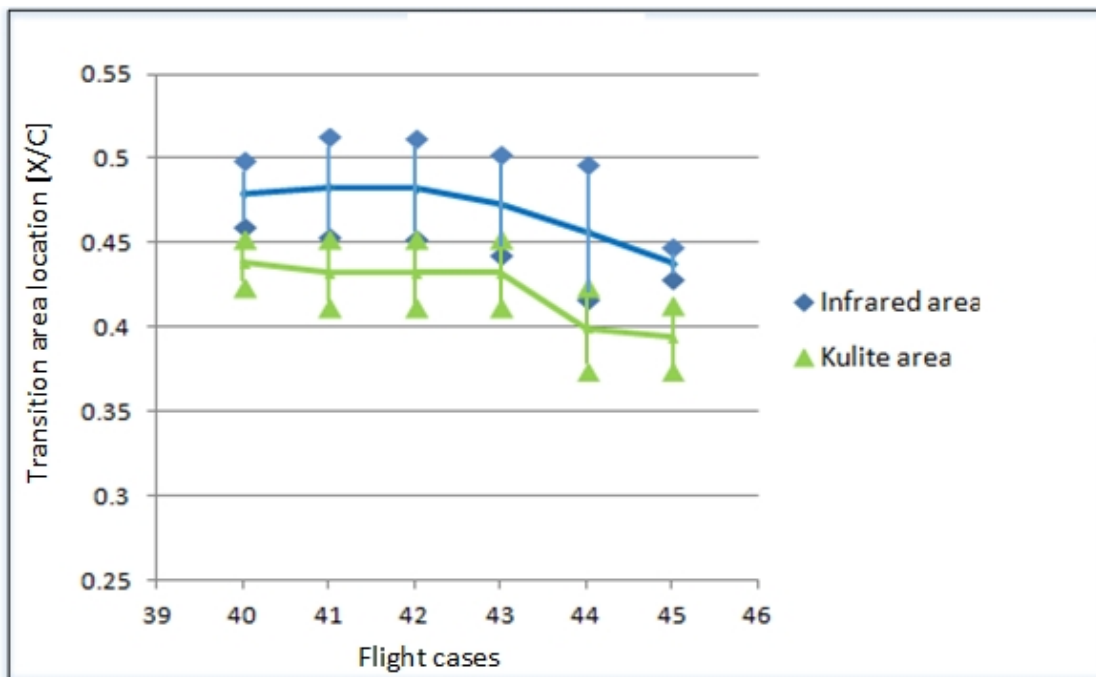


Figure 4.23 Comparison between Kulite sensor results and infrared measurements in terms of the transition location for the original airfoils- case #40 to case #45

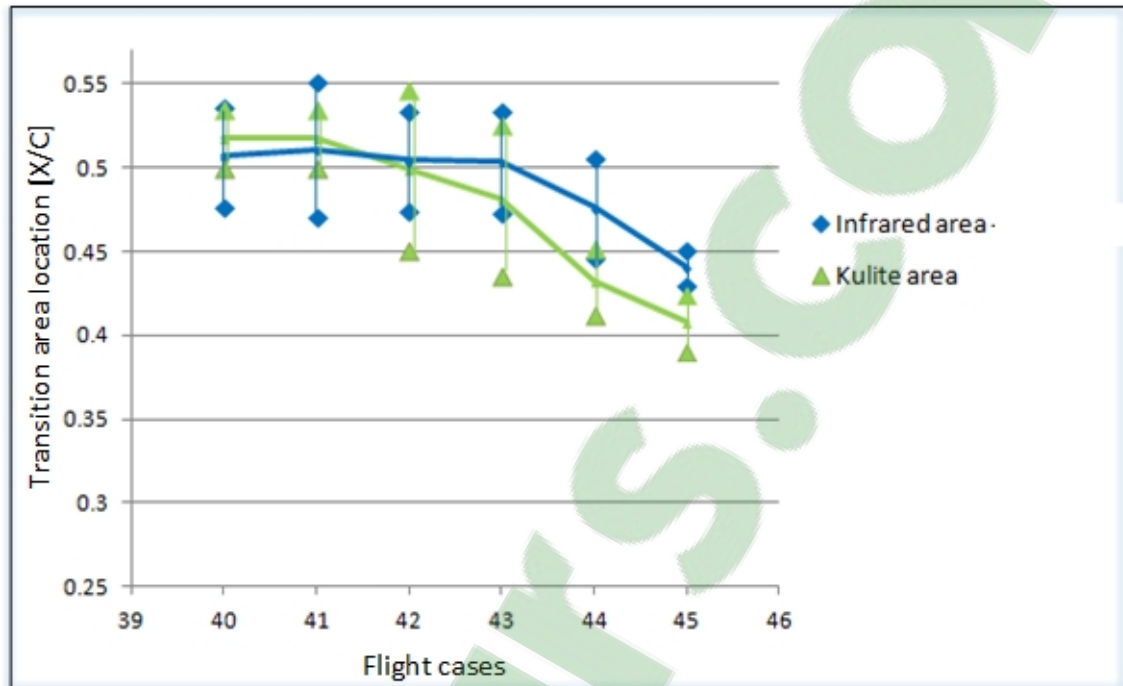


Figure 4.24 Comparison between Kulite sensor results and infrared measurements in terms of flow transition location for the optimized airfoils - case #40 to case# 45

4.3 Vibration Experimental Results

Following the second phase of wind tunnel test at NRC, post-processing of the accelerometer data was performed using Matlab software, according to the procedure described in section 3.2.2.2. The results are displayed for the cases shown in Table 4.3. Case #22, case #68 and case #37 allow us to evaluate the effect of the Mach number (speed) variation (since the angle of attack remains constant), while cases #37, #35, #86 and #83 show the effect of the angle of attack variation (with a constant speed) on the recorded amplitudes and frequencies.

Table 4.3 Maximum Amplitudes of the Recorded Accelerations

Maximum amplitude								
Case number	Mach number	Angle of attack	Wing accelerometer (m/s ²)			Aileron accelerometer (m/s ²)		
			X axis	Y axis	Z axis	X axis	Y axis	Z axis
22	0.15	0°	0.3326	0.3715	0.4334	0.4227	0.4895	1.3537
68	0.2	0°	0.9307	0.9295	0.9776	1.3039	1.3476	2.7924
37	0.25	0°	0.7749	0.9416	1.1429	1.1921	1.2958	3.6388
35	0.25	1°	0.5785	0.7980	1.0078	0.8838	1.1342	3.9850
86	0.25	2°	0.5013	0.7237	0.9190	0.8487	1.0412	4.1031
83	0.25	3°	0.5881	0.8223	0.9979	0.9495	1.0989	3.9648

Figure 4.25 to Figure 4.30 show the recorded amplitudes in terms of time and frequency for various flight cases in the wind tunnel. The maximum amplitude accelerations are displayed in blue for an optimal visualization, and shown on Table 4.3. Some "exceeding" of the recorded waveforms relative to the specified limits (maximum amplitude acceleration) is clearly visible. This "exceeding" occurred because the maximum acceleration amplitudes were computed assuming that the wing motion was perfectly sinusoidal. The non-sinusoidal signals resulting from the wind tunnel and its equipment noises may affect the recorded waveforms by interfering with the wing acceleration signal. These "exceedings" are therefore not representative of the actual wing motion variation and can be safely neglected.

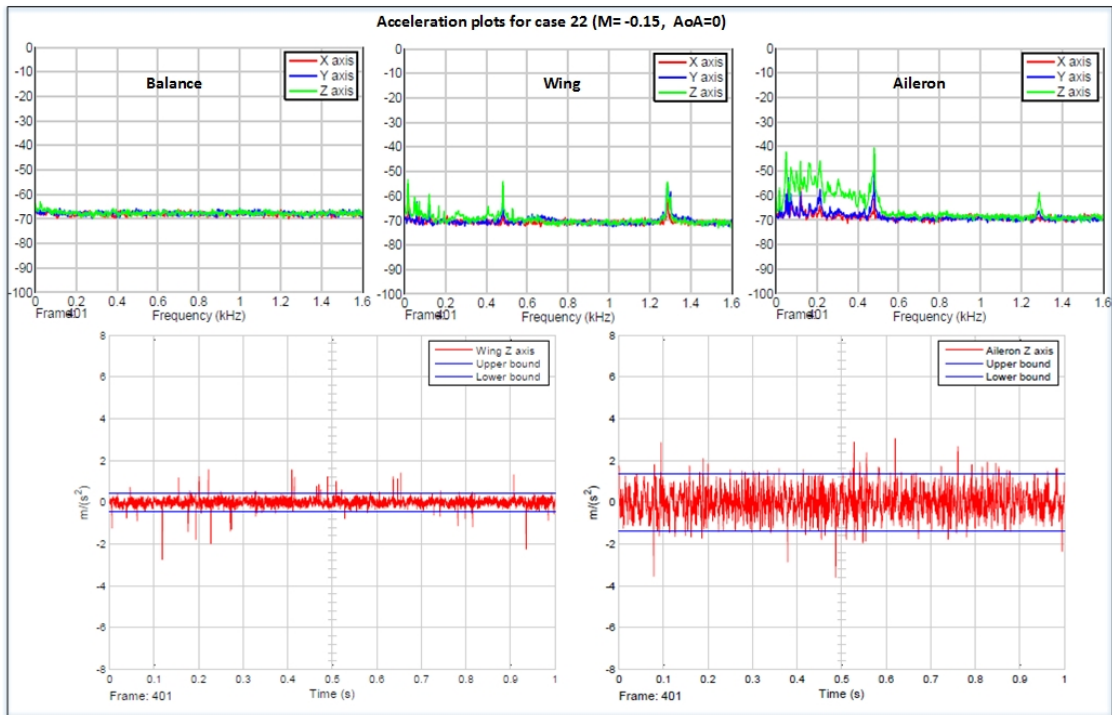


Figure 4.25 Time and frequency domain representations of recorded accelerations
Mach number = 0.15, angle of attack = 0°

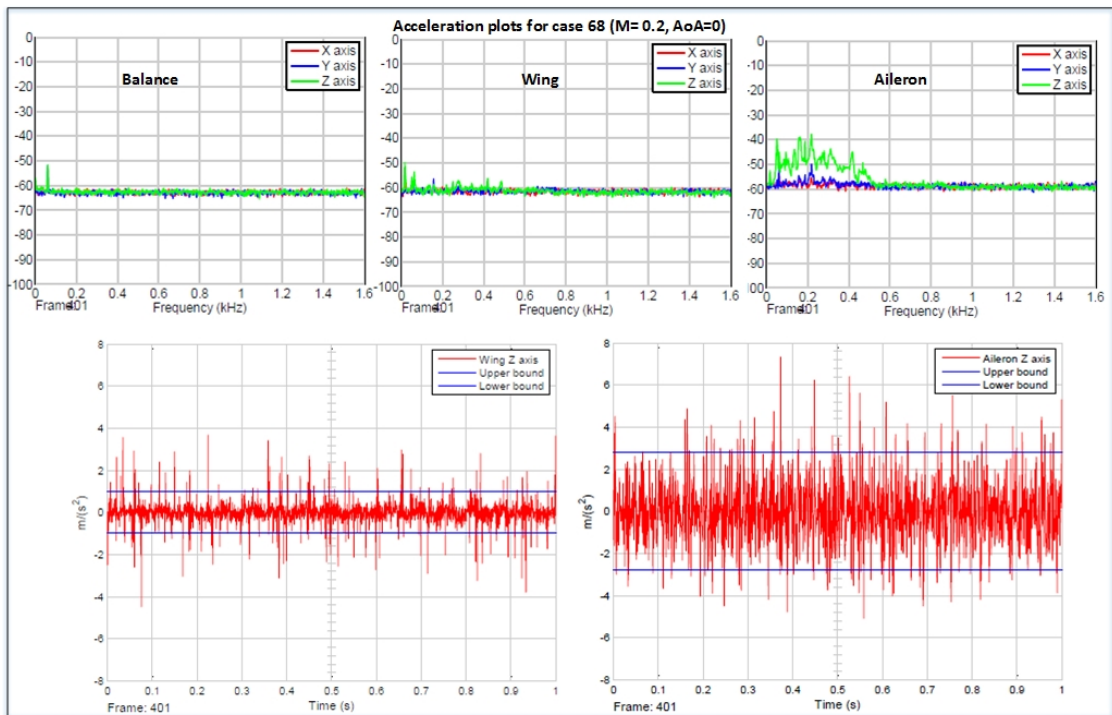


Figure 4.26 Time and frequency domain representations of recorded accelerations
Mach number = 0.2, angle of attack = 0°

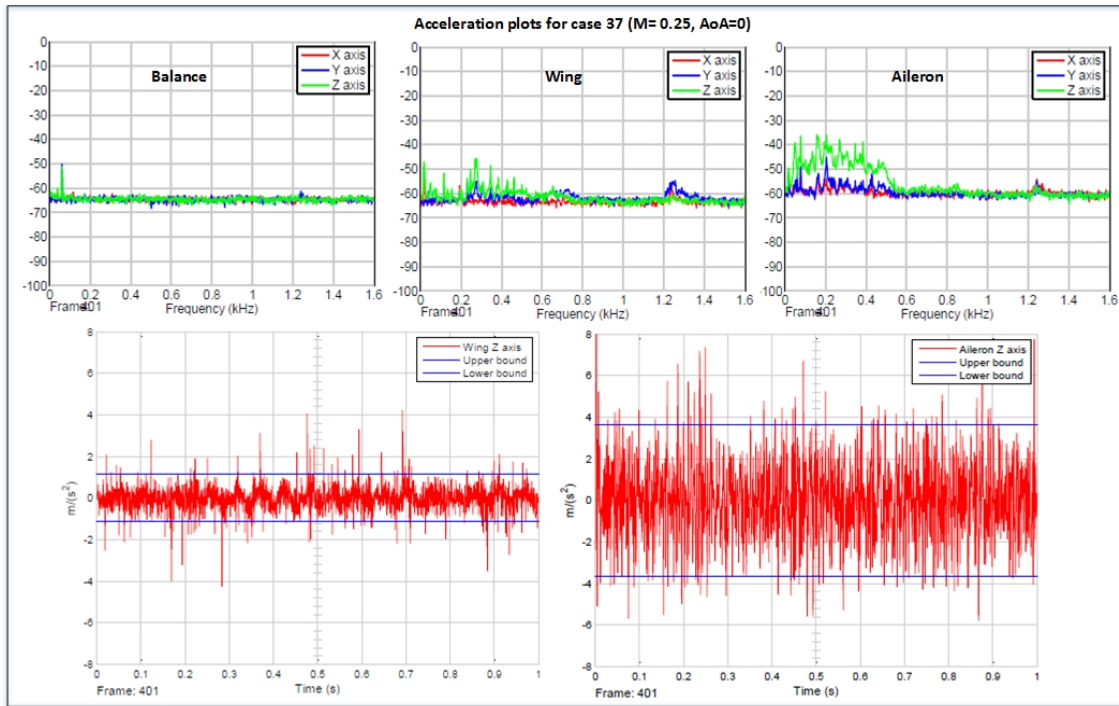


Figure 4.27 Time and frequency domain representations of recorded accelerations
Mach number = 0.25, angle of attack = 0°

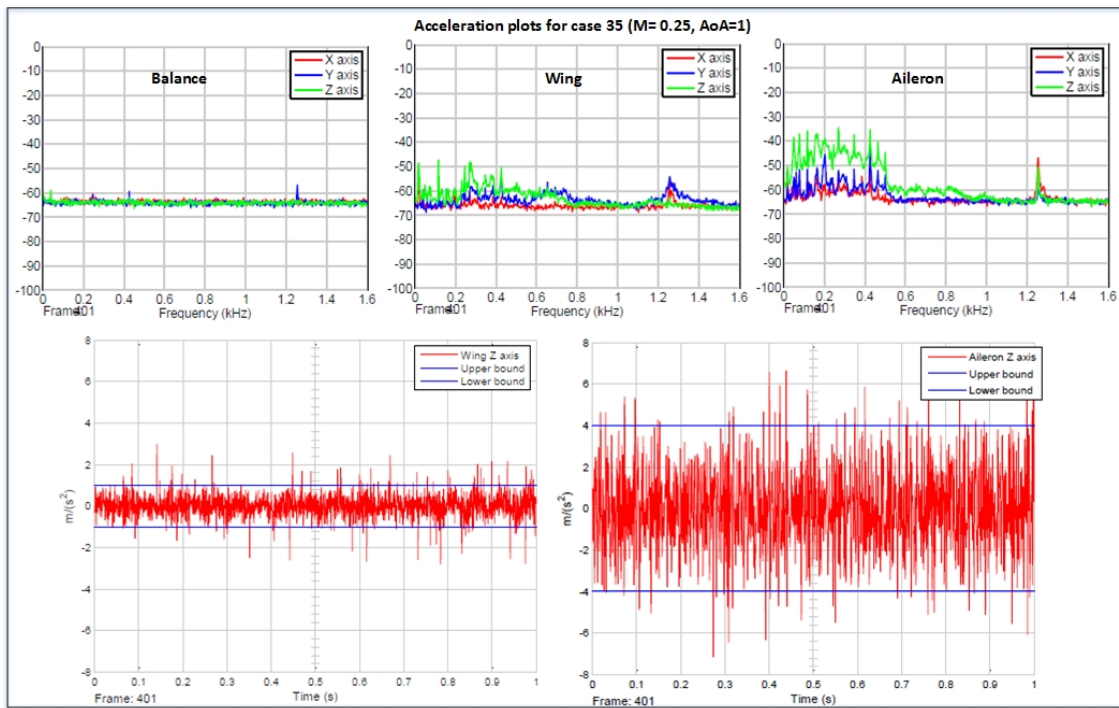


Figure 4.28 Time and frequency domain representations of recorded accelerations
Mach number = 0.25, angle of attack = 1°

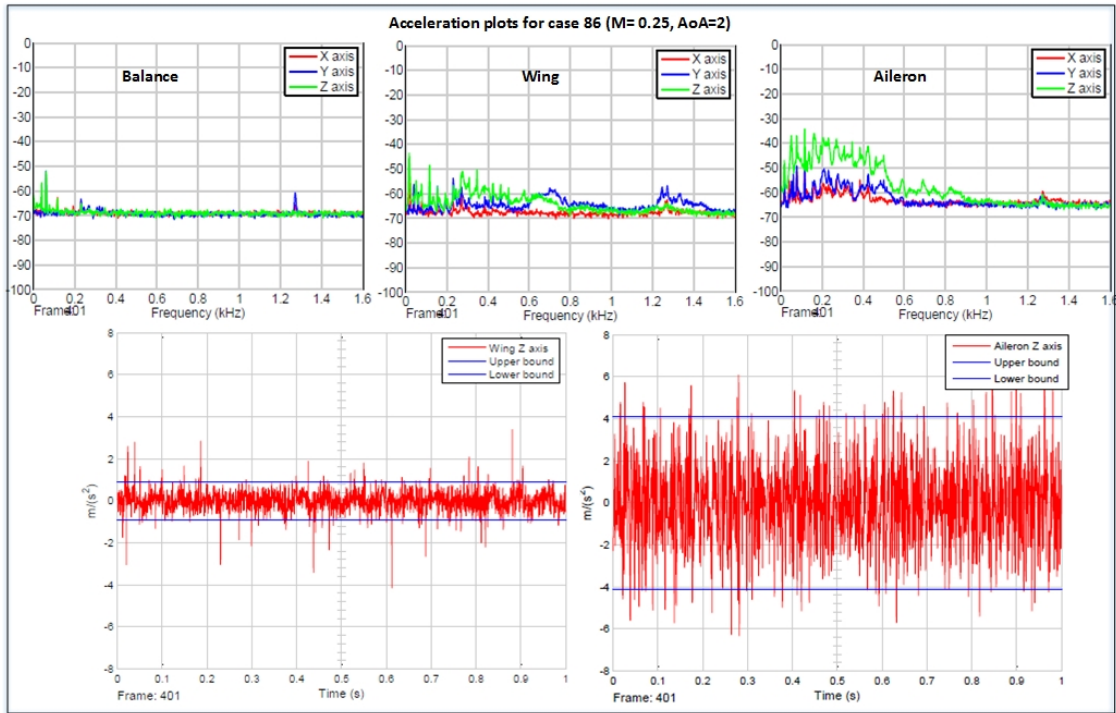


Figure 4.29 Time and frequency domain representations of recorded accelerations
Mach number = 0.25, angle of attack = 2°

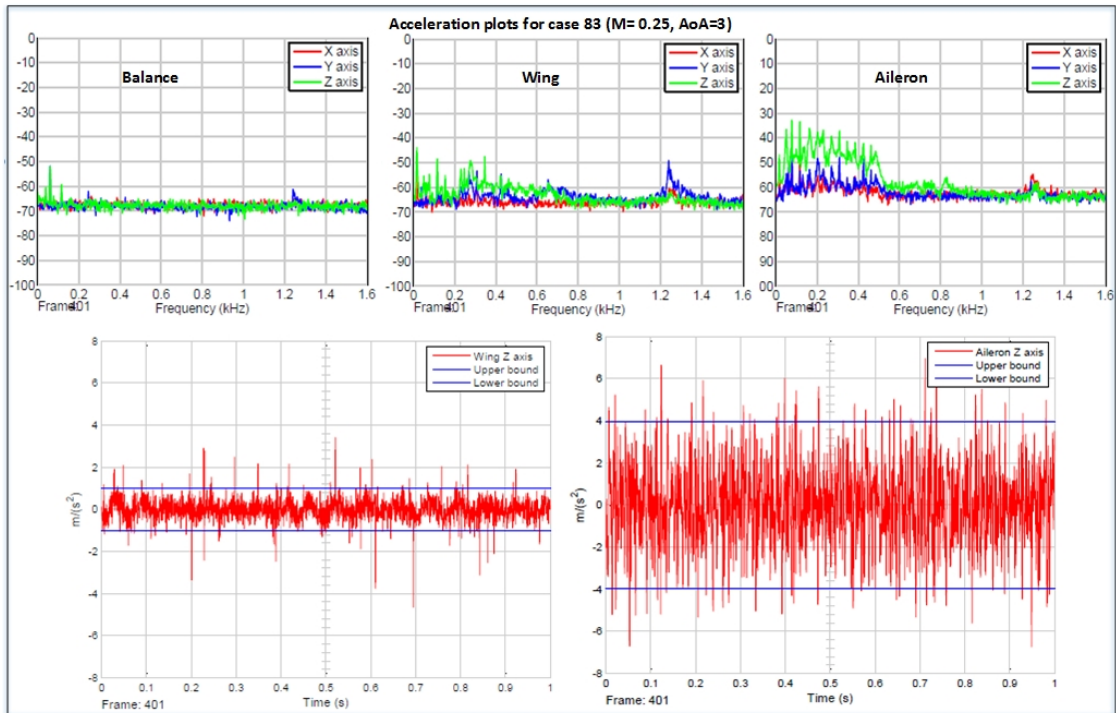


Figure 4.30 Time and frequency domain representations of recorded accelerations
Mach number = 0.25, angle of attack = 3°

The upper portions of Figure 4.25 through Figure 4.30 indicate the frequency domain displays of each accelerometer's channel (in three graphs) and the lower portions show the time domain display of the accelerometers' wing and aileron Z-axes (in two graphs). Only the accelerations' Z-axes are presented in the time domain (for illustration), because they were the ones most affected by the vibrations. Nevertheless, the amplitudes of the X and Y axes' accelerations can be visualized in the frequency domain on the figures. The figures confirm that the accelerometer installed on the aileron was more affected by the vibration than the one installed on the wing. This behavior was expected because the aileron was installed as a free body fixed to the wing by an external actuator, and therefore it (the aileron) was the most flexible part of the demonstrator. The influence of the airspeed (Mach number) on the magnitude of the acceleration can be observed. The magnitudes for cases with Mach number = 0.25 was more than two times the magnitudes obtained for cases with Mach number = 0.15. Of courses, the overall accelerations' magnitudes remained small, as they correspond to the small displacements occurring on the prototype composed of the wing and the aileron.

From the PSD plots appearing in Figure 4.25 to Figure 4.30, we can see that the accelerations occurring on the balance remained small and could be neglected with respect to the accelerations occurring on the wing and aileron. The presence of the first ten vibration modes was clearly visible on the wing and the aileron's PSD figures between 0 Hz and 450 Hz, as predicted by aeroelastic studies (Koreanschi *et al.*, 2016). The amplitudes of the vibrations were distributed along three accelerometer' axes with different magnitudes. In addition, less important modes (in terms of amplitudes) occurred around 1,300 Hz, and can be visualized on the X and Y axis of the wing and aileron accelerations' PSD figures (the Z axes' accelerations can be measured only up to 550 Hz, according to the from accelerometers' specification).

Overall, this study found that the data recorded from accelerometers for the speeds at which the wing demonstrator was tested, indicates that no aeroelastic dynamic or static phenomena occurred; and therefore that the wind tunnel tests on the demonstrator were conducted within

the safety limits. The flutter numerical analysis was conducted by the LARCASE team in this project. The experimental results shown here validated the numerical results; as they had predicted that flutter was not supposed to occur at any Mach number lower than 0.3.

CONCLUSION

The present thesis highlights the contributions to the successful realization of the MDO 505 project. These contributions include the acquisition, post-processing and interpretation of the pressure experimental data during IAR-NRC wind tunnel tests on a morphing wing tip. These tests were conducted to characterize the behavior of a morphing wing tip in airflow with a primary objective of localizing the laminar to turbulent boundary layer transition region of the air flow. The secondary objective is the real time acquisition and monitoring of the wing model vibrations during the tests in order to ensure the safe behavior of the wing.

The morphing wing tip was manufactured and equipped with a composite material upper skin. The real time acquisition of the pressure data was successfully performed during multiple sets of tests at the IAR-NRC wind tunnel. Thirty-two (32) Kulite sensors supported by NI PXIes-4330 devices were used to sense pressure fluctuations on the wing flexible skin, at the rate of 20 KHz. The Kulite sensors were carefully installed on the wing skin so that the aerodynamic loads applied on the wing would not alter the sensors' readings.

Ninety seven (97) different flight configurations were simulated, optimized for transition delay and then tested at the IAR-NRC wind tunnel for the validation of their simulation results. 30 % of the tested configurations showed transition delay appearance, as result of the morphing. The "spectral analysis method" of the pressure distribution was used to determine the laminar to turbulent transition area at the wing chord situated at 40% of the span. Infra-Red (IR) measurements were performed to confirm the local transition obtained from pressure data results as well as to evaluate the transition region on the entire wing skin surface. Very good agreement was found between the two experimental methods (Kulite sensors and IR equipment). Comparisons between experimental pressure coefficients and numerical Xfoil and Fluent software predictions were also performed for the wing chord at 40% of the span section, revealing very good matches. The effects of the morphing were clearly visible on the pressure distribution plots. The lift and the drag coefficients were

experimentally determined for the tested cases via wind tunnel balance measurements, and the results showed a maximum drag reduction of 0.60%.

To assess the wing tip model vibrations caused by the aerodynamic loads during the wind tunnel tests, two ADXL-326 type accelerometers were installed on both the wing and the aileron boxes. The accelerometers were connected to a NI USB-6212 box for the handling and analysis of their real time data acquisition and the Analog to Digital Conversion (ADC) of the acquired voltage. The real time acceleration acquisitions were done at the frequency rate of 3.2 kHz, which allowed to visualize vibration frequencies up to 1.6 kHz. The real time processing and the vibration amplitude monitoring were managed via an in-house software installed on a personal computer. The acquired data were visualized in real time, in both time and frequencies domains. The vibrations' amplitudes were quantified through Standard Deviation (SD) methods, with the aim of preventing any aeroelastic phenomenon appearing during the tests. Fortunately, the vibration amplitudes remained relatively low during all the wind tunnel tests sets, as predicted by the wing model aeroelastic studies.

Having the opportunity to work on such a multidisciplinary project was a rewarding experience on many levels. Globally, the two main aspects of the research presented in this thesis, while they were studied for different purposes, both required the organization of real time data acquisition, the real time processing and the post processing of acquired data. These processes cannot only be applied to the aerospace domain; they can be utilized in all of the engineering industry, as the tests remain a valuable technique with which to validate new technologies. However, experimental work must be carefully analyzed and all the assumptions, environmental conditions and equipments limitations need to be considered. This thesis shows how to carefully manage series of data based on the expected results determined from numerical calculations so that no valuable information in the data will be overlooked. The experience and expertise made possible by working closely with multidisciplinary professionals in the aerospace domain certainly contributed to the success of this work.

Clicours.com

RECOMMENDATIONS

The research presented in this thesis could further be improved following the next comments:

- The post-processing of pressure data was time efficient because the interpretation of Standard deviation (SD) and Power Spectrum Density (PSD) figures was handmade during the data post processing. The suggestion for such future multidisciplinary project would be to find a method for the automatic dissociation of laminar PSD curves from the turbulent PSD curves, so that the detection of the transition zone can be automatically done and therefore exploitable in real time.
- The quantification of the wing vibrations amplitudes during the wind tunnel tests has been achieved successfully. One should improve this quantification by handling the real-time integration of data to convert accelerations to displacements, which are more representative of the vibrations amplitudes. However, it should required to erase in real-time (by filtering data for example) any undesirable noise that could alter the results of real-time conversation of acceleration to displacement.

ANNEX I

SPECIFICATIONS OF THE PRESSURE SENSORS

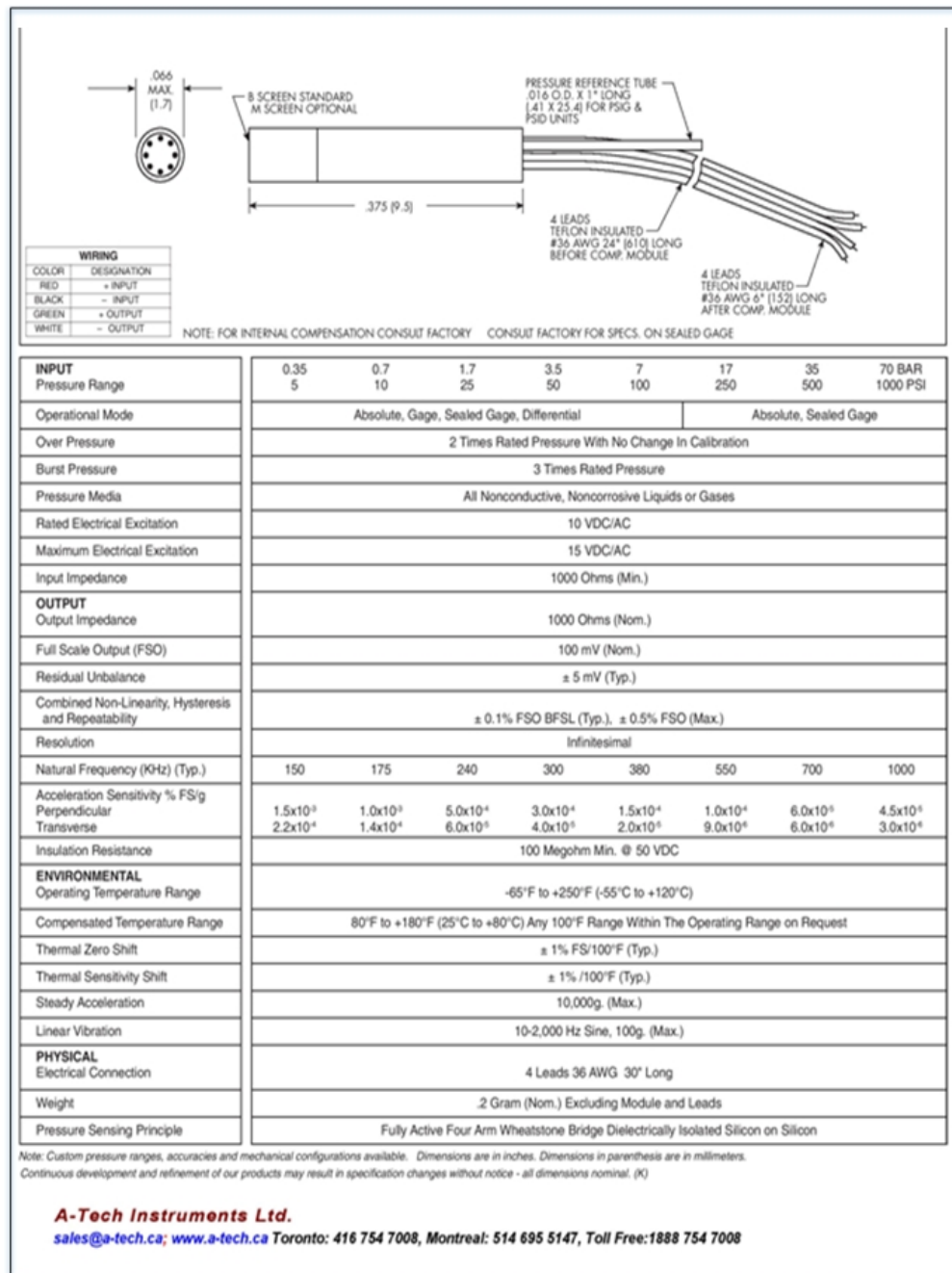


Figure A-I-1 Kulite XCQ-062 transducer specifications
 Taken from Kulie (2014)

ANNEX II

ACCELEROMETERS SPECIFICATIONS

ADXL326					
SPECIFICATIONS					
T _A = 25°C, V _S = 3 V, C _X = C _Y = C _Z = 0.1 µF, acceleration = 0 g, unless otherwise noted. All minimum and maximum specifications are guaranteed. Typical specifications are not guaranteed.					
Table 1.					
Parameter	Conditions	Min	Typ	Max	Unit
SENSOR INPUT	Each axis				
Measurement Range		±16	±19		g
Nonlinearity	Percent of full scale		±0.3		%
Package Alignment Error			±1		Degrees
Interaxis Alignment Error			±0.1		Degrees
Cross Axis Sensitivity ¹			±1		%
SENSITIVITY (RATIOMETRIC) ²	Each axis				
Sensitivity at X _{OUT} , Y _{OUT} , Z _{OUT}	V _S = 3 V	51	57	63	mV/g
Sensitivity Change Due to Temperature ³	V _S = 3 V		±0.01		%/°C
ZERO g BIAS LEVEL (RATIOMETRIC)					
0 g Voltage at X _{OUT} , Y _{OUT}	V _S = 3 V	1.35	1.5	1.65	V
0 g Voltage at Z _{OUT}	V _S = 3 V	1.2	1.5	1.8	V
0 g Offset vs. Temperature			±1		mg/°C
NOISE PERFORMANCE					
Noise Density X _{OUT} , Y _{OUT} , Z _{OUT}			300		µg/√Hz rms
FREQUENCY RESPONSE ⁴					
Bandwidth X _{OUT} , Y _{OUT} ⁵	No external filter		1600		Hz
Bandwidth Z _{OUT} ⁵	No external filter		550		Hz
R _{FLT} Tolerance			32 ± 15%		kΩ
Sensor Resonant Frequency			5.5		kHz
SELF TEST ⁶					
Logic Input Low			+0.6		V
Logic Input High			+2.4		V
ST Actuation Current			+60		µA
Output Change at X _{OUT}	Self test 0 to 1	−29	−62	−114	mV
Output Change at Y _{OUT}	Self test 0 to 1	+29	+62	+114	mV
Output Change at Z _{OUT}	Self test 0 to 1	+29	+105	+190	mV
OUTPUT AMPLIFIER					
Output Swing Low	No load		0.1		V
Output Swing High	No load		2.8		V
POWER SUPPLY					
Operating Voltage Range		1.8		3.6	V
Supply Current	V _S = 3 V		350		µA
Turn-On Time ⁷	No external filter		1		ms
TEMPERATURE					
Operating Temperature Range		−40		+85	°C

¹ Defined as coupling between any two axes.

² Sensitivity is essentially ratiometric to V_S.

³ Defined as the output change from ambient-to-maximum temperature or ambient-to-minimum temperature.

⁴ Actual frequency response controlled by user-supplied external filter capacitors (C_X, C_Y, C_Z).

⁵ Bandwidth with external capacitors = 1/(2 × π × 32 kΩ × C). For C_X, C_Y = 0.003 µF, bandwidth = 1.6 kHz. For C_Z = 0.01 µF, bandwidth = 500 Hz. For C_X, C_Y, C_Z = 10 µF, bandwidth = 0.5 Hz.

⁶ Self test response changes cubically with V_S.

⁷ Turn-on time is dependent on C_X, C_Y, C_Z and is approximately 160 × C_X or C_Y or C_Z + 1 ms, where C_X, C_Y, C_Z are in µF.

Figure A-II-1 ADXL 326 sensor specifications
Taken from analog devices (2009)

ANNEX III

SPECIFICATION OF THE ACQUISITION MODULE FOR ACCELEROMETERS


	
DEVICE SPECIFICATIONS	
NI USB-6212	
M Series Data Acquisition: 16 AI, 2 AO, 32 DIO Bus-Powered USB	
Analog Output	
Number of channels	2
DAC resolution	16 bits
DNL	±1 LSB
Monotonicity	16 bit guaranteed
Maximum update rate	
1 channel	250 kS/s
2 channels	250 kS/s per channel
Timing accuracy	50 ppm of sample rate
Timing resolution	50 ns
Output range	±10 V
Output coupling	DC
Output impedance	0.2 Ω
Output current drive	±2 mA
Overdrive protection	±30 V
Overdrive current	2.4 mA
Power-on state	±20 mV
Power-on glitch	±1 V for 200 ms
Output FIFO size	8,191 samples shared among channels used
Data transfers	USB Signal Stream, programmed I/O
AO waveform modes	Non-periodic waveform, periodic waveform regeneration mode from onboard FIFO, periodic waveform regeneration from host buffer including dynamic update
Settling time, full-scale step, 15 ppm (1 LSB)	32 μs
Slew rate	5 V/μs
Glitch energy	
Magnitude	100 mV

Figure A-III-1 NI USB-6212 specifications
Adapted from National Instruments (2016)

BIBLIOGRAPHY

- Albarbar, A, A Badri, Jyoti K Sinha et A Starr. 2009. « Performance evaluation of MEMS accelerometers ». *Measurement*, vol. 42, n° 5, p. 790-795.
- Analog devices. 2009. « ADXL326 Small, Low Power, 3-Axis ± 16 g Accelerometer ». < <http://www.analog.com/en/products/mems/accelerometers/adxl326.html#product-overview>>. Accessed June 15, 2016.
- Barbarino, Silvestro, Onur Bilgen, Rafic M Ajaj, Michael I Friswell et Daniel J Inman. 2011. « A review of morphing aircraft ». *Journal of Intelligent Material Systems and Structures*, vol. 22, n° 9, p. 823-877.
- Bellanger, É., Perez, J., Ducros, X., & Renvoizé, V. (2013). *Physique MPSI-PCSI-PTSI: Programme 2013*. Pearson Education France.
- Bracht, K, et W Merzkirch. 1977. « Schlieren visualization of the laminar-to-turbulent transition in a shock-tube boundary-layer ». In *International Symposium on Flow Visualization*. Vol. 1, p. 241-246.
- Broch, Jens Trampe. 1980. *Mechanical vibration and shock measurements*. Brüel & Kjær.
- Burrows, Michael L. 1975. *Strain-gage vibration measurements on a submarine-towed antenna cable*. DTIC Document.
- Chendjou, Yvan Wilfried Tondji, et Ruxandra Botez. 2014. *Numerical and Experimental Measures of the Unmanned Aerial System UAS-S4 of Hydra Technologies*. SAE Technical Paper.
- Chopra, Inderjit. 2002. « Review of state of art of smart structures and integrated systems ». *AIAA journal*, vol. 40, n° 11, p. 2145-2187.
- Courchesne, Samuel, Andrei Vladimir Popov et Ruxandra Mihaela Botez. 2010. « New aeroelastic studies for a morphing wing ». In *Proceedings of the 48th AIAA Aerospace Sciences Meeting Including the New Horizons Forum and Aerospace Exposition, American Institute of Aeronautics and Astronautics (AIAA), Washington, DC*.
- Crawford, Brian K, Glen T Duncan Jr, David E West et William S Saric. 2013. « Laminar-turbulent boundary layer transition imaging using IR thermography ». *Optics and Photonics Journal*, vol. 3, n° 03, p. 233.
- Crouch, JD, et LL Ng. 2000. « Variable N-factor method for transition prediction in three-dimensional boundary layers ». *AIAA journal*, vol. 38, n° 2, p. 211-216.

- Crowder, James P. 1980. « Add fluorescent minitufts to the aerodynamicist's bag of tricks ». *Astronautics Aeronautics*, vol. 18, p. 54-56.
- Drake, Aaron. 2010. « Oil Film Interferometry in the Development of Long-Endurance Aircraft ». In *48th AIAA Aerospace Sciences Meeting Including the New Horizons Forum and Aerospace Exposi. Orlando, Florida*. p. 4-7.
- Flore, Lica, et Albert Arnau Cubillo. 2015. « DYNAMIC MECHANICAL ANALYSIS OF AN AIRCRAFT WING WITH EMPHASIS ON VIBRATION MODES CHANGE WITH LOADING ». *Scientific Research & Education in the Air Force-AFASES*, vol. 2.
- Galbraith, RA, et FN Coton. 1990. « Two-dimensional, incompressible aerofoil design and analysis ». *Computational methods in viscous aerodynamics(A 92-21976 07-02)*. Amsterdam, Netherlands and New York/Southampton, England, Elsevier/Computational Mechanics Publications, 1990, p. 331-367.
- GUEZGUEZ, Mohamed Sadok. 2015. « Morphing Wing System Integration with Wind Tunnel Testing ». ÉCOLE DE TECHNOLOGIE SUPÉRIEURE.
- Hallcrest, LCR. « TLC Products for Use in Research and Testing Applications ». *LCR Hallcrest Research & Testing Products, Rev*, vol. 1, p. 1-18.
- Herbert, Thorwald. 1988. « Secondary instability of boundary layers ». *Annual Review of Fluid Mechanics*, vol. 20, n° 1, p. 487-526.
- Holmes, Bruce J, Peter D Gall, Cynthia C Croom, Gregory S Manuel et Warren C Kelliher. 1986. « A new method for laminar boundary layer transition visualization in flight: Color changes in liquid crystal coatings ».
- Hussain, Malik Zawwar, et Muhammad Sarfraz. 2009. « Monotone piecewise rational cubic interpolation ». *International Journal of Computer Mathematics*, vol. 86, n° 3, p. 423-430.
- Joseph, Liselle A, Aurelien Borgoltz et William Devenport. 2014. « Transition Detection for Low Speed Wind Tunnel Testing using Infrared Thermography ». In *30th AIAA Aerodynamic Measurement Technology and Ground Testing Conference*. p. 2939.
- IATA, I. A. T. A. 2015. « The IATA Technology Roadmap 2015. 3rd Edition ». En ligne. <<http://www.iata.org/whatwedo/environment/Documents/technology-roadmap-2015.pdf>>. Accessed on August 03, 2016.
- Kachanov, Yury S. 1994. « Physical mechanisms of laminar-boundary-layer transition ». *Annual review of fluid mechanics*, vol. 26, n° 1, p. 411-482.

- Kammegne, Michel Joel Tchatchueng, Ruxandra Mihaela Botez et Teodor Lucian Grigorie. 2016 « Actuation mechanism control in a morphing application with a full-scaled portion of an aircraft wing ».
- Kleiser, Leonhard, et Thomas A Zang. 1991. « Numerical simulation of transition in wall-bounded shear flows ». *Annual Review of Fluid Mechanics*, vol. 23, n° 1, p. 495-537.
- Koreanschi, A, O Sugar et RM Botez. 2015. « Drag Optimization of a Wing Equipped with a Morphing Upper Surface ». *Royal Aeronautical Journal*.
- Koreanschi, Andreea, Mehdi Ben Henia, Olivier Guillemette, Francois Michaud, Yvan Tondji, Oliviú Sugar Gabor, Ruxandra Mihaela Botez et Manuel Flores Salinas. 2016. « Flutter Analysis of a Morphing Wing Technology Demonstrator: Numerical Simulation and Wind Tunnel Testing a ». *INCAS Bulletin*, vol. 8, n° 1, p. 99.
- Koreanschi, Andreea, O Sugar-Gabor et Botez. 2014. « New numerical study of boundary layer behaviour on a morphing wing-with-aileron system ». In *American Institute of Aeronautics and Astronautics AIAA 32nd Applied Aerodynamics Conference, Atlanta, GA, USA*. p. 16-20.
- Lalanne, Christian. 2013. *Mechanical Vibration and Shock Analysis, Specification Development*, 5. John Wiley & Sons.
- Loving, Donald L, et Samuel Katzoff. 1959. « The Fluorescent-Oil Film Method and Other Techniques for Boundary-Layer Flow Visualization ».
- Mack, Leslie M. 1977. « Transition prediction and linear stability theory ». In *In AGARD Laminar-Turbulent Transition 22 p (SEE N78-14316 05-34)*. Vol. 1.
- Mack, Leslie M. 1984. *Boundary-layer linear stability theory*. DTIC Document.
- Mamou, M, Y Mébarki, M Khalid, M Genest, D Coutu, AV Popov, C Sainmont, T Georges, L Grigorie et RM Botez. 2010. « Aerodynamic performance optimization of a wind tunnel morphing wing model subject to various cruise flow conditions ». *Proc of ICAS'27*, p. 1-18.
- Mathematics. 2014, « Root Mean Square of Sum of Sinusoids with Different Frequencies ». < <http://math.stackexchange.com/q/974755> >. Accessed September 20, 2016
- Mathworks. 2006. « Fast Fourier Transform ». < <http://www.mathworks.com/help/matlab/ref/fft.html> >. Accessed June 13, 2016.
- Mathworks. 2006. « Standard deviation ». < <http://www.mathworks.com/help/matlab/ref/std.html> >. Accessed June 13, 2016.

- Mathworks. 2006. « Welch's power spectral density estimate ». < <http://www.mathworks.com/help/signal/ref/pwelch.html>>. Accessed June 13, 2016.
- McFadden, PD, et JD Smith. 1984. « Vibration monitoring of rolling element bearings by the high-frequency resonance technique—a review ». *Tribology international*, vol. 17, n° 1, p. 3-10.
- Michaud, François, Simon Joncas et Ruxandra Botez. 2013. « Design manufacturing and testing of a small-scale composite morphing wing ». In *19th Conference on composite materials*.
- Murugan, Senthil, et MI Friswell. 2013. « Morphing wing flexible skins with curvilinear fiber composites ». *Composite Structures*, vol. 99, p. 69-75.
- National Research Council Canada. 2013. « 2 m x 3 m wind tunnel ». < http://www.nrcnrc.gc.ca/eng/solutions/facilities/wind_tunnel/2x3_metre.html>. Consulté le 16 juin 2016.
- Omega Engineering. 2000. « STRAIN GAGE TECHNICAL DATA » 5 p. Retrieved from https://www.omega.ca/techref/pdf/STRAIN_GAGE_TECHNICAL_DATA.pdf. Accessed september 04, 2016.
- Parameswaran, S, et S Jayantha. 1999. « Spectral analysis of pressure fluctuations on bluff bodies placed in turbulent flows ». *COMPUTATIONAL FLUID DYNAMICS JOURNAL*, vol. 8, n° 3, p. 436-442.
- Pisoni, Attilio C, Claudio Santolini, Dagmar E Hauf et Steven Dubowsky. 1995. « Displacements in a vibrating body by strain gage measurements ». In *PROCEEDINGS-SPIE THE INTERNATIONAL SOCIETY FOR OPTICAL ENGINEERING*. p. 119-119. SPIE INTERNATIONAL SOCIETY FOR OPTICAL.
- Popov, Andrei Vladimir, Ruxandra Mihaela Botez et Michel Labib. 2008. « Transition point detection from the surface pressure distribution for controller design ». *Journal of Aircraft*, vol. 45, n° 1, p. 23-28.
- Popov, Andrei Vladimir, Teodor Lucian Grigorie, Ruxandra Mihaela Botez, Youssef Mébarki et Mahmood Mamou. 2010. « Modeling and testing of a morphing wing in open-loop architecture ». *Journal of Aircraft*, vol. 47, n° 3, p. 917-923.
- Popov, AV, RM Botez, M Mamou, Y Mébarki, B Jahrhaus, M Khalid et TL Grigorie. 2009. « Drag reduction by improving laminar flows past morphing configurations ». In *AVT-168 NATO Symposium on the Morphing Vehicles*.

- Sainmont, C, I Paraschivoiu et D Coutu. 2009. « Multidisciplinary approach for the optimization of a laminar airfoil equipped with a morphing upper surface ». In *NATO AVT-168 Symposium on Morphing Vehicles*.
- Saric, William S, Helen L Reed et Edward J Kerschen. 2002. « Boundary-layer receptivity to freestream disturbances ». *Annual review of fluid mechanics*, vol. 34, n° 1, p. 291-319.
- Schlichting, Hermann. 1968. « Boundary-layer theory ».
- Semiconductor, Kulite. 2014. « XCQ-062 ». En ligne. <<http://www.advizia.com/v41/ModelDetail.asp?User=KuliteTransducers&PkgOrder=186&Rnd=429>>. Consulté le 03 Juillet 2016.
- Smith, AMO, et N Gamberoni. 1956. « Transition, Pressure Gradient, and Stability Theory. Report no. ES. 26388, Douglas Aircraft Co ». *Inc., El Segundo, CA*.
- Smith, Stephen B., et David W. Nelson. 1990. « Determination of the aerodynamic characteristics of the mission adaptive wing ». *Journal of Aircraft*, vol. 27, n° 11, p. 950-958.
- Stanewsky, E. 2001. « Adaptive wing and flow control technology ». *Progress in Aerospace Sciences*, vol. 37, n° 7, p. 583-667.
- Sykora, Daniel M, et Michael L Holmes. 2011. « Dynamic measurements using a Fizeau interferometer ». In *SPIE Optical Metrology*. p. 80821R-80821R-10. International Society for Optics and Photonics.
- Tanner, LH, et LG Blows. 1976. « A study of the motion of oil films on surfaces in air flow, with application to the measurement of skin friction ». *Journal of Physics E: Scientific Instruments*, vol. 9, n° 3, p. 194.
- Thill, C, J Etches, I Bond, K Potter et P Weaver. 2008. « Morphing skins ». *The Aeronautical Journal*, vol. 112, n° 1129, p. 117-139.
- Thomas C. Ferree. 2010. Inferring signal amplitudes from discrete (FFT) power values. «Technical note from Electrical Geodesics, Inc.», 07 p.
- Van Ingen, JL. 1956. *A suggested semi-empirical method for the calculation of the boundary layer transition region*. Delft University of Technology.
- Weisshaar, Terrence A. 2006. *Morphing aircraft technology-new shapes for aircraft design*. DTIC Document.
- White, Frank. 2006. *Viscous fluid flow*. McGraw-Hill series in mechanical engineering, 439 p.

Wilson, Earl J. 1976. « Strain-gage Instrumentation ». *Harris' Shock and Vibration Handbook, S*, p. 17.1-17.15.

Young, Donald F, Bruce R Munson, Theodore H Okiishi et Wade W Huebsch. 2010. *A brief introduction to fluid mechanics*. John Wiley & Sons

